



FILE COPY

NBS TECHNICAL NOTE 1072

DO NOT TAKE

U.S. DEPARTMENT OF COMMERCE / National Bureau of Standards

# Theory of Near-Field Phased Arrays for Electromagnetic Susceptibility Testing

DC  
100  
U5753  
NO. 1072  
1984

## NATIONAL BUREAU OF STANDARDS

The National Bureau of Standards<sup>1</sup> was established by an act of Congress on March 3, 1901. The Bureau's overall goal is to strengthen and advance the Nation's science and technology and facilitate their effective application for public benefit. To this end, the Bureau conducts research and provides: (1) a basis for the Nation's physical measurement system, (2) scientific and technological services for industry and government, (3) a technical basis for equity in trade, and (4) technical services to promote public safety. The Bureau's technical work is performed by the National Measurement Laboratory, the National Engineering Laboratory, and the Institute for Computer Sciences and Technology.

**THE NATIONAL MEASUREMENT LABORATORY** provides the national system of physical and chemical and materials measurement; coordinates the system with measurement systems of other nations and furnishes essential services leading to accurate and uniform physical and chemical measurement throughout the Nation's scientific community, industry, and commerce; conducts materials research leading to improved methods of measurement, standards, and data on the properties of materials needed by industry, commerce, educational institutions, and Government; provides advisory and research services to other Government agencies; develops, produces, and distributes Standard Reference Materials; and provides calibration services. The Laboratory consists of the following centers:

Absolute Physical Quantities<sup>2</sup> — Radiation Research — Chemical Physics —  
Analytical Chemistry — Materials Science

**THE NATIONAL ENGINEERING LABORATORY** provides technology and technical services to the public and private sectors to address national needs and to solve national problems; conducts research in engineering and applied science in support of these efforts; builds and maintains competence in the necessary disciplines required to carry out this research and technical service; develops engineering data and measurement capabilities; provides engineering measurement traceability services; develops test methods and proposes engineering standards and code changes; develops and proposes new engineering practices; and develops and improves mechanisms to transfer results of its research to the ultimate user. The Laboratory consists of the following centers:

Applied Mathematics — Electronics and Electrical Engineering<sup>2</sup> — Manufacturing Engineering — Building Technology — Fire Research — Chemical Engineering<sup>2</sup>

**THE INSTITUTE FOR COMPUTER SCIENCES AND TECHNOLOGY** conducts research and provides scientific and technical services to aid Federal agencies in the selection, acquisition, application, and use of computer technology to improve effectiveness and economy in Government operations in accordance with Public Law 89-306 (40 U.S.C. 759), relevant Executive Orders, and other directives; carries out this mission by managing the Federal Information Processing Standards Program, developing Federal ADP standards guidelines, and managing Federal participation in ADP voluntary standardization activities; provides scientific and technological advisory services and assistance to Federal agencies; and provides the technical foundation for computer-related policies of the Federal Government. The Institute consists of the following centers:

Programming Science and Technology — Computer Systems Engineering.

<sup>1</sup>Headquarters and Laboratories at Gaithersburg, MD, unless otherwise noted; mailing address Washington, DC 20234.

<sup>2</sup>Some divisions within the center are located at Boulder, CO 80303.

# Theory of Near-Field Phased Arrays for Electromagnetic Susceptibility Testing

David A. Hill

Electromagnetic Fields Division  
National Engineering Laboratory  
National Bureau of Standards  
U.S. Department of Commerce  
Boulder, Colorado 80303



---

U.S. DEPARTMENT OF COMMERCE, Malcolm Baldrige, Secretary

NATIONAL BUREAU OF STANDARDS, Ernest Ambler, Director

Issued February 1984

National Bureau of Standards Technical Note 1072  
Natl. Bur. Stand. (U.S.), Tech Note 1072, 109 pages (Feb. 1984)  
CODEN: NBTNAE

U.S. GOVERNMENT PRINTING OFFICE  
WASHINGTON: 1984

## CONTENTS

	Page
1. Introduction.....	1
2. Review of previous work.....	3
3. Basic concepts.....	4
3.1 Equivalence principle.....	4
3.2 Relationship to scattering problem.....	6
3.3 Sampling and scanning considerations.....	10
4. Near fields of smooth current distributions.....	12
4.1 Two-dimensional geometry.....	13
4.2 Three-dimensional geometry.....	18
5. Near fields of arrays.....	22
5.1 Electric dipole array.....	23
5.2 Huygens' source array.....	26
6. Near-field array synthesis.....	28
6.1 A new uniqueness theorem.....	29
6.2 Least squares analysis.....	32
6.3 Line source example.....	36
7. Conclusions and recommendations.....	42
8. Acknowledgments.....	44
9. References.....	44
Appendix A Asymptotic evaluation of two-dimensional fields.....	48
Appendix B Asymptotic evaluation of three-dimensional fields.....	53
Appendix C Fields of a Hertzian dipole.....	61
Appendix D Fields of a Huygens' source.....	63
Appendix E A uniqueness example.....	65
Appendix F Line source fields.....	68



# **Theory of Near-Field Phased Arrays for Electromagnetic Susceptibility Testing**

David A. Hill

Electromagnetic Fields Division  
National Bureau of Standards  
Boulder, Colorado 80303

The feasibility of using a near-field array for electromagnetic susceptibility testing is studied. The basic objective is to control the element weightings such that a plane wave is generated within the test volume. The basic theory is developed for arbitrary array geometries, and numerical results are obtained for finite planar arrays. A general near-field array synthesis technique is developed, and the technique minimizes the mean square error in the test volume while constraining the array excitations. The constraint prevents large excitations and is useful in minimizing the fields outside the test volume. The basic idea looks promising, but some practical considerations, such as bandwidth and angular scanning limitations, require further theoretical and experimental investigation.

Key words: array synthesis; dipole; electromagnetic susceptibility; Huygens' source; line source; near field; phased array.

## **1. Introduction**

The ideal incident field for electromagnetic susceptibility testing is one which is a uniform plane wave throughout the test volume. The field outside the test volume is arbitrary in principle because it does not affect the response of the equipment under test (EUT). However, it is desirable to keep the field outside the test volume small in order to avoid wasted power and reflections from surrounding objects. Thus, a far-field antenna range is not generally acceptable for susceptibility testing because only a small portion of the total power is incident on the test volume. An additional disadvantage with far-field ranges is that the far-field distance is often very large. It is desirable that the test facility dimensions not be too much larger than the dimensions of the test volume so that the facility could be located indoors.

Present methods of producing a plane wave can be divided into "low frequency" and "high frequency" methods. The low frequency methods utilize a section of a transmission line which supports a transverse electromagnetic

(TEM) wave. Both parallel plate lines and TEM cells have been used to produce fields which are planar over a portion of their cross section. The transmission line dimensions are normally somewhat less than a wavelength so that higher order modes cannot propagate. Consequently, transmission line methods are most effective for testing EUTs which are electrically small. High frequency methods generally focus a spherical wave into a plane wave with a microwave lens [1] or a paraboloidal reflector. Both methods are designed on the basis of ray tracing and are thus limited to high frequencies. The paraboloidal reflector, which has been termed "compact range" [2], has been used quite successfully for antenna pattern measurements and with less success for radar cross-section measurements. There exists a frequency gap (about 50 MHz to 1 GHz) between the low frequency and high frequency methods where another method of producing a plane wave is needed.

The present methods generate a fixed plane wave and have no capability of scanning the angle of arrival. Thus, the EUT must be rotated in order to obtain angular information. The possibility of a compact range with a spherical reflector and a movable feed to allow angular scanning has been discussed [3], but it has not been determined whether a spherical reflector will produce a plane wave of acceptable quality.

The near-field phased array method, which we analyze in this report, has the potential of electronically scanning in both elevation and azimuth. If the EUT is located on a turntable [3], then an electronic scan in elevation is sufficient. Another potential advantage of a near-field array over a compact range is that arrays should be able to work down to lower frequencies since they are not limited to the geometrical optics range. The frequency range of interest runs from about 30 MHz up to microwaves.

The organization of this report is as follows. Section 2 contains a review of previous work on near-field arrays. Section 3 introduces some of the basic concepts in near-field phased arrays and points out the relationships to near-field scanning and electromagnetic scattering problems. Section 4 presents analytical and numerical results for the near fields of continuous current distributions. The abrupt truncation of the current at the edge of the source region is shown to produce an undesirable edge diffraction field

within the test volume. Section 5 presents analytical and numerical results for the near fields of discrete arrays, and the effect of element spacing is studied. Section 6 presents a fairly general array synthesis procedure for minimizing the difference between the actual field and the desired plane wave field within the test volume. A constraint condition also provides a means of keeping the field strength small outside the test volume. Section 7 summarizes the results of this study and makes recommendations for further work.

## 2. Review of previous work

The idea of generating a plane wave in the near field of a phased array was discussed as early as 1968 by Martsafey [4] who analyzed an infinite planar array. He showed that if the element spacing is less than a half wavelength, the field of the array consists of a single propagating plane wave and an infinite sum of decaying evanescent waves. Other geometries are more complicated, but spherical [5,6] and cylindrical [7] arrays have also been analyzed.

Ludwig and Larsen [6] pointed out that synthesizing a plane wave in a test volume is the reciprocal case to predicting the far-field pattern of an antenna which is transmitting from the test volume. Thus, the array element weightings in the plane wave synthesis case are the same as the probe weightings in near-field scanning. They confirmed this relationship for a spherical geometry with electric dipole elements by computing the field inside a sphere where the element weightings were given by the spherical near-field scanning theory. The plane wave quality was good when a full sphere was used, but deteriorated when the array covered only a portion of the sphere. Actually, when the array is truncated, the spherical near-field scanning theory no longer gives the best weighting values. Ludwig and Larsen [6] have suggested that the determination of the optimum weights for truncated spheres is an interesting area for future work.

Bennett and Schoessow [5] determined the weighting function for a truncated spherical array by using an approximate diffraction integral. They attempted to reduce the error field in the test zone by multiple iterations and were partially successful. Many detailed calculations are contained in

the Ph.D. thesis by Schoessow [8]. A Fourier analysis of the field in the test zone showed that much of the error field originated from the edges of the array.

The only experimental results have been obtained by Lynggaard [9] who built and tested a five-element array of horns. The array was essentially planar, but the theory for a large sphere [6] was used to determine the element weightings. The test volume was a small sphere at a fairly large distance from the array. Directional scanning of the plane wave was not attempted.

### 3. Basic concepts

#### 3.1. Equivalence principle

The electric and magnetic fields,  $\underline{E}_p$  and  $\underline{H}_p$ , of a time harmonic,  $\exp(j\omega t)$ , plane wave can be written in the following form:

$$\begin{aligned}\underline{E}_p &= \underline{E}_0 \exp(-j \underline{k} \cdot \underline{r}) , \\ \underline{H}_p &= \underline{H}_0 \exp(-j \underline{k} \cdot \underline{r}) ,\end{aligned}\tag{1}$$

where

$$\underline{E}_0 \cdot \underline{k} = 0, \quad \underline{H}_0 = \hat{k} \times \underline{E}_0 / \eta ,$$

$$\hat{k} = \underline{k} / |\underline{k}|, \quad |\underline{k}| = 2\pi / \lambda ,$$

$\eta$  is the free space impedance,  $\lambda$  is the free space wavelength,  $\underline{r}$  is the position vector, and  $\underline{E}_0$  is a constant. All field and source quantities are assumed to vary as  $\exp(j\omega t)$ , and the time dependence will be suppressed throughout this report. For a propagating plane wave,  $\underline{k}$  is real in (1) and the electric and magnetic fields have constant magnitudes. The plane wave fields in (1) are solutions to the source-free Maxwell's equations in a homogenous, infinite region.

The equivalence principle can be used to show that the plane wave fields in (1) can also be generated by sources in a finite region. Consider a volume

V enclosed by a surface S as shown in figure 1. Inside S, we specify planar fields,  $\underline{E}_p$  and  $\underline{H}_p$ , as given by (1). Outside S, the exterior fields,  $\underline{E}_e$  and  $\underline{H}_e$ , are arbitrary outgoing fields which satisfy Maxwell's equations. By outgoing fields, we mean that they satisfy the radiation condition at infinity. From the equivalence principle [10], these fields can be generated by the following electric and magnetic surface currents,  $\underline{J}$  and  $\underline{M}$ , on S:

$$\underline{J} = \hat{n} \times (\underline{H}_p - \underline{H}_e) \text{ and } \underline{M} = (\underline{E}_p - \underline{E}_e) \times \hat{n}, \quad (2)$$

where  $\hat{n}$  is the inward unit normal to S.  $\underline{J}$  and  $\underline{M}$  have units of amperes/m and volts/m, respectively. Because  $\underline{E}_e$  and  $\underline{H}_e$  in (2) are arbitrary, the source currents  $\underline{J}$  and  $\underline{M}$  are nonunique, and there are many current distributions which will generate a perfect plane wave inside S. Nonuniqueness is typical of inverse problems where the fields in a region are specified and the sources are unknown. The practical problem involves finding a solution of (2) where the currents  $\underline{J}$  and  $\underline{M}$  can be approximated well by a phased array of realistic antenna elements. As an aside, the plane wave fields,  $\underline{E}_p$  and  $\underline{H}_p$ , in (2) could actually be any desired fields which satisfy the source-free Maxwell's equations. So far only plane wave fields are of interest for electromagnetic susceptibility testing, and we consider only plane wave synthesis throughout this report.

The most desirable case of (2) is obtained when the exterior fields,  $\underline{E}_e$  and  $\underline{H}_e$ , are zero. Then the surface currents,  $\underline{J}_0$  and  $\underline{M}_0$ , are simply:

$$\underline{J}_0 = \hat{n} \times \underline{H}_p \quad \text{and} \quad \underline{M}_0 = \underline{E}_p \times \hat{n} \quad (3)$$

Since the exterior fields of the current distribution in (3) are zero, it makes no difference what the surrounding medium is as shown in figure 2. Consequently, surrounding objects would not contribute undesirable reflections because they would not be illuminated by the sources  $\underline{J}_0$  and  $\underline{M}_0$ .

Although the source distributions in (2) and (3) are highly idealized, they show that there is no basic limitation to generating a perfect plane wave in the near field of sources. The practical limitations arise from the use of

an array of realistic antennas in attempting to approximate the smooth electric and magnetic current distributions of (2) and (3).

### 3.2. Relationship to scattering problem

One disadvantage of the sources given by (2) is that both electric and magnetic surface currents are required. It would be useful to have solutions requiring only electric currents or magnetic currents rather than a combination of both. An electric current distribution might be approximated by an array of dipole antennas, and a magnetic current distribution might be approximated by an array of loops (magnetic dipoles). The desired solutions can be found by examining the relevant scattering problems.

Consider electric and magnetic fields,  $\underline{E}_i$  and  $\underline{H}_i$ , incident on a closed, perfect electric conductor as shown in figure 3a. Only an electric surface current  $\underline{J}_s$  will be set up on the surface  $S$ , and that current distribution will radiate scattered electric and magnetic fields,  $\underline{E}_s$  and  $\underline{H}_s$ . The total field everywhere is the sum of the incident and scattered fields. Inside  $S$ , the total field must be zero in accordance with Waterman's extended boundary condition [11]:

$$\underline{E}_i + \underline{E}_s = 0 \quad \text{and} \quad \underline{H}_i + \underline{H}_s = 0 . \quad (4)$$

If we choose the incident field to be the negative of the desired plane wave ( $\underline{E}_i = - \underline{E}_p$ ,  $\underline{H}_i = - \underline{H}_p$ ), then from (4) the scattered fields inside  $S$  are exactly the desired plane wave:

$$\underline{E}_s = \underline{E}_p \quad \text{and} \quad \underline{H}_s = \underline{H}_p . \quad (5)$$

If we now remove the incident field and let the scattered current  $\underline{J}_s$  radiate in free space, the result will be the desired plane wave inside  $S$  and scattered fields,  $\underline{E}_s$  and  $\underline{H}_s$ , outside  $S$  as shown in figure 3b. Thus, the problem of finding an electric surface current distribution which generates a plane wave inside  $S$  is equivalent to solving the problem of plane wave scattering by the same shape. Analytical solutions are available for plane wave scattering

by simple shapes [12] such as spheres and cylinders. Numerical methods are required for general shapes, and integral equation solutions [13] are typically utilized.

To obtain a solution to (2) with only magnetic surface currents, it is possible to pursue the same method for a perfect magnetic conductor. An alternative is to apply duality [10] directly to the electric current configuration in figure 3b by replacing the fields and sources as follows:

$$\begin{aligned} \underline{E}_p &\rightarrow \underline{H}_p, & \underline{E}_s &\rightarrow \underline{H}_s, \\ \underline{H}_p &\rightarrow -\underline{E}_p, & \underline{H}_s &\rightarrow -\underline{E}_s, \\ \text{and} & & \underline{J}_s &\rightarrow \underline{M}_s. \end{aligned} \quad (6)$$

Thus, magnetic currents  $\underline{M}_s$  on  $S$  will produce a plane wave inside  $S$ , but the polarization will be orthogonal to that of the plane wave produced by  $\underline{J}_s$  in figure 3b. If the scattering solution pictured in 3a is known for both polarizations of the incident field, then the dual magnetic current solution can be obtained for both polarizations from (5).

A more general solution, where the electric and magnetic currents have a fixed ratio over the entire surface  $S$ , can be obtained when the scatterer is characterized by a surface impedance boundary condition [14] as shown in figure 4a. If  $\underline{E}_t$  and  $\underline{H}_t$  are the total (incident plus scattered) electric and magnetic fields just outside  $S$ , they are required to satisfy

$$\hat{n} \times (\hat{n} \times \underline{E}_t) = Z \hat{n} \times \underline{H}_t, \quad (7)$$

where  $Z$  is the surface impedance. Equivalent electric and magnetic currents  $\underline{J}_s$  and  $\underline{M}_s$  can be defined

$$\underline{J}_s = -\hat{n} \times \underline{H}_t \quad \text{and} \quad \underline{M}_s = \hat{n} \times \underline{E}_t. \quad (8)$$

From (7), we can relate  $\underline{J}_S$  and  $\underline{M}_S$ :

$$\underline{J}_S = -\frac{1}{Z} \hat{n} \times \underline{M}_S \quad \text{or} \quad \underline{M}_S = Z \hat{n} \times \underline{J}_S . \quad (9)$$

From (9), we can see that  $\underline{J}_S$  and  $\underline{M}_S$  are orthogonal and the ratio of their magnitudes is determined by  $Z$ . The case,  $Z = 0$ , represents a perfect electric conductor as in figure 3a, and  $\underline{M}_S = 0$ . The case,  $Z = \infty$ , represents a perfect magnetic conductor, and  $\underline{J}_S = 0$ . As shown in figure 4b, if we let  $\underline{J}_S$  and  $\underline{M}_S$  radiate in free space, they generate a plane wave field inside  $S$  and scattered fields outside  $S$ . If we let  $Z$  equal the free space impedance  $\eta$ , then the electric and magnetic currents in (9) radiate as a distribution of Huygen's sources [15]. A Huygen's source is essentially a small portion of a plane wave and can be considered an approximate model for a small aperture antenna, such as a horn or an open-ended waveguide. It has also been used to model the probe antenna in the theory of near-field scanning [16].

In general, the scattering problem for impedance surfaces [17] is somewhat more difficult than for perfectly conducting surfaces. However, the planar case is useful for illustrating the significance of the value of  $Z$ . Consider a plane wave incident on an impedance plane ( $z = 0$ ) as in figure 5a. The incident fields,  $E_{yi}$ , and  $H_{xi}$ , and reflected fields,  $E_{ys}$  and  $H_{xs}$ , are given by:

$$\begin{aligned} E_{yi} &= -E_0 e^{ikz} , & H_{xi} &= -\frac{E_0}{\eta} e^{ikz} , \\ E_{ys} &= -R E_0 e^{-ikz} , & H_{xs} &= \frac{R E_0}{\eta} e^{-ikz} , \end{aligned} \quad (10)$$

$$R = \frac{\Delta - 1}{\Delta + 1} , \quad \text{and} \quad \Delta = Z/\eta .$$

The equivalent currents are determined from (8) and (10):

$$\underline{J}_{ys} = -\frac{E_0}{\eta} \cdot \frac{2}{1 + \Delta} \quad \text{and} \quad \underline{M}_{xs} = -Z \underline{J}_{ys} . \quad (11)$$

If we let the currents in (11) radiate in free space, the desired plane wave fields,  $E_{yp}$  and  $H_{xp}$ , are radiated in the negative  $z$  half space as shown in figure 5b:

$$E_{yp} = E_0 e^{ikz} \quad \text{and} \quad H_{xp} = \frac{E_0}{\eta} e^{ikz} . \quad (12)$$

In the positive  $z$  half space, the reflected fields as given by (10) are radiated. The ratio of the reflected field to the desired plane wave at  $z = 0$  is given by

$$\left. \frac{E_{ys}}{E_{yp}} \right|_{z=0} = \frac{1 - \Delta}{1 + \Delta} . \quad (13)$$

For  $\Delta$  equal to zero or infinity, the reflected field has the same magnitude as the desired plane wave and equal powers are radiated on each side of the  $z = 0$  plane. In other words, an electric current sheet by itself or a magnetic current sheet by itself radiates equally on both sides. However, a sheet of Huygen's sources ( $\Delta = 1$ ) produces no reflected field, and all of the power is radiated into the test zone ( $z < 0$ ). Of course, this result holds only for the infinite planar geometry of figure 5.

The solutions for the source currents in figures 3b and 4b are generally fairly difficult to obtain because the related scattering problems in figures 3a and 3b are difficult to solve. One special case of practical interest is when the perfect electric conductor in figure 3a is large compared to a wavelength. Then the physical optics approximation [18] yields the following simple result of  $\underline{J}_s$ :

$$\underline{J}_s = \begin{cases} 2 \hat{n} \times \underline{H}_p, & \text{illuminated area} \\ 0, & \text{shadowed area} \end{cases} . \quad (14)$$

As shown in figure 6, the near field of  $\underline{J}_s$  can be divided into three regions. The desired plane wave exists in the center, a transition zone exists along the shadow boundary, and a very small field exists outside the transition zone. The details of the transition zone will be covered in section 4, but the width  $d$  is on the order of  $\sqrt{\lambda z}$ . In the geometrical optics limit ( $\lambda \rightarrow 0$ ), the width of the transition zone shrinks to zero, and a sharp

shadow boundary exists. For nonzero  $\lambda$ , the field at large  $z$  eventually evolves into a spherical wave with inverse distance dependence.

### 3.3. Sampling and scanning considerations

Up to this point we have considered only continuous current distributions. If such current distributions are to be approximated by a phased array of discrete elements then sampling criteria must be considered in order to determine the number of elements required. In order to obtain some rough estimates, we consider the simple geometry shown in figure 7. The test zone has width  $D$  and is located at a distance  $R$  from the array. The array is of width  $W$ , and the elements have an interelement spacing  $s$ . We assume that  $W$  is large compared to a wavelength and that the smoothed current distribution can be approximated by (14). Since  $\hat{n}$  is constant for a planar surface,  $\underline{J}_s$  is constant in magnitude, and we are dealing with a uniform array.

If the plane wave is to be scanned in angle, then  $s$  must be less than  $\lambda/2$  to avoid grating lobes [4]. In order that the truncated plane wave include all of the test zone,  $W$  must be somewhat greater than  $D$  as seen in figure 7. The number of elements in one dimension  $N$  is thus given by

$$N \approx W/s > 2 D/\lambda \quad . \quad (15)$$

If we assume the same parameters in the orthogonal planar direction, then the total number of elements in the array  $N^2$  is given by

$$N^2 > 4(D/\lambda)^2 \quad (16)$$

For comparison, the total number of elements required for a spherical array for a test zone of diameter  $D$  can be computed as the product of the number of elevation samples  $N_\theta$  times the number of azimuthal samples  $N_\phi$  [6]. For large  $D/\lambda$ , this product is given by

$$N_\theta N_\phi \approx (\pi D/\lambda) (2\pi D/\lambda) = 2\pi^2 (D/\lambda)^2 \quad . \quad (17)$$

It is not surprising that the number of elements required for a spherical array in (17) is somewhat greater than the number of elements required for a planar array in (16). The spherical array allows the plane wave to be scanned over all angles in elevation and azimuth while the planar array allows scanning over somewhat less than a hemisphere. A possible means of increasing the scanning range is to use several planar arrays with different orientations. This idea has been discussed for the reciprocal case of near-field antenna measurements [19], but apparently has not been implemented.

If the plane wave is not to be scanned in angle, then the planar array in figure 7 is a broadside array, and the elements have uniform phase. In this case, the interelement spacing  $s$  can be increased to a full wavelength before grating lobes appear. The total number of elements required can then be reduced from  $4(D/\lambda)^2$  in (16) to  $(D/\lambda)^2$ . In practice this number can be reduced even further by allowing grating lobes outside the test region. In this case,  $s$  can be increased to [18]:

$$s = \lambda \sqrt{1 + 4R^2/(D+W)^2} < \lambda \sqrt{1 + (R/D)^2} . \quad (18)$$

Then  $N^2$  is reduced to:

$$N^2 > \frac{D^2}{\lambda^2 (1 + R^2/D^2)} . \quad (19)$$

Some of the numerical results of Schoessow [8] show grating lobes outside the test zone where he has used interelement element spacings greater than a wavelength.

The truncated plane wave produced by the planar array can be scanned in angle by introducing a linear phase shift to the elements. However, if the truncated plane wave is scanned too far, it will miss the test zone. By purely geometric considerations, the maximum scan angle  $\theta_{\max}$  is given by [18]:

$$\theta_{\max} = \tan^{-1} \left[ \frac{W - D}{2R} \right] . \quad (20)$$

This result is in agreement with the reciprocal problem of near-field antenna measurements where the far-field antenna pattern cannot be determined for angles larger than  $\theta_{\max}$  [20]. The result in (20) ignores diffraction effects, and a term of the order  $\sqrt{\lambda/R}$  should be subtracted if diffraction effects are important. If  $W$  is increased to infinity in (20), then  $\theta_{\max} = \pi/2$  and the plane wave can be scanned over a hemisphere. In order to cover a full sphere, the array must surround the test volume.

It has been noted that an alternative to actually building a phased array is to take a single element and step it through all of the element positions [21]. In this way the plane wave is never actually generated, but the response of the EUT is the sum of the separate responses properly weighted to yield a plane wave response. This method has the advantage of not requiring the potentially large number of elements as indicated by (16) and (17). Also, the requirement for accurate control of the amplitude and phase of a large number of elements is eliminated. The difficulty with this approach is that the sum of the responses is equal to the total plane wave response only if the EUT is linear, and this is not always true for strong fields [3]. The other point in favor of actually constructing the array is that the EUT response is obtained directly without further processing. Another interesting possibility of the constructed array is that it could yield the far-field radiated emissions pattern of an arbitrary source EUT if the array is operated in the receiving mode.

#### **4. Near fields of smooth current distributions**

Realistic near-field arrays of finite extent suffer from truncation effects at the edges of the array as indicated in figure 6. The simplest model for studying truncation effects is a smooth physical optics current distribution as given by (14) which is abruptly truncated at the edges of the array. For simplicity, we consider only planar current distribution, but the asymptotic method of analysis could also be used for curved surfaces. In section 4.1 we consider a simple two-dimensional geometry, and in section 4.2 we consider a more realistic three-dimensional geometry.

#### 4.1. Two-dimensional geometry

We consider a semi-infinite surface current shown in figure 8. The electric current distribution  $\underline{J}$  is given by (14):

$$\underline{J}(x') = \begin{cases} 2 \hat{z} \times \underline{H}_p & \left| \begin{array}{l} x = x' \\ z = 0 \end{array} \right. \\ 0 & , \quad x' > 0 \end{cases} \quad (21)$$

where

$$\begin{aligned} \underline{H}_p &= \underline{H}_0 e^{-jk_i \cdot \underline{\rho}} \quad , \\ \underline{k}_i &= k \hat{k}_i \quad , \quad \hat{k}_i = \hat{x} \sin \theta_i + \hat{z} \cos \theta_i \quad , \\ \underline{\rho} &= \hat{x} x + \hat{z} z \quad , \end{aligned}$$

and  $\theta_i$  is the incidence angle defined in figure 8. The electric and magnetic fields are most easily derived via the magnetic vector potential  $\underline{A}$  [10]:

$$\underline{A} = \int_{-\infty}^0 \underline{J}(x') G(|\underline{\rho} - \underline{\rho}'|) dx' \quad , \quad (22)$$

where

$$\begin{aligned} G(|\underline{\rho} - \underline{\rho}'|) &= \frac{1}{4j} H_0^{(2)}(k|\underline{\rho} - \underline{\rho}'|) \quad , \\ \underline{\rho}' &= \hat{x} x' \quad , \end{aligned}$$

and  $H_0^{(2)}$  is the zero order Hankel function of the second kind.

The integral in (22) is difficult to evaluate in general, but for sufficiently large values of  $kz$  it can be evaluated by asymptotic methods [22]. The total vector potential  $\underline{A}$  then can be written as the sum of two terms:

$$\underline{A} = \underline{A}_s + \underline{A}_e \quad . \quad (23)$$

$\underline{A}_s$  is the plane wave term which arrives via the direct ray from the stationary phase point as indicated in figure 8. It is derived in Appendix A, and the result is:

$$\underline{A}_s \sim \hat{z} \times \underline{H}_0 \frac{e^{-jk(x \sin \theta_i + z \cos \theta_i)}}{jk \cos \theta_i} U(\theta_i - \theta_e), \quad (24)$$

where

$$U(\theta_i - \theta_e) = \begin{cases} 1, & \theta_i - \theta_e > 0 \\ 0, & \theta_i - \theta_e < 0 \end{cases}$$

$$\sin \theta_e = x/\rho \quad \text{and} \quad \rho = \sqrt{x^2 + z^2}.$$

Because of the unit step function  $U$  in (24),  $\underline{A}_s$  exists only in the illuminated region to the left of the dashed line in figure 8.  $\underline{A}_s$  can also be thought of as the geometrical optics field which drops abruptly to zero to the right of the dashed line (shadow boundary) in figure 8. The edge diffraction term  $\underline{A}_e$  is also derived in Appendix A, and the result is

$$\underline{A}_e \sim \hat{z} \times \underline{H}_0 \frac{e^{-j(k\rho - \frac{\pi}{4})}}{jk \cos \theta_e \sqrt{\pi}} F_-(\nu) e^{j\nu^2} \text{sgn}(\theta_e - \theta_i), \quad (25)$$

where

$$\text{sgn}(\theta_e - \theta_i) = \begin{cases} +1, & \theta_e - \theta_i > 0 \\ -1, & \theta_e - \theta_i < 0 \end{cases}.$$

The Fresnel integral  $F_-$  and the argument  $\nu$  are defined in Appendix A. Both  $\underline{A}_p$  and  $\underline{A}_e$  are discontinuous at the shadow boundary ( $\theta_e = \theta_i$ ), but the sum of the two terms is continuous, as it should be.

At points which are not near the shadow boundary, the asymptotic form of the Fresnel integral [22] can be used in (25), and  $\underline{A}_e$  simplifies to

$$\underline{A}_e \approx \hat{z} \times \underline{H}_0 \frac{e^{-jk\rho} \text{sgn}(\theta_e - \theta_i)}{jk \sqrt{2\pi jk\rho} (\sin \theta_e - \sin \theta_i)}. \quad (26)$$

In the illuminated region ( $\theta_e < \theta_i$ ), the edge diffraction term  $\underline{A}_e$  will interfere constructively and destructively with the desired plane wave term  $\underline{A}_s$  and will cause ripples in amplitude and phase. Such ripples are very evident in the results of Bennett and Schoessow [5] and a Fourier analysis of the total field by Schoessow [8] has determined that the error field arrives primarily from the edges of the array. From (24) and (26), the ratio of undesirable edge diffraction term to the plane wave term is found to be

$$\frac{|\underline{A}_e|}{|\underline{A}_s|} \approx \frac{\cos \theta_i}{\sqrt{2\pi k\rho} |\sin \theta_e - \sin \theta_i|} . \quad (27)$$

The  $(k\rho)^{-1/2}$  dependence in (27) is characteristic of edge diffracted fields [22]. The expression in (27) can be used to determine the width of the transition zone from small field strength to full plane field strength as indicated in figure 6. If we assume that  $\theta_e$  and  $\theta_i$  are small and we require  $|\underline{A}_e/\underline{A}_s|$  be small outside the transition zone, then from (27) it follows that

$$\sqrt{2\pi k\rho} |\theta_e - \theta_i| \gg 1 . \quad (28)$$

The width  $d$  of the transition zone is approximately the arc distance  $2\rho|\theta_e - \theta_i|$ . From (28),  $d$  must satisfy

$$d = 2\rho|\theta_e - \theta_i| \gg 2\sqrt{\lambda\rho} . \quad (29)$$

Thus, the width  $d$  of the transition zone is somewhat greater than  $\sqrt{\lambda\rho}$ , and this result is in agreement with that of Turchin and Tseytlin [18].

The actual field components,  $\underline{H}$  and  $\underline{E}$ , are obtained by taking the following curl operations on  $\underline{A}$ :

$$\begin{aligned} \underline{H} &= \nabla \times \underline{A} \quad \text{and} \\ \underline{E} &= \frac{1}{j\omega\epsilon} \nabla \times \nabla \times \underline{A} , \end{aligned} \quad (30)$$

where  $\epsilon$  is the permittivity of free space. The details of the curl operations are carried out in Appendix A. In figures 9-14, we show some numerical results for the electric field as a function of  $x$ . The main purpose of these results is to illustrate the behavior of the field in the transition zone. The Fresnel integral, which is required for the evaluation of the edge diffracted fields, was evaluated by power series for small argument and asymptotic series for large argument [23].

In figures 9-12, the electric field is polarized in the  $y$  direction, and  $\underline{H}_0$  is given by

$$\underline{H}_0 = H_0 (\hat{x} \cos \theta_i - \hat{z} \sin \theta_i) . \quad (31)$$

In figure 9, the magnitude of the electric field is shown at two distances from the planar surface current. The distance  $z = 30 \lambda$  was chosen to match the example in the paper by Bennett and Schoessow [5]. In both cases, the field decays smoothly in the shadow region ( $x > 0$ ) and exhibits damped oscillations in the illuminated zone ( $x < 0$ ). As predicted by (29), the transition zone is wider for larger  $z$ . Phase results for the same cases are shown in figure 10. Results for magnitude and phase as a function of incidence angle  $\theta_i$  are shown in figures 11 and 12. Again, the geometrical optics results are shown as dashed lines. The transition zones are seen to widen for oblique angles.

In figures 13 and 14, the magnetic field is polarized in the  $y$  direction, and  $\underline{H}_0$  is given by

$$\underline{H}_0 = \hat{y} H_0 . \quad (32)$$

Thus, the electric field is polarized in the  $xz$ -plane. Figure 13 shows magnitude results for normal incidence ( $\theta_i = 0$ ). The existence of a small  $E_z$  component is due to diffraction. Figure 14 shows results for various values of  $\theta_i$ , and a larger value of  $|E_z|$  exists for oblique angles.

In figures 9, 10, and 13 and in (27), it is clear that the diffracted field decays rather slowly and causes undesirable ripple in the field in the

illuminated region. The reason for the slow decay is that the edge diffracted field decays only as  $(k\rho)^{-1/2}$  as seen in (27). The magnitude of the edge diffracted field can be decreased by tapering the current at the edge of the array ( $x' = 0$ ). To see this, we consider first the untapered result. The integral form of the edge diffracted field  $\underline{A}_e$  is

$$\underline{A}_e = - \int_0^{\infty} \underline{f}(x') e^{jkg(x')} dx' , \quad (33)$$

where  $\underline{f}$  and  $g$  are defined in (A2). For the case with no stationary points near zero or in the interval 0 to  $\infty$ , (33) can be integrated by parts to obtain [22]:

$$\underline{A}_e \sim \underline{f}(0) \frac{e^{jkg(0)}}{jkg'(0)} . \quad (34)$$

If we replace the abrupt transition in the current at  $x' = 0$  with a linear taper as in figure 15, then  $x'$  near zero  $\underline{f}$  in (33) is replaced by a tapered function  $\underline{f}_t$ :

$$\underline{f}_t(x') = \underline{f}(x') (-x'/L) , \quad (35)$$

where  $L$  is the approximate length of the taper as shown in figure 15. The tapered current is slightly smoothed at  $x' = L$  to avoid a discontinuity in the derivative. Since  $\underline{f}_t(0)$  is zero, the leading term in the asymptotic evaluation of (33) now is [22]:

$$\underline{A}_{et} \sim \frac{-\underline{f}'_t(0) e^{jkg(0)}}{(jk)^2 [g'(0)]^2} , \quad (36)$$

where

$$\underline{f}'_t(0) = -\underline{f}(0)/L.$$

Equation (36) can be written in the following form:

$$\underline{A}_{et} \sim \frac{1}{jKLg'(0)} \underline{A}_e , \quad (37)$$

where  $g'(0) = \sin \theta_e - \sin \theta_i$ . Thus, the diffracted field can be reduced by tapering if  $kL$  is large. This effect will be shown quantitatively in section 5.

#### 4.2. Three-dimensional geometry

In this section we treat the more realistic case of physical optics currents on a finite surface. The asymptotic methods which we will use to evaluate the field are applicable to curved surfaces, but for simplicity we will treat only planar surfaces. The theory has much in common with some of the earlier work on diffraction by apertures [24,25].

Consider first a general planar area as shown in figure 16 where the surface currents are given by the physical optics expression in (14). For high frequencies, the electric field (or the magnetic field) can be expanded in an asymptotic series of the following form [25]:

$$\underline{E} \sim \underline{E}_s + \underline{E}_e + \underline{E}_c, \quad (38)$$

where the three ray paths are shown in figure 16. For points not near the shadow boundary, the three terms have the following dependence on wave number  $k$  [25]:

$$\underline{E}_s \propto k^0, \quad \underline{E}_e \propto k^{-1/2}, \quad \text{and} \quad \underline{E}_c \propto k^{-1}. \quad (39)$$

$\underline{E}_s$  is the stationary phase contribution which yields the desired plane wave field.  $\underline{E}_e$  is an edge diffraction term which emanates from a stationary phase point on the edge of the surface and, in some cases, there could be multiple stationary points on the edge.  $\underline{E}_c$  is a corner diffraction term which emanates from a point where the tangent to the surface is discontinuous. For large  $k$ ,  $\underline{E}_c$  is usually negligible compared to  $\underline{E}_e$ , and we will not include  $\underline{E}_c$  in the field calculations in this section. The main objective is to determine how much degradation of the desired field  $\underline{E}_s$  is caused by the leading undesirable term  $\underline{E}_e$ .

We begin by setting up the general integral for the vector potential  $\underline{A}(\underline{r})$  in terms of the surface current  $\underline{J}(\underline{r}')$ :

$$\underline{A}(\underline{r}) = \frac{1}{4\pi} \iint_S \frac{\underline{J}(\underline{r}') e^{-jk|\underline{r} - \underline{r}'|}}{|\underline{r} - \underline{r}'|} dS . \quad (40)$$

We assume that the surface  $S$  is located in the  $xy$  plane and that  $\underline{J}$  is the physical optics current given by (14):

$$\underline{J}(\underline{r}') = \begin{cases} \hat{z} \times \underline{H}_p(\underline{r}'), & \underline{r}' \text{ on } S \\ 0, & \underline{r}' \text{ not on } S \end{cases} \quad (41)$$

where

$$\underline{H}_p(\underline{r}') = \underline{H}_0 e^{-jk_i \cdot \underline{r}'} \quad \text{and} \quad \underline{k}_i = \hat{k}_i k .$$

We can then write  $\underline{A}$  in a form convenient for asymptotic evaluation:

$$\underline{A}(\underline{r}) = \iint_S \underline{f} e^{jkg} dS , \quad (42)$$

where

$$\underline{f} = \frac{\hat{z} \times \underline{H}_0}{2\pi|\underline{r} - \underline{r}'|}$$

and

$$g = - (\hat{k}_i \cdot \underline{r}' + |\underline{r} - \underline{r}'|) .$$

Integrals of the type in (42) can be evaluated as the sum of two terms [22]:

$$\underline{A} \sim \underline{A}_s + \underline{A}_e . \quad (43)$$

$\underline{A}_s$  is the stationary phase term which yields the desired plane wave field within the illuminated region.

In order to evaluate the edge diffraction term  $\underline{A}_e$ , we write (42) in the following form:

$$\underline{A} = \int_0^L \int_0^{\alpha(u_2)} \underline{f} e^{jkg} du_1 du_2, \quad (44)$$

where  $u_1$ ,  $u_2$ ,  $L$ , and  $\alpha$  are defined in figure 17. The edge diffraction contribution  $\underline{A}_e$  is essentially the negative of the integral in (44) for  $u_1 > \alpha$ :

$$\underline{A}_e \sim - \int_0^L \int_{\alpha(u_2)}^{\infty} \underline{f} e^{jkg} du_1 du_2. \quad (45)$$

The  $u_1$  integration in (45) can be cast into a Fresnel integral form as in (25) for the one-dimensional integral. The  $u_2$  integration is done by stationary phase, and the general result is [22]:

$$\begin{aligned} \underline{A}_e \sim & \pm \frac{|g_{u_1}|}{g_{u_1}} \underline{f} e^{jkg} e^{\mp jv^2} \sqrt{\frac{2}{k|g_{u_1}u_1|}} F_{\pm}(v) \cdot \\ & \cdot \left( \frac{k}{2\pi} |g_{u_2}u_2| \right)^{-1/2} e^{j \frac{\pi}{4} \text{sgn}(g_{u_2}u_2)} \Bigg|_{\substack{u_1 = \alpha(u_{2e}) \\ u_2 = u_{2e}}}, \end{aligned} \quad (46)$$

$$g_{u_1 u_1}[\alpha(u_{2e}), u_{2e}] \begin{matrix} > 0 \\ < 0 \end{matrix},$$

where

$$v = \sqrt{\frac{k}{2|g_{u_1}u_1|}}$$

$$g_{u_2}[\alpha(u_{2e}), u_{2e}] = 0 .$$

In (46), subscripts  $u_1$  or  $u_2$  imply differentiation, and all quantities are evaluated at  $u_2 = u_{e2}$  which is the stationary point determined from  $g_{u_2} = 0$ . If there is more than one stationary edge point, then (46) becomes a summation of the contributions from each point.

We now consider the specific example of a rectangular surface as shown in figure 18. For simplicity, the plane wave is scanned only in the  $xz$ -plane, and the propagation direction  $\hat{k}_i$  is given by

$$\hat{k}_i = \hat{z} \cos \theta_i + \hat{x} \sin \theta_i , \quad (47)$$

where  $\theta_i$  is the incidence angle as shown in figure 18. Since the perimeter is made up of four straight segments, there can be up to four stationary edge points. The asymptotic evaluation of the fields is tedious, and the details are given in Appendix B.

Results for both  $E_y$  polarization and  $H_y$  polarization are derived in Appendix B, but in the following numerical examples we consider only  $E_y$  polarization. The calculations have shown that polarization effects are fairly minor for cases where  $a$ ,  $b$ , and  $z$  are large compared to  $\lambda$ . For our numerical results, we choose  $a/\lambda = b/\lambda = 30$ . These dimensions correspond rather closely to those in the numerical results of Bennett and Schoessow [5]. In figure 19, we show the magnitude of the electric field along a center cut ( $y/\lambda = 15$ ) at two distances from the current sheet. The geometrical optics approximation is shown for comparison. The field quality is seen to deteriorate at the larger distance, and this effect is predicted by the angular dependence of the edge diffraction terms. The magnitude of the ripple at  $z/\lambda = 30$  is somewhat larger than that computed by Bennett and Schoessnow [5] for a synthesized array, but their analysis involved only a one-dimensional array. Our two-dimensional current sheet is more physically realistic because it includes diffraction from edges in both  $x$  and  $y$  directions. It is

the constructive and destructive interference of the four edge-diffracted rays with the plane wave that produces the complicated interference patterns in figures 19 - 21.

Figure 20 shows the effect of scanning the plane wave. The quality of the plane wave is seen to decrease as the scan angle  $\theta_i$  is increased, and the field is no longer symmetrical about the center of the plane wave zone. Figure 21 shows the magnitude of the electric field on a cut off the center line ( $y/\lambda = 5$ ). The ripple in  $E_y$  is slightly greater than that along the center line in figure 19. A small  $E_z$  component is produced by diffraction from edges 1 and 3.

Other calculations have produced similar results, and the main problem is the large ripple caused by edge diffraction. As indicated in the previous section, edge diffraction is strong because of the abrupt truncation of the current at the edges. This edge diffraction could be reduced by tapering the current near the edges as demonstrated in (37), but taper was not investigated for the geometry in figure 18. It is investigated in the following section on arrays.

## 5. Near fields of arrays

The numerical results for smooth current distributions in section 4 show the effects of truncating the radiating surface. In this section, we analyze discrete arrays in order to study the effect of element spacing. This effect is analogous to sampling in the reciprocal problem of near-field scanning [20]. Since we are not yet prepared to consider the details of the array elements, we choose fairly simple array elements for the analysis. Hertzian electric dipoles are the array elements in section 5.1, and Huygens' sources [15] are the array elements in section 5.2. In each case, the effect of tapering the amplitude of the elements at the edge of the array is studied, and the amplitude of the ripple field in the test volume is substantially reduced.

### 5.1. Electric dipole array

In this section we analyze a planar array of electric dipole elements. For simplicity, we consider Hertzian dipoles, but there is little difference in the far-field pattern of Hertzian dipoles and finite dipoles of length up to a half wavelength [26]. It is assumed that the test zone is at least a wavelength from the array so that only the far-field terms of a given element are required. However, the test zone will normally be located in the near field of the entire array.

The geometry of the rectangular array is shown in figure 22. The dipole elements are located at  $x_i, y_j$  which are given by

$$\begin{aligned} x_i &= \Delta x'(i - 1/2), \quad i = 1, 2, \dots, N_x \\ y_j &= \Delta y'(j - 1/2), \quad j = 1, 2, \dots, N_y \end{aligned} \quad (48)$$

where

$$\Delta x' = a/N_x, \quad \Delta y' = b/N_y,$$

and the total number of elements is  $N_x N_y$ . The fields of a single element ( $\underline{E}_{ij}, \underline{H}_{ij}$ ) of arbitrary orientation in the  $xy$ -plane are derived in Appendix C. The total fields of the array ( $\underline{E}, \underline{H}$ ) are given by double summations:

$$\underline{E} = \sum_{i=1}^{N_x} \sum_{j=1}^{N_y} \underline{E}_{ij}, \quad (49)$$

$$\underline{H} = \sum_{i=1}^{N_x} \sum_{j=1}^{N_y} \underline{H}_{ij},$$

where  $\underline{E}_{ij}$  is given by (C4) and  $\underline{H}_{ij}$  is given by (C3).

For simplicity, we consider the magnetic field of the plane wave to be polarized in the x direction and propagating in the positive z direction:

$$\underline{H}_p = \hat{x} H_0 e^{-jkz} . \quad (50)$$

From (14), the smoothed surface current density is

$$\underline{J}_s = 2 \hat{z} \times \underline{H}_p = \hat{y} 2 H_0 . \quad (51)$$

The dipole moment  $\underline{p}_{ij}$  is the surface current density times the area of the patch as indicated in figure 22:

$$\underline{p}_{ij} = \Delta x' \Delta y' \underline{J}_s = \hat{y} 2 \Delta x' \Delta y' H_0 . \quad (52)$$

The fields of uniform arrays have been calculated from (49), (52), (C2), and (C3), and some results are shown in figure 23. The parameters,  $a = b = 30 \lambda$ , were chosen to match the examples in section 4.2 and the earlier work of Bennett and Schoessow [5]. Only half of the center cut for  $y/\lambda < 15$  is shown since the fields are symmetrical about  $y/\lambda = 15$ . For an element spacing,  $\Delta x' = \Delta y' = 1.5 \lambda$ , large oscillations exist, and the quality of the field is clearly not adequate. This is to be expected because the element spacing requirement discussed in section 3.3 has been exceeded. The results are much better for a spacing of one wavelength where most of the ripple is now caused by edge diffraction which cannot be reduced simply by reducing the element spacing.

The analytical result in (37) indicates that the edge-diffracted field can be reduced by tapering the amplitude of the elements near the edge of the array.

To explore the effectiveness of tapering, we utilize a linear taper function  $t_\lambda$  defined by:

$$t_{\lambda}(i, T, N) = \begin{cases} \frac{i}{T+1} & , \quad i \leq T \\ 1 & , \quad T < i < N+1-T \\ \frac{N+1-i}{T+1} & , \quad i \geq N+1-T \end{cases} \quad (53)$$

where  $N$  is the total number of elements in a row and  $T$  is the number of tapered elements on each end of the row. For example, for  $T = 1$ ,  $t_{\lambda} = 1/2$  for  $i = 1$  or  $N$ , and  $t_{\lambda} = 1$  for all other elements. For  $T = 0$ ,  $t_{\lambda}$  equals unity for all elements. The linear taper function can be used in both the  $x'$  and  $y'$  directions so that all edges of the array have the same taper. Thus, for the tapered array, we replace  $\underline{p}_{ij}$  of (52) by:

$$\underline{p}_{ij} = \hat{y}^2 \Delta x' \Delta y' H_0 t_{\lambda}(i, T_x, N_x) t_{\lambda}(j, T_y, N_y) . \quad (54)$$

The use of two taper parameters,  $T_x$  and  $T_y$ , in (54) allows for the possibility of different tapers in the  $x'$  and  $y'$  directions, but in all our calculations we assume  $T_x = T_y = T$ .

In figure 24, we examine the effect of the taper parameter  $T$  when the interelement spacing is a half wavelength. The untapered result ( $T = 0$ ) is similar to the result in figure 23 when the interelement spacing is  $\lambda$  except that the ripple has been slightly reduced. When  $T$  is increased to 2 and 6 in figure 24, the ripple is seen to decrease markedly, and the field is quite smooth near the center of the array. The main disadvantage of the taper is that the width of the test zone is narrowed as the number of tapered elements is increased. Thus, the best choice of  $T$  depends on the quality of the plane wave and the size of the test zone required.

The number of elements required for the array in figure 24 is 3600 ( $N_x N_y = 60 \times 60$ ), and this number is so large because the electrical size of the test zone is so large. It is only at microwave frequencies where the test zone must be electrically large for EUT's of typical dimensions (on the order

of meters). Consider the case in figure 25 where the array dimensions have been decreased by a factor of 10 ( $a = b = 3 \lambda$ ). In this case, the number of array elements is reduced to 36 ( $N_x N_y = 6 \times 6$ ), but the field shows an amplitude taper across the test zone. (The flat geometrical optics field is shown for comparison.) In this case, the linear taper does not really help the problem. It is likely that some other type of nonuniform excitation would provide an improvement, but it is not obvious how to find the best element excitations. A general numerical method is probably required, and a promising method is described in section 6. The preliminary conclusion is that the linear edge taper is useful only for reducing the edge-diffracted field of electrically large arrays.

## 5.2. Huygens' source array

In this section we analyze a planar array of Huygen's sources. A Huygen's source [15] is essentially a small portion of a plane wave, and it is an approximate representation of a small aperture antenna [16] such as a horn or an open-ended waveguide. It has a broad pattern in the forward direction and a null in the backward direction. For this reason, it is a better aperture antenna model than single electric or magnetic dipoles which have equal radiation in the front and back directions. The directivity of a Huygens' source is 3 (or 4.77 dB) which is twice that of a Hertzian dipole, but is less than that of an open-ended rectangular waveguide [27].

Figure 26 shows the crossed electric and magnetic dipoles which constitute a Huygen's source. For simplicity, we assume that the plane wave is propagating in the positive  $z$  direction and the electric field is polarized in the  $x$  direction:

$$\begin{aligned} \underline{E}_p &= \hat{x} E_{ox} e^{-jkz} , \\ \underline{H}_p &= \hat{y} \frac{E_{ox}}{\eta} e^{-jkz} . \end{aligned} \tag{55}$$

From the equivalence principle, the electric and magnetic dipole moments,  $\underline{p}_{ij}$  and  $\underline{m}_{ij}$ , are [15]:

$$\begin{aligned}\underline{p}_{ij} &= - \hat{x} \frac{E_{0x}}{\eta} \Delta x' \Delta y' , \\ \underline{m}_{ij} &= - \hat{y} E_{0x} \Delta x' \Delta y' .\end{aligned}\tag{56}$$

The far fields of a Huygens' source have been given in spherical coordinates [15], but in Appendix D we derive the Cartesian components.

The individual elements are again located as indicated in (48) and in figure 22. The fields are double summations:

$$\begin{aligned}\underline{E} &= \sum_{i=1}^{N_x} \sum_{j=1}^{N_y} \underline{E}_{ij} , \\ \underline{H} &= \sum_{i=1}^{N_x} \sum_{j=1}^{N_y} \underline{H}_{ij} ,\end{aligned}\tag{57}$$

where  $\underline{E}_{ij}$  and  $\underline{H}_{ij}$  are given by (D6). In figure 27, the normalized electric field strength on a center cut is shown for two different interelement spacings. As with the dipole array, a spacing of  $1.5 \lambda$  is too large, and the field has unacceptably large ripples.

In order to examine the effect of edge tapering, we again apply a linear taper to the edge elements. Thus, for the tapered array, we replace  $\underline{p}_{ij}$  and  $\underline{m}_{ij}$  of (56) by

$$\begin{aligned}\underline{p}_{ij} &= - \hat{x} \frac{E_{0x}}{\eta} \Delta x' \Delta y' t_{\lambda}(i, T_x, N_x) T_{\lambda}(j, T_y, N_y) , \\ \underline{m}_{ij} &= - \hat{y} E_{0x} \Delta x' \Delta y' t_{\lambda}(i, T_x, N_x) t_{\lambda}(j, T_y, N_y) ,\end{aligned}\tag{58}$$

where  $T_\lambda$  is given by (53). For the example in figure 28,  $T_x = T_y = T$ . The decrease in field ripple is comparable to that for the tapered dipole array in figure 24. The case for  $T = 0$  represents a uniform array and, in all cases, the interelement spacing is  $\lambda/2$ . This spacing provides a slight decrease in ripple for the uniform array as compared to the case for a spacing of  $\lambda$  in figure 27.

In summary, the use of edge tapering for an array of Huygens' sources decreases the edge-diffracted field as it did for the array of dipole sources. Thus, a large array with tapering provides a high quality field over a large area, but requires a large number of elements. The improvement of the field quality in going from a uniform to a tapered array might have implications for the reciprocal problem of near-field antenna measurements [18] when only a finite scan area [25] is used. Rather than abruptly truncating the scan, some sort of tapering process at the edge of the scan area [28] might be helpful.

## 6. Near-field array synthesis

The results for tapered arrays in section 5 indicate that large improvements over uniform arrays are possible. The linear edge tapering which was examined in section 5 was based on reducing the edge-diffracted field according to the analysis in section 4.1. The question naturally arises as to whether other types of tapering or completely different source distributions might yield better results. The goal of this section is to develop a general method of near-field array synthesis which will yield an optimum source distribution.

The subject of antenna array synthesis is well developed for conventional far-field applications [29,30], but near-field applications raise new difficulties. First, the convenient Fourier transform relationship which exists between the source distribution and the far-field pattern is not available for near fields, particularly for arbitrary geometries. Second, far-field synthesis involves approximating the field over a surface of infinity whereas our near-field application requires a specified near field within a test volume.

In section 6.1, a uniqueness theorem is derived which allows us to specify the desired fields on the surface surrounding the test volume. In section 6.2, this theorem is used to derive a synthesis procedure based on surface fields rather than volume fields. The general numerical synthesis method is based on earlier work by Mautz and Harrington [31] and does not require the far-field Fourier transform relationship. The method minimizes the mean square error in the fields and imposes a constraint on the source norm. The source norm constraint is useful in keeping the fields small outside the test volume. Section 6.3 applies the method to a planar array of line sources with good results.

### 6.1. A new uniqueness theorem

Uniqueness theorems tell what surface field information is required to uniquely determine the fields within the enclosed volume. The classical uniqueness theorem for time-harmonic fields [10] states that the tangential electric (or magnetic) field uniquely determines the fields in the enclosed volume. Unfortunately, this theorem breaks down for lossless media, such as free space. A more general uniqueness theorem from Müller [32] states that the tangential electric and magnetic fields are sufficient to uniquely specify the fields in the enclosed volume. The proof of the theorem requires continuously differentiable constitutive parameters, but does not require loss. Thus, it is applicable for our free space geometry.

In near-field synthesis problems, it is not as convenient to specify both the tangential electric and magnetic fields as it would be to specify a single quantity. A single quantity which has been found to uniquely determine the fields in the enclosed volume is the tangential vector  $\underline{F}$  which is defined as:

$$\underline{F} = \underline{E}_{\text{tan}} - \eta \hat{n} \times \underline{H} , \quad (59)$$

where  $\underline{E}_{\text{tan}}$  is the tangential electric field,  $\eta$  is the free-space impedance, and  $\hat{n}$  is the inward unit normal as shown in figure 29. A uniqueness theorem for  $\underline{F}$  can be stated as follows. "The fields in a source-free region are

specified by  $\underline{F}$  over the boundary." This theorem can be stated in the following equivalent form. "If  $\underline{F} = 0$  on the surface of a source-free region, then  $\underline{E} = \underline{H} = 0$  within the enclosed region." The meaning of the second statement is that if there is no change in  $\underline{F}$ , then there can be no change in  $\underline{E}$  and  $\underline{H}$  throughout the enclosed region. These are the difference fields which Harrington [10] utilized, and if they are zero, then only one unique field solution exists.

The proof of the second form of the theorem goes as follows. First, scalar multiplication of the equation,  $\underline{F} = 0$ , by its complex conjugate,  $\underline{F}^* = 0$ , yields

$$(\underline{E}_{\text{tan}} - \eta \hat{n} \times \underline{H}) \cdot (\underline{E}_{\text{tan}}^* - \eta \hat{n} \times \underline{H}^*) = 0 . \quad (60)$$

If the scalar multiplication in (60) is carried out term by term, then

$$|\underline{E}_{\text{tan}}|^2 + \eta^2 (\hat{n} \times \underline{H}) \cdot (\hat{n} \times \underline{H}^*) - \eta [\underline{E}_{\text{tan}} \cdot (\hat{n} \times \underline{H}^*) + \underline{E}_{\text{tan}}^* \cdot (\hat{n} \times \underline{H})] = 0 . \quad (61)$$

Using some vector identities, (61) can be written:

$$|\underline{E}_{\text{tan}}|^2 + \eta^2 |\underline{H}_{\text{tan}}|^2 + 2 \eta R_e [\hat{n} \cdot (\underline{E} \times \underline{H}^*)] = 0 , \quad (62)$$

where  $R_e$  indicates the real part. We now integrate (62) over the closed surface  $S$ :

$$\oint_S (|\underline{E}_{\text{tan}}|^2 + \eta^2 |\underline{H}_{\text{tan}}|^2) dS + 2 \eta R_e \oint_S \hat{n} \cdot (\underline{E} \times \underline{H}^*) dS = 0 . \quad (63)$$

The second integral in (63) is the real part of the Poynting vector integrated over a closed surface. Since the interior region is source free, this integral must be greater than or equal to zero [10]:

$$2\eta R_e \oint_S \hat{n} \cdot (\underline{E} \times \underline{H}^*) dS \geq 0 \quad (64)$$

All quantities in the first integral are either positive or zero. Thus, the only way for (63) to be satisfied is for both  $\underline{E}_{\text{tan}}$  and  $\underline{H}_{\text{tan}}$  to be zero:

$$\underline{E}_{\text{tan}} = \underline{H}_{\text{tan}} = 0 \text{ on } S. \quad (65)$$

To this point, we have shown that if  $\underline{F} = 0$ , then  $\underline{E}_{\text{tan}} = \underline{H}_{\text{tan}} = 0$  on  $S$ . Müller [32] has shown that (65) implies that  $\underline{E} = \underline{H} = 0$  inside  $S$ . Thus the proof is complete.

Although we initially assumed that  $\eta$  in (59) was the impedance of free space, the proof of the uniqueness theorem requires only that  $\eta$  be some positive quantity. For the special case of a lossless medium, the second integral in (63) is identically zero:

$$R_e \oint_S \hat{n} \cdot (\underline{E} \times \underline{H}^*) dS = 0. \quad (66)$$

In this case, all that is required is that  $\eta^2$  be positive. Consequently,  $\eta$  could be any positive or negative real quantity (but not zero). This freedom to choose  $\eta$  positive or negative real corresponds to the positive or negative real  $\alpha$  in the combined field integral equation of Mautz and Harrington [33]. For our near-field synthesis procedure which follows, we take  $\eta$  to be the free-space impedance in order to equalize the importance of the electric and magnetic fields. In order to illustrate the utility of the function  $\underline{F}$ , an example is shown in Appendix E where  $\underline{E}_{\text{tan}}$  (or  $\underline{H}_{\text{tan}}$ ) is not sufficient to determine the interior fields, but  $\underline{F}$  is sufficient.

An interesting feature of the function  $\underline{F}$  is that it might have significance for measurements of the fields in a region. One way to determine the fields in a source-free region, as in figure 29, would be to probe the fields directly throughout the volume. For an accurate field characterization, this

would require on the order of  $(L/\lambda)^3$  measurements of the three components of a vector field (E or H).  $L$  is some linear dimension of the region. In principle, the same field information is available from measurements of F over the surface  $S$ . This would require only on the order of  $(L/\lambda)^2$  measurements of the two components of F. Each component of F involves an orthogonal component of E and H, and a special loop antenna probe [34] could obtain these two components simultaneously.

## 6.2. Least squares analysis

The general configuration for the synthesis problem is shown in figure 30. The sources produce fields within the test volume, but we choose to work with the tangential fields on the surface  $S$ . A symbolic relationship between the sources  $s$  and the field  $F$  on the surface  $S$  can be written:

$$T s = F, \quad (67)$$

where  $T$  is a linear operator. We assume that  $T$  is known which means that we know how to compute the fields given the sources (the forward problem). We follow the method of Mautz and Harrington [31], but the details and some of the notation are different because we are working with near fields and arbitrary geometries.

The problem is made discrete from the start and cast into matrix form:

$$[T] [s] = [F] . \quad (68)$$

$[s]$  is an  $N \times 1$  source column matrix, and the scalar elements  $s_j$  are typically input currents or voltages to antennas:

$$[s]_{N \times 1} = \begin{bmatrix} s_1 \\ s_2 \\ \vdots \\ s_N \end{bmatrix} . \quad (69)$$

$[F]$  is an  $M \times 1$  column matrix, and the elements are vectors which are orthogonal to  $\hat{n}$ :

$$[F]_{M \times 1} = \begin{bmatrix} \underline{F}_1 \\ \underline{F}_2 \\ \vdots \\ \underline{F}_M \end{bmatrix}, \quad (70)$$

where

$$\underline{F}_i = \hat{u}_1 F_{1i} + \hat{u}_2 F_{2i}.$$

$\hat{u}_1$  and  $\hat{u}_2$  are tangential vectors as shown in figure 30. In terms of the electric and magnetic fields  $\underline{F}_i$  is given by

$$\underline{F}_i = (\underline{E}_{\text{tan}} - n \hat{n} \times \underline{H}) \Big|_{\underline{r} = \underline{r}_i}. \quad (71)$$

$\underline{r}_i$  is the position vector of the  $i^{\text{th}}$  point as shown in figure 30.  $[T]$  is an  $M \times N$  rectangular matrix of vectors.

$$[T]_{M \times N} = \begin{bmatrix} \underline{T}_{11} & \underline{T}_{12} & \cdots & \underline{T}_{1N} \\ \underline{T}_{21} & & & \vdots \\ \vdots & & & \vdots \\ \underline{T}_{M1} & \cdots & \cdots & \underline{T}_{MN} \end{bmatrix} \quad (72)$$

The element  $\underline{T}_{ij}$  is the vector  $\underline{F}_i$  produced by source  $s_j = 1$  when all other source elements are zero.

In the synthesis problem, the right side of (68) is set equal to the desired column matrix:

$$[T] [s] \approx [P], \quad (73)$$

where

$$\underline{P}_i = (\underline{E}_p \tan - \eta \hat{n} \times \underline{H}_p) \Big|_{\underline{r} = \underline{r}_i}$$

and  $\underline{E}_p$  and  $\underline{H}_p$  are the plane wave fields given by (1). The method is actually more general, and  $[P]$  could be a column matrix of any desired field values. Since  $[P]$  is an  $M \times 1$  column matrix of two-component vectors and  $[s]$  is an  $N \times 1$  column matrix of scalars, (73) actually represents  $2M$  equations in  $N$  unknowns. Normally  $2M$  is greater than  $N$ , and (73) can only be solved approximately. The least squares solution to (73) is [31]:

$$[s] = [[\tilde{T}]^* [T]]^{-1} [\tilde{T}]^* [P] , \quad (74)$$

where the tilde denotes transpose. Matrix multiplication in (74) and in the following equations has the usual meaning. Whenever the elements multiplied together are vectors, the dot product is understood. The solution for  $[s]$  in (74) minimizes the quantity:

$$\|[F] - [P]\|^2 = \sum_{m=1}^M |F_m - P_m|^2 , \quad (75)$$

where  $[F]$  is given by (68). In some cases, (74) provides a useful solution; but in other cases, the norm of  $[s]$  is large. Such solutions usually produce large fields outside the test volume where small fields are desirable.

In cases where the source norm is large, a more useful solution can be obtained by minimizing

$$\varepsilon_c = \|[F] - [P]\|^2 \quad (76)$$

with a constraint on the source norm

$$\|[s]\|^2 \leq C , \quad (77)$$

where

$$\|[s]\|^2 = \sum_{n=1}^N |s_n|^2 .$$

C is a positive constant to be chosen. The simultaneous solution to (76) and (77) has been derived by Mautz and Harrington [31], and we give only their final results.

The solution requires the eigenvalues  $\lambda_i$  and the eigenvectors  $[\phi]_i$  which satisfy

$$[\tilde{T}]^* [T] [\phi]_i = \lambda_i [\phi]_i . \quad (78)$$

The matrix  $[\tilde{T}]^* [T]$  is Hermitian, and efficient computer codes [35] are available for computing the eigenvalues and eigenvectors. The constrained solution for  $[s]$  is [31]:

$$[s] = \sum_{i=1}^N \frac{C_i}{\lambda_i + \alpha} [\phi]_i , \quad (79)$$

where

$$C_i = [\phi]_i^* [\tilde{T}]^* [P] .$$

The Lagrange multiplier  $\alpha$  satisfies

$$C - \sum_{i=1}^N \frac{|C_i|^2}{(\lambda_i + \alpha)^2} = 0 . \quad (80)$$

(80) is a monotonically decreasing function in  $\alpha$  which is real and positive, and the equation is easily solved numerically for  $\alpha$ . If  $\alpha$  is set equal to zero, then (77) gives the unconstrained solution for  $[s]$  which is the eigenvector expansion of (74). It has been shown [31] that as C is decreased, both  $\alpha$  and the error  $\epsilon_C$  increase. However, it is often the case that large decreases in the source norm can be achieved with only small increases in the error  $\epsilon_C$ .

### 6.3. Line source example

In order to demonstrate the effectiveness of the synthesis technique, we consider the two-dimensional problem shown in figure 31. An array of y-directed electric line sources is located in the  $z = 0$  plane, and a rectangular test volume is centered about  $z = z_0$  on the  $z$  axis. All quantities are independent of  $y$ . The two-dimensional geometry was chosen for simplicity, but the line source array problem is not entirely academic. For example, Bennett and Muntanga [7] have used a slotted waveguide to approximate a line source in plane wave synthesis, and their measurements show that the fields are nearly uniform in the  $y$  direction.

We consider only the broadside case where the plane wave is propagating in the positive  $z$  direction. Thus, the desired plane wave fields,  $\underline{E}_p$  and  $\underline{H}_p$ , are given by

$$\underline{E}_p = \hat{y} E_{py} \quad \text{and} \quad \underline{H}_p = \hat{x} H_{px}$$

where 
$$E_{py} = E_0 e^{-jkz} \quad (81)$$

and 
$$H_{px} = - (E_0/\eta) e^{-jkz} .$$

For the geometry in figure 31, the elements of the matrices  $[T]$ ,  $[P]$ , and  $[F]$  are  $y$ -component vectors rather than two-component vectors. Thus we have a scalar problem, and the matrix  $[P]$  is:

$$[P] = \begin{bmatrix} P_1 \\ P_2 \\ \vdots \\ P_i \\ \cdot \\ P_M \end{bmatrix} , \quad (82)$$

where

$$P_i = [E_{py} - \eta \hat{y} \cdot (\hat{n} \times \hat{x}) H_{px}] \Big|_{\substack{x = x_i \\ z = z_i}} .$$

By using a vector identity and (81), we can rewrite  $P_i$ :

$$P_i = E_0 (1 + \hat{n} \cdot \hat{z}) e^{-jkz_i} \quad (83)$$

The value of  $\hat{n} \cdot \hat{z}$  depends on which side of the test volume the point is located. On side 1,  $\hat{n} \cdot \hat{z} = 1$ , on side 3,  $\hat{n} \cdot \hat{z} = -1$ , and on sides 2 and 4,  $\hat{n} \cdot \hat{z} = 0$

The array consists of  $2N$  line sources with equal spacings  $d$  as shown in figure 31. Since the desired field is symmetrical in  $x$ , the array is symmetrical. The  $j^{\text{th}}$  element is located in the  $z = 0$  plane at  $x'_j$  given by

$$x'_j = \pm d(j - \frac{1}{2}) , \quad j = 1, \dots, M . \quad (84)$$

(The integer  $j$  should not be confused with imaginary  $j = \sqrt{-1}$ ) The source matrix  $[s]$  consists of the unknown line currents:

$$[s] = \begin{bmatrix} I_1 \\ I_2 \\ \vdots \\ I_j \\ \vdots \\ I_N \end{bmatrix} . \quad (85)$$

The  $[T]$  matrix is an  $M \times N$  matrix of scalars:

$$[T] = \begin{bmatrix} T_{11} & T_{12} & \dots & \dots & T_{1N} \\ T_{21} & & & & \vdots \\ \vdots & & & & \vdots \\ T_{M1} & \dots & \dots & \dots & T_{MN} \end{bmatrix},$$

where

(86)

$$T_{ij} = [E_{yj} - \eta \hat{y} \cdot (\hat{n} \times \underline{H}_j)] \Big|_{\substack{x = x_i \\ z = z_i \\ I_j = 1}}$$

$E_{yj}$  and  $\underline{H}_j$  are the electric and magnetic fields produced by unit line sources at  $x_j^{\pm} = \pm d(j - 1/2)$ . The specific forms of  $E_{yj}$ ,  $\underline{H}_j$ , and  $T_{ij}$  are given in Appendix F

A computer program was written to compute the least squares solution for the source matrix  $[s]$  with constraint by (79) and without constraint by (74). The Lagrange multiplier  $\alpha$  required in (79) was determined from (80) by Newton's method [36]. The solution of (74) was obtained from the QR decomposition [37] of  $[T]$ . As a check on the two methods, the solution of (79) with  $\alpha = 0$  was compared with the solution of (74) and, in all cases, the  $[s]$  matrix agreed to at least 5 significant figures

The solution of (80) for  $\alpha$  requires a constraint parameter  $C$  as defined by (77). A good value for  $C$  can be obtained from the physical optics approximation for  $[s]$ . From (14) and (81), the smoothed current density  $\underline{j}$  is given by

$$\underline{J} = - \hat{y} \ 2 \ E_0 / \eta \ . \quad (87)$$

For an interelement spacing of  $d$ , this results in an  $[s]$  matrix of uniform current elements  $I_u$ :

$$[s] \approx \begin{bmatrix} I_u \\ I_u \\ \vdots \\ I_u \end{bmatrix} \ , \quad I_u = - 2 \ d \ E_0 / \eta \ . \quad (88)$$

If we require that the norm of the synthesized solution be no greater than that of the uniform solution in (88), then  $C$  is given by:

$$C = N \ |I_u|^2 \ . \quad (89)$$

Other values of  $C$  might be more appropriate in some cases, and the computer program allows any value of  $C$ . However, all of the numerical results in this section utilize the value given by (89).

The synthesized solution for the currents was found to be insensitive to the number of surface points  $M$  (equals the number of equations) so long as the points are spaced less than  $\lambda/2$ . The points are equally spaced in  $u$  over the range from  $0$  to  $A + B$ , and the spacing  $\Delta u$  is given by

$$\Delta u = (A + B) / M \ . \quad (90)$$

The locations of the points are

$$u_i = \Delta u \ (i - 1/2) \ , \quad i = 1, 2, \dots, M \ . \quad (91)$$

For cases where the fields are not symmetrical (for example, a scanned plane wave), the points must be distributed over the entire perimeter.

The numerical results in figures 32 - 40 apply to a square test volume which is four wavelengths on a side ( $A = B = 4 \lambda$ ). In figures 32 - 34, the spacing  $d = \lambda/2$ , the number of elements  $2N = 12$ , and  $z_0 = 4 \lambda$ . The unconstrained currents in figure 32 are quite large and variable, whereas the constrained currents are much closer to those of a uniform array. The value of the uniqueness function  $F_y$  as given by (71) is shown over half the perimeter in figure 33. The curves are discontinuous at  $u = A/2$  and  $u = B + A/2$  because  $\hat{n}$  is discontinuous at those points. For comparison, we define a normalized squared error  $\epsilon_n$ :

$$\epsilon_n = \frac{\| [F] - [P] \|^2}{\| [P] \|^2} = \frac{\sum_{i=1}^M |F_{yi} - P_i|^2}{\sum_{i=1}^M |P_i|^2}, \quad (92)$$

where  $F_{yi}$  is the actual value of  $F_y$  at the  $i^{\text{th}}$  point and  $P_i$  is the desired plane wave value as given by (83). For the uniform array,  $\epsilon_n = 6.24 \times 10^{-2}$ ; for the constrained array,  $\epsilon_n = 4.35 \times 10^{-3}$ ; and for the unconstrained array,  $\epsilon_n = 5.52 \times 10^{-4}$ . The unconstrained array looks the most attractive from the error standpoint, but the difficulty with the unconstrained array is shown in figure 34 where the electric field is actually larger outside the test volume than inside. This feature is undesirable both because of wasted power and because of the possibility of reflections from objects outside the test volume. The constrained array has a fairly uniform field in the test volume, and the external field falls off at about the same rate as the field of a uniform array. The results for other values of  $z$  and for the magnetic field are similar to those in figure 34.

In figures 35 and 36, the interelement spacing has been increased to  $3 \lambda/4$ , and the number of elements  $2N$  has been decreased from 12 to 8 such that the width of the array is about the same. For this case, the unconstrained array satisfies (77) and the constraint has no effect. Thus, only one solu-

tion for the current is shown in figure 35. For the uniform array, the normalized error  $\epsilon_n = 8.87 \times 10^{-2}$ ; and for the synthesized array,  $\epsilon_n = 1.57 \times 10^{-2}$ . As expected, the errors have increased as the number of elements has been decreased from 12 to 8. The center cut of the electric field is shown in figure 36, and the field of the synthesized array decreases even faster than that of the uniform array outside the test volume. This is because the source norm is smaller for the synthesized array.

In figures 37 and 38, the interelement spacing  $d$  has been increased to  $\lambda$ , and the number of elements  $2N$  has been decreased to 6. In this case, the unconstrained solution again satisfies (77), and the constraint has no effect. The solution for the current is shown in figure 37. For the uniform array, the normalized error  $\epsilon_n = 0.278$ ; and for the synthesized array,  $\epsilon_n = 0.110$ . Thus, the synthesis procedure reduces the error, but both errors are fairly large. The center cut of the electric field is shown in figure 38, and the quality of the field is poor. Larger values of  $d$  have been found to yield even larger errors in the fields.

Part of the reason that the field quality is poor for  $d = \lambda$  in figure 38 is that the test volume is located close to the array ( $z_0 = 4\lambda$ ). In figures 39 and 40, the test volume has been moved farther from the array ( $z_0 = 8\lambda$ ). In this case, the constraint has a small effect as indicated by the two current solutions in figure 39. For the uniform array, the normalized error  $\epsilon_n = 8.81 \times 10^{-2}$ ; for the constrained array,  $\epsilon_n = 9.22 \times 10^{-3}$ ; and for the unconstrained array,  $\epsilon_n = 5.85 \times 10^{-3}$ . Thus the errors have been decreased significantly by moving the test volume farther from the array. The center cut of the electric field is shown in figure 40.

In figures 41 - 43, we consider a smaller test volume located closer to the array ( $A = B = z_0 = 2\lambda$ ). The solutions for the currents with and without a constraint are shown in figure 41. For the uniform array, the normalized error  $\epsilon_n = 1.00 \times 10^{-1}$ ; for the constrained array,  $\epsilon_n = 1.57 \times 10^{-2}$ ; and for the unconstrained array,  $\epsilon_n = 9.10 \times 10^{-3}$ . The corresponding uniqueness function  $F_y$  is shown over half the perimeter in figure 42. The electric field

on a center cut is shown in figure 43, and, as in previous cases, the constrained synthesis field has a more rapid decay than the unconstrained synthesis field outside the test volume.

Other calculations have produced similar results. The uniform array always has the largest error, and the unconstrained synthesized array has the smallest error. The constrained synthesized array is a good compromise because it has a small error and a rapid field decay outside the test volume. The computer code for the array synthesis is very fast, and it is easy to do further parameter studies.

One area which deserves further study is the relationship between the normalized error in the surface fields defined by (92) and the error in the fields throughout the test volume. By uniqueness, the volume error vanishes when the surface error in  $\underline{F}$  vanishes. Also, the numerical results indicate that the normalized error in the fields throughout the test volume are small when the errors in  $\underline{F}$  on the surface are small. However, it would be useful to have a more definite relationship since our synthesis technique only minimizes the error in  $\underline{F}$ .

## 7. Conclusions and recommendations

In the wide frequency range of interest (approximately 30 MHz to several GHz) for electromagnetic susceptibility testing, there is a gap between the "low frequency" and "high frequency" methods of producing a plane wave test field. For example, the TEM cell is useful below about 50 MHz, and the compact range is useful above about 1 GHz. From the previous work reviewed in section 2 and the theoretical results of sections 3 - 6, it is clear that a near-field phased array is a promising means of producing a plane wave in the frequency range of interest. The reverberation chamber [38] can be used over a similar frequency range, but it has not been discussed in this report because it does not produce a plane wave.

As shown in section 2, there is no fundamental limitation on the quality of the plane wave which can be generated by near-field sources. Many different source distributions can produce the same plane wave field in a

given test volume, but they will produce different fields outside the test volume. Thus, there is no unique solution to the array synthesis problem in designing a near-field array, and many array geometries should be considered. A number of practical questions involving bandwidth [39], array scanning capability, and array elements and geometry must be addressed before near-field arrays can be made useful for susceptibility testing.

The truncation effects at the edges of near-field arrays are analogous to the errors due to finite scan area in near-field scanning [20]. As shown in sections 4 and 5, the main effect is a ripple which results from interference between the edge diffracted fields and the desired plane wave. As shown in section 5, the ripple can be reduced by tapering the amplitude of the elements at the edges of the array. The main practical difficulty at high frequencies is that a large number of elements is required to produce a plane wave over an electrically large test volume.

In order to avoid trial-and-error procedures in determining the element weightings, a very general near-field synthesis method based on a new uniqueness theorem was developed in section 6. The method minimizes the mean squared error between the desired field and the actual field over the test volume, and it provides a direct numerical solution for the amplitude and phase of the element weightings. In addition, a constraint can be placed on the source norm in order to prevent large fields outside the test volume. This is important in minimizing wasted power and reflections from nearby objects. The computer code is very efficient, and parameter studies are easily performed.

In order to better understand the capabilities and limitations of near-field phased arrays, the following theoretical studies are recommended. The general near-field synthesis technique should be applied to realistic three-dimensional geometries involving realistic array elements (such as dipoles, loops, or aperture antennas). The case where the test volume is located in the near field of the individual elements should be included in order to understand low-frequency effects where the test volume is less than a wavelength from the array. Bandwidth limitations involving both the array geometry and array elements should be studied. Special wideband antennas

might be considered. A related study could examine the feasibility of transmitting narrow pulses for time-domain testing. The directional scanning limitations imposed by the array geometry and the array elements should be studied. Nonuniform element spacings [30] should be considered for reducing the number of array elements.

It is premature to design and build a large near-field array at this point, but valuable experience could be gained by building and testing one or two small arrays. Also, some of the potential difficulties, such as mutual coupling between array elements and reflections from surrounding objects, could be studied experimentally just as well as theoretically. Planar arrays appear to be the simplest to start with. The large frequency range of interest opens up numerous possibilities for array elements. Dipoles or loops could be used at VHF, and aperture antennas such as horns or open-ended waveguides, could be used at microwave frequencies. Special wideband antennas should also be considered. The element weightings would be determined from the array synthesis theory. An important part of the design would be the means of controlling the amplitude and phase of the element weightings. If possible, both amplitude and phase of the electric and magnetic fields should be measured throughout the test volume and compared with theoretical predictions. Some measurements should be made as a function of frequency and scan angle in order to evaluate bandwidth and scan limitations.

## 8. Acknowledgments

The author is grateful to Dr. M. T. Ma for technical discussions during the course of this work. Many thanks also go to C. K. S. Miller and H. E. Taggart for their continuous interest and support.

## 9. References

- [1] Olver, A. D.; Saleeb, A. A. Lens-type compact antenna range. *Electronics letters*, 15: 409-410; 1979.
- [2] Johnson, R. C.; Ecker, H. A.; Moore, R. A. Compact range techniques and measurements. *IEEE Trans. Ant. Propagat.*, AP-17: 568-575; 1969.

- [3] Excell, P. S.; Gunes, Z. F. The compact range principle applied to electromagnetic susceptibility testing. IERE Conf. Proc. Electro-magnetic Compatibility: 317-322; 1982.
- [4] Martsafey, V. V. Measurements of electrodynamic antenna parameters by the method of synthesized apertures. Radio Engr. Electron. Phys., 13: 1869-1873; 1968.
- [5] Bennett, J. C.; Schoessow, E. P. Antenna near-field/far-field transformation using a plane-wave-synthesis technique. IEE Proc., 125: 179-184; 1978.
- [6] Ludwig, A. C.; Larsen, F. H. Spherical near-field measurements from a compact-range viewpoint. Technical University of Denmark Report R213; 1979.
- [7] Bennett, J. C.; Muntanga, N. E. Antenna near-field/far-field transformation with reduced data acquisition and processing requirements. IEE Proc., 129(H): 229-231; 1982.
- [8] Schoessow, E. P. Plane wave synthesis: a new approach to the problems of antenna near-field/far-field transformation. University of Sheffield, Ph. D. thesis; 1980.
- [9] Lynggaard, S. K. Plane wave synthesis for antenna measurements. Technical University of Denmark (in Danish), M. S. thesis; 1982.
- [10] Harrington, R. F. Time-harmonic electromagnetic fields. New York: McGraw-Hill; 1961.
- [11] Waterman, P. C. Matrix formulation of electromagnetic scattering. Proc. IEEE, 53: 805-812; 1965.
- [12] Bowman, J. J.; Senior, T. B. A ; Uslenghi P. L. E., ed. Electromagnetic and acoustic scattering by simple shapes. Amsterdam: North-Holland Publishing Co.; 1969.
- [13] Mittra, R., ed. Computer techniques for electromagnetics. Oxford: Pergamon Press; 1973.
- [14] Senior, T. B. A. Approximate boundary conditions. IEEE Trans. Ant. Propagat., AP-29: 826-829; 1981.
- [15] Jordan, E. C.; Balmain, K. G. Electromagnetic waves and radiating systems. Englewood Cliffs: Prentice Hall; 1968.
- [16] Wood, P. J. The prediction of antenna characteristics from spherical near-field measurements, part 1, theory. Marconi Review, XL: 42-68; 1977.
- [17] Andreason, M. G. Scattering from cylinders with arbitrary surface impedance. Proc. IEEE, 53: 812-817; 1965.

- [18] Turchin, V. I.; Tseytlin, N. M. Antenna testing based on near-field measurements. *Radio Engr. Electron. Phys.*, 24: 1-26; 1979.
- [19] Appel-Hansen, J. Antenna measurements using near-field scanning techniques. Technical University of Denmark Report NB 129; 1980.
- [20] Yaghjian, A. D. Upper-bound errors in far-field antenna parameters determined from planar near-field measurements, part 1: analysis. *Nat. Bur. Stand. (U.S.) Tech. Note* 667; 1975.
- [21] Appel-Hansen, J. Near-field scanning and intermediate distance techniques for antenna measurements. Technical University of Denmark Report NB 134; 1981.
- [22] James, G. L. Geometrical theory of diffraction for electromagnetic waves. Stevenage: Peter Peregrinus; 1976.
- [23] Abramowitz, M.; Stegun, I. A., ed. Handbook of mathematical functions. *Nat. Bur. Stand. (U.S.) Handb.*; 1964.
- [24] Keller, J. B. Diffraction by an aperture. *J. Appl. Phys.* 28: 426-444; 1957.
- [25] Keller, J. B.; Lewis, R. M.; Seckler, B. D. Diffraction by an aperture, II. *J. Appl. Phys.* 28: 570-579; 1957.
- [26] Kraus, J. D. Antennas. New York: McGraw-Hill; 1950.
- [27] Yaghjian, A. D. Approximate formulas for the far fields and gain of open-ended rectangular waveguide. *Nat. Bur. Stand. (U.S.) NBSIR* 83-1689; 1983.
- [28] Crawford, M. L. Calibration of broadbeam antennas using planar near-field measurements. Conference on Precision Electromagnetic Measurements: 53-56; 1976.
- [29] Collin, R. E.; Zucker, F. J., ed. Antenna theory part 1. New York: McGraw-Hill; 1969. Ch. 7.
- [30] Ma, M. T. Theory and application of antenna arrays. New York: John Wiley & Sons; 1974.
- [31] Mautz, J. R.; Harrington, R. F. Computational methods for antenna pattern synthesis. *IEEE Trans. Ant. Propagat.* AP-23: 507-512; 1975.
- [32] Müller C. Foundations of the mathematical theory of electromagnetic waves. Berlin: Springer-Verlag; 1969.
- [33] Mautz, J. R.; Harrington, R. F. H-field, E-field, and combined-field solutions for conducting bodies of revolution. *AEU*, 32: 157-164; 1978.

- [34] Kanda, M. An electric and magnetic field sensor for simultaneous electromagnetic near-field measurements--theory. Nat. Bur. Stand. (U.S.) Tech. Note 1062; 1983.
- [35] Boisvert, R.; Howe, S.; Kahauer, D.; Knapp-Cordes, J.; Knapp-Cordes, M. Guide to available mathematical software. Center for Applied Mathematics, Nat. Bur. Stand. (U.S.); 1981.
- [36] Hamming, R. W. Numerical methods for scientists and engineers. New York: McGraw-Hill; 1973.
- [37] Dongarra, J. J.; Mohler, C. B.; Bunch, J. R.; Stewart, G. W. LINPACK user's guide. Philadelphia: SIAM, 1979.
- [38] Crawford, M. L. Evaluation of a reverberation chamber for performing EM radiated fields susceptibility measurements. Nat. Bur. Stand. (U.S.) NBSIR 81-1638; 1981.
- [39] Schoessow, E. P.; Bennett, J. C. The plane wave synthesis technique for antenna near-field/far-field transformation: further development. IEEE Conf. Pub. 195: 269-273; 1981.

## Appendix A

### Asymptotic evaluation of two-dimensional fields

The first step in the evaluation of the integral in (22) is to replace the Hankel function by its asymptotic form for large argument [10]:

$$H_0^{(2)}(x) \sim \sqrt{\frac{2j}{\pi x}} e^{-jx} \quad (A1)$$

Substituting (21) and (A1) into (22), the integral can be cast in the following form:

$$\underline{A} = \int_{-\infty}^0 \underline{f}(x') e^{jkg(x')} dx' ,$$

where

$$\underline{f}(x') = \frac{\hat{z} \times H_0}{\sqrt{2\pi jk} [(x - x')^2 + z^2]^{1/2}} , \quad (A2)$$

and

$$g(x') = - [x' \sin \theta_i + \sqrt{(x - x')^2 + z^2}] .$$

In order to obtain the stationary phase contribution to (A2), we need the first and second derivatives of  $g(x')$  with respect to  $x'$ :

$$g'(x') = - \sin \theta_i + \frac{x - x'}{\sqrt{(x - x')^2 + z^2}}$$

and

$$g''(x') = \frac{-1}{\sqrt{(x - x')^2 + z^2}} + \frac{(x - x')^2}{[(x - x')^2 + z^2]^{3/2}} . \quad (A3)$$

The stationary phase point  $x'_S$  occurs for  $g'(x'_S) = 0$ . This equation is easily solved to yield

$$x'_S = x - z \tan \theta_i \quad (\text{A4})$$

Since  $x'_S$  must be negative, a stationary phase point exists only for  $z \tan \theta_i > x$ . This is the region to the left of the dashed line in figure 8. At the stationary point ( $x' = x'_S$ ),  $\underline{f}$ ,  $g$ , and  $g''$  have the following values:

$$\begin{aligned} g(x'_S) &= - (x \sin \theta_i + z \cos \theta_i) , \\ g''(x'_S) &= - \cos^3 \theta_i / z , \quad \text{and} \end{aligned} \quad (\text{A5})$$

$$\underline{f}(x'_S) = \hat{z} \times \underline{H}_0 \sqrt{\frac{\cos \theta_i}{2\pi j k z}} .$$

The stationary phase evaluation of integrals of the form of (A2) yields the following general form [22]:

$$\underline{A}_S \sim \sqrt{\frac{2\pi}{k |g''(x'_S)|}} \underline{f}(x'_S) \exp\{j[kg(x'_S) + \frac{\pi}{4} \text{sgn}[g''(x'_S)]]\} , \quad (\text{A6})$$

where  $\text{sgn}$  is the sign of the argument. Since we are interested only in positive  $z$  and values of  $|\theta_i|$  less than  $\pi/2$ ,  $g''$  in (A5) is negative. Substituting (A5) into (A6), we obtain the final result for  $\underline{A}_S$ :

$$\underline{A}_S \sim \hat{z} \times \underline{H}_0 \frac{e^{-jk(x \sin \theta_i + z \cos \theta_i)}}{jk \cos \theta_i} U(z \tan \theta_i - x) . \quad (\text{A7})$$

The general form for the end point (or edge diffraction) term is given by [22]:

$$\underline{A}_e \sim \underline{f}(0) e^{jkg(0)} \sqrt{\frac{2}{k |g''(0)|}} F_{\pm}(\nu) e^{\mp j\nu^2 \text{sgn}(g'(0))} ,$$

$$g''(0) \begin{matrix} > \\ < \end{matrix} 0, \quad \text{where} \quad (\text{A8})$$

$$v = \sqrt{\frac{k}{2|g''(0)|}} |g'(0)|.$$

The Fresnel integral  $F_{\pm}$  is defined as [22]:

$$F_{\pm}(v) = \int_v^{\infty} \exp(\pm jt^2) dt. \quad (\text{A9})$$

By substituting (A2) and (A3) into (A8), we obtain the final value for  $\underline{A}_e$ :

$$\underline{A}_e \sim \hat{z} \times \underline{H}_0 \frac{e^{-j(k\rho - \frac{\pi}{4})}}{jk \cos \theta_e \sqrt{\pi}} F_-(v) e^{jv^2} \text{sgn}(\theta - \theta_{ei}), \quad (\text{A10})$$

where

$$v = \frac{\sqrt{k\rho/2}}{\cos \theta_e} |\sin \theta_e - \sin \theta_i|,$$

$$\sin \theta_e = x/\rho, \quad \text{and} \quad \rho = \sqrt{x^2 + z^2}.$$

The electric and magnetic fields are given by the curl operations indicated in (30). In order to evaluate the curl, we use the following vector identity [10]:

$$\nabla \times (\underline{a}\phi) = \nabla\phi \times \underline{a} + \phi\nabla \times \underline{a}. \quad (\text{A11})$$

Using (A7) and (A11), the curl of  $\underline{A}_s$  is found to yield the expected plane wave expression  $\underline{H}_p$  in the illuminated region:

$$\begin{aligned} \underline{H}_s &= \nabla \times \underline{A}_s \\ &\sim \frac{U(\theta_i - \theta_e)}{jk \cos \theta_i} \nabla [e^{-jk(x \sin \theta_i + z \cos \theta_i)}] \times (\hat{z} \times \underline{H}_0) \\ &\sim \underline{H}_p U(\theta_i - \theta_e), \end{aligned} \quad (\text{A12})$$

where  $\underline{H}_p$  is given by (21). The stationary phase value of the electric field is given by an additional curl operation:

$$\begin{aligned} \underline{E}_s &= \frac{1}{j\omega\epsilon} \nabla \times \underline{H}_s \\ &\sim \frac{U(\theta_i - \theta_e)}{j\omega\epsilon} \nabla \left[ e^{-jk(x \sin \theta_i + z \cos \theta_i)} \right] \times \underline{H}_0 \\ &\sim \frac{U(\theta_i - \theta_e)}{j\omega\epsilon} \left[ -j k e^{-jk(x \sin \theta_i + z \cos \theta_i)} \right] \hat{k}_i \times \underline{H}_0 \quad (A13) \\ &\sim -\eta \hat{k}_i \times \underline{H}_p U(\theta_i - \theta_e), \end{aligned}$$

where  $\hat{k}_i$  is given by (21). Strictly speaking, both (A12) and (A13) should contain an extra term from the differentiation of the unit step  $U(\theta_i - \theta_e)$ , but this term is omitted here because it is later canceled by a term in  $\underline{A}_e$ .

The curl of the edge diffraction term is somewhat more involved:

$$\begin{aligned} \underline{H}_e &= \nabla \times \underline{A}_e \\ &\sim \frac{F_-(\nu) e^{j(\nu^2 + \pi/4)} \operatorname{sgn}(\theta_e - \theta_i)}{jk \cos \theta_e} \cdot \nabla \times \left[ \hat{z} \times \underline{H}_0 e^{-jk\rho} \right] \quad (A14) \\ &\sim \left[ \underline{H}_0 \cos \theta_e - \hat{z} (\underline{H}_0 \cdot \hat{\rho}) \right] e^{-jk\rho} F_-(\nu) \frac{e^{j(\nu^2 + \pi/4)}}{\cos \theta_e \sqrt{\pi}} \operatorname{sgn}(\theta_e - \theta_i), \end{aligned}$$

where

$$\hat{\rho} = \hat{x} \sin \theta_e + \hat{z} \cos \theta_e.$$

In (A14) and in all other equations in Appendices A and B, only the leading term in powers of  $k$  is retained. The electric field edge diffraction term is obtained from the curl of  $\underline{H}_e$ :

$$\underline{E}_e = \frac{1}{j\omega\epsilon} \nabla \times \underline{H}_e \sim \eta [\underline{H}_0 \times \hat{\rho} \cos \theta_e - \hat{y} \sin \theta_e (\underline{H}_0 \cdot \hat{\rho})] \cdot \frac{e^{-jk\rho} e^{j(\nu^2 + \pi/4)} F(\nu) \operatorname{sgn}(\theta_e - \theta_i)}{\cos \theta_e \sqrt{\pi}} . \quad (\text{A15})$$

The total electric and magnetic fields can now be written:

$$\underline{E} = \underline{E}_s + \underline{E}_e \quad \text{and} \quad \underline{H} = \underline{H}_s + \underline{H}_e . \quad (\text{A16})$$

## Appendix B

### Asymptotic evaluation of three-dimensional fields

For the rectangular surface shown in figure 18, a stationary phase point exists inside the tube:

$$0 < y < b \quad \text{and} \tag{B1}$$

$$z \tan \theta_i < x < a + z \tan \theta_i .$$

The stationary phase contribution from this point is the desired plane wave field. Outside the tube, no stationary phase points exist, and only edge-diffracted fields are present.

Each of the four edges in figure 18 generates an edge-diffracted field of the form given by (46). For the rectangular geometry of figure 18, the specific form for  $\underline{f}$  and  $g$  as given by (42) are:

$$\underline{f} = \frac{\hat{z} \times H_0}{2\pi R} \quad \text{and} \quad g = - (x' \sin \theta_i + R) , \tag{B2}$$

where

$$R = |\underline{r} - \underline{r}'| = \sqrt{(x - x')^2 + (y - y')^2 + z^2} .$$

For each of the four edges,  $u_1$ ,  $u_2$ , and  $\alpha$  as defined in figure 17 are different functions of  $x'$ ,  $y'$ ,  $a$ , and  $b$ . For each edge we will now define and derive all of the required quantities in the edge diffraction term (46).

For edge number 1, we have

$$u_1 = -y' , \quad u_2 = x' , \quad \text{and} \quad \alpha = 0. \tag{B3}$$

The required derivatives of  $g$  are

$$g_{u_1} = \frac{y - y'}{R}, \quad g_{u_2} = \frac{x - x'}{R} - \sin \theta_i, \quad (B4)$$

$$g_{u_1 u_1} = -\frac{(x - x')^2 + z^2}{R^3}, \quad \text{and} \quad g_{u_2 u_2} = -\frac{(y^2 + z^2)}{R^3}.$$

The stationary edge point determined from  $g_{u_2} = 0$  is:

$$u_{2e} = x - \sqrt{y^2 + z^2} \tan \theta_i, \quad (B5)$$

where

$$0 < u_{2e} < a.$$

If the stationary point  $u_{2e}$  lies outside the interval from 0 to  $a$ , then the contribution from edge 1 is zero. Substituting (B2) - (B5) into (46), the contribution from edge 1 is:

$$\underline{A}_{e1} = -\hat{z} \times \underline{H}_0 \frac{\text{sgn}(y) \sqrt{y^2 + z^2} e^{jv_1^2} F_-(v_1) e^{jkg_1}}{k \cos \theta_i \sqrt{j\pi(y^2 \sin^2 \theta_i + z^2)}}, \quad (B6)$$

where

$$v_1 = \sqrt{\frac{k(y^2 + z^2)^{1/2} \cos \theta_i}{2(y^2 \sin^2 \theta_i + z^2)}} |y|$$

and

$$g_1 = -x \sin \theta_i - \sqrt{y^2 + z^2} \cos \theta_i.$$

For edge number 2, we have

$$u_1 = x', \quad u_2 = y', \quad \text{and} \quad \alpha = a \quad (B7)$$

The required derivatives of  $g$  are

$$\begin{aligned}
 g_{u_1} &= \frac{x - x'}{R} - \sin \theta_i, & g_{u_2} &= \frac{y - y'}{R}, \\
 g_{u_1 u_1} &= \frac{-[(y - y')^2 + z^2]}{R}, & \text{and} & \\
 g_{u_2 u_2} &= \frac{-[(x - x')^2 + z^2]}{R}.
 \end{aligned} \tag{B8}$$

The stationary point determined from  $g_{u_2} = 0$  is:

$$u_{2e} = y, \quad \text{where} \quad 0 < u_{2e} < b. \tag{B9}$$

If the stationary point  $u_{2e}$  lies outside the interval from 0 to  $b$ , then the contribution from edge 2 is zero. Substituting (B2) and (B7) - (B9) into (46), the contribution from edge 2 is:

$$\underline{A}_{e2} = \hat{z} \times \underline{H}_0 \frac{\text{sgn}(g_{u_1}) \sqrt{(x - a)^2 + z^2}}{kz \sqrt{j\pi}} e^{jv_2^2} F_-(v_2) e^{jkg_2},$$

where

$$g_{u_1} = \frac{x - a}{\sqrt{(x - a)^2 + z^2}} - \sin \theta_i, \tag{B10}$$

$$v_2 = \sqrt{\frac{k[(x - a)^2 + z^2]^{3/2}}{2z^2}} |g_{u_1}|,$$

and

$$g_2 = -a \sin \theta_i - \sqrt{(x - a)^2 + z^2}.$$

For edge number 3, we have

$$u_1 = y', \quad u_2 = -x', \quad \text{and} \quad \alpha = b. \tag{B11}$$

The required derivatives of  $g$  are

$$g_{u_1} = \frac{y - y'}{R}, \quad g_{u_2} = \sin \theta_i + \frac{x - x'}{R},$$

$$g_{u_1 u_1} = \frac{-[(x - x')^2 + z^2]}{R^3}, \quad \text{and} \quad (B12)$$

$$g_{u_2 u_2} = \frac{-[(y - y')^2 + z^2]}{R^3}.$$

The stationary point determined from  $g_{u_2} = 0$  is:

$$u_{2e} = \sqrt{(y - b)^2 + z^2} \tan \theta_i - x, \quad (B13)$$

where

$$-a < u_{2e} < 0.$$

If the stationary point  $u_{2e}$  lies outside the interval from  $-a$  to  $0$ , then the contribution from edge 3 is zero. Substituting (B2) and (B11) - (B13) into (46), the contribution from edge 3 is:

$$\underline{A}_{e3} = \hat{z} \times \underline{H}_0 \frac{\text{sgn}(y - b) \sqrt{(y - b)^2 + z^2} e^{jv_3^2} F_-(v_3)}{k \cos \theta_i \sqrt{j\pi [(y - b)^2 \sin^2 \theta_i + z^2]}} e^{jkg_3},$$

where

$$v_3 = \sqrt{\frac{k \cos \theta_i [(y - b)^2 + z^2]}{2 [(y - b)^2 \sin^2 \theta_i + z^2]}} |y - b|, \quad (B14)$$

and

$$g_3 = -x \sin \theta_i - \sqrt{(y - b)^2 + z^2} \cos \theta_i.$$

For edge number 4, we have

$$u_1 = -x', \quad u_2 = -y', \quad \text{and} \quad \alpha = 0. \quad (\text{B15})$$

The required derivatives of  $g$  are

$$g_{u_1} = \sin \theta_i + \frac{x' - x}{R}, \quad g_{u_2} = \frac{y' - y}{R},$$

$$g_{u_1 u_1} = \frac{-[(y - y')^2 + z^2]}{R^3}, \quad \text{and} \quad (\text{B16})$$

$$g_{u_2 u_2} = \frac{-[(x - x')^2 + z^2]}{R^3}.$$

The stationary point determined from  $g_{u_2} = 0$  is

$$u_{2e} = y, \quad \text{where} \quad 0 < u_{2e} < b. \quad (\text{B17})$$

If the stationary point  $u_{2e}$  lies outside the interval from 0 to  $b$ , then the contribution from edge 4 is zero. Substituting (B2) and (B15) - (B17) into (47), the contribution from edge 4 is:

$$\underline{A}_{e4} = \hat{z} \times \underline{H}_0 \frac{\text{sgn}(g_{u_1}) \sqrt{x^2 + y^2}}{kz \sqrt{j\pi}} e^{jv_4^2} F_-(v_4) e^{jkg_4},$$

where

$$g_{u_1} = \sin \theta_i - \frac{x}{\sqrt{x^2 + y^2}},$$

$$v_4 = \frac{\sqrt{k(x^2 + y^2)^{3/2}}}{z\sqrt{2}} \left| \sin \theta_i - \frac{x}{\sqrt{x^2 + y^2}} \right|,$$

and

$$g_4 = -\sqrt{x^2 + z^2}.$$

The remaining task is to derive the electric and magnetic fields from the four edge-diffracted vector potential terms,  $\underline{A}_{e1}$ ,  $\underline{A}_{e2}$ ,  $\underline{A}_{e3}$ , and  $\underline{A}_{e4}$ . Each of the terms can be written in the following general form:

$$\underline{A}_e = \hat{z} \times \underline{H}_0 h(\underline{r}) e^{jkg(\underline{r})}, \quad (B19)$$

where  $h$  and  $g$  are different for each edge. Since we are dealing with high frequency fields, we include only the leading term in  $k$  for  $\underline{H}_e$ :

$$\begin{aligned} \underline{H}_e &= \nabla \times \underline{A}_e = \nabla \times [\hat{z} \times \underline{H}_0 h(\underline{r}) e^{jkg(\underline{r})}] = -(\hat{z} \times \underline{H}_0) \times \nabla [h(\underline{r}) e^{jkg(\underline{r})}] \\ &\sim -jkh(\underline{r}) e^{jkg(\underline{r})} (\hat{z} \times \underline{H}_0) \times \nabla g(\underline{r}). \end{aligned} \quad (B20)$$

For the electric field  $\underline{E}_e$ , we again retain only the leading term in  $k$ :

$$\begin{aligned} \underline{E}_e &= \frac{1}{j\omega\epsilon} \nabla \times \underline{H}_e \\ &= -\eta_0 \nabla \times [h(\underline{r}) e^{jkg(\underline{r})} (\hat{z} \times \underline{H}_0) \times \nabla g(\underline{r})] \\ &\sim \eta_0 jk h(\underline{r}) e^{jkg(\underline{r})} [(\hat{z} \times \underline{H}_0) \times \nabla g] \times \nabla g. \end{aligned} \quad (B21)$$

As a check on (B20) and (B21), it can be shown that  $\underline{E}_e$  and  $\underline{H}_e$  are consistent to the first order in  $k$ :

$$\nabla \times \underline{E}_e = -j\omega\mu \underline{H}_e. \quad (B22)$$

$\underline{E}_e$  and  $\underline{H}_e$  also satisfy the expected orthogonality relationship for high frequency fields:

$$\underline{E}_e \cdot \underline{H}_e = 0. \quad (B23)$$

In addition, the phase term  $g$  for each edge, satisfies the eiconal equation [22] as expected for high frequency fields:

$$\nabla g \cdot \nabla g = 1 . \quad (\text{B24})$$

Equations (B22) and (B23) are satisfied for any phase function  $g$ . To show that (B24) is satisfied, we need to take the gradient of  $g$  for each edge term. This requires no extra work because the gradients are required in (B20) and (B21) anyway. For the four edges the gradients are given by:

$$\begin{aligned} \nabla g_1 &= - \hat{x} \sin \theta_i - \frac{\cos \theta_i}{\sqrt{y^2 + z^2}} (y \hat{y} + z \hat{z}) , \\ \nabla g_2 &= - \frac{\hat{x} (x - a) + \hat{z} z}{\sqrt{(x - a)^2 + z^2}} , \end{aligned} \quad (\text{B25})$$

$$\nabla g_3 = - \hat{x} \sin \theta_i - \frac{\cos \theta_i}{\sqrt{(y - b)^2 + z^2}} [\hat{y} (y - b) + \hat{z} z] ,$$

and

$$\nabla g_4 = - \frac{\hat{x} x + \hat{z} z}{\sqrt{x^2 + z^2}} .$$

Both  $E_y$  and  $H_y$  polarizations are of interest. For  $E_y$  polarization,  $\underline{H}_0$  is given by

$$\underline{H}_0 = H_0 (- \hat{x} \cos \theta_i + \hat{z} \sin \theta_i) . \quad (\text{B26})$$

In this case,  $\hat{z} \times \underline{H}_0$  is given by

$$\hat{z} \times \underline{H}_0 = - H_0 \cos \theta_i \hat{y} . \quad (\text{B27})$$

Thus, the surface current is  $y$ -directed. For  $H_y$  polarization,  $\underline{H}_0$  is given by

$$\underline{H}_0 = \hat{y} H_0 . \quad (\text{B28})$$

In this case,  $\hat{z} \times \underline{H}_0$  is given by

$$\hat{z} \times \underline{H}_0 = -H_0 \hat{x} . \quad (\text{B29})$$

Thus the surface current is x-directed.

## Appendix C

### Fields of a Hertzian dipole

The fields of a Hertzian dipole in spherical coordinates are well known [10,26], but here we derive the Cartesian components of the fields. Consider an electric dipole of moment  $\underline{p}_{ij}$  located at  $(x'_i, y'_j)$  in the  $x$ - $y$  plane as indicated in figure 22. The magnetic vector potential  $\underline{A}_{ij}$  is given by

$$\underline{A}_{ij} = \frac{e^{-jkR}}{4\pi R} \underline{p}_{ij} ,$$

where

$$R = \sqrt{(x - x'_i)^2 + (y - y'_j)^2 + z^2} . \quad (C1)$$

The magnetic field  $\underline{H}_{ij}$  is derived from the curl of (C1):

$$\underline{H}_{ij} = \nabla \times \underline{A}_{ij} \sim \frac{1}{4\pi R} \nabla \times (\underline{p}_{ij} \cdot e^{-jkR}) \sim \frac{-1}{4\pi R} \underline{p}_{ij} \times \nabla (e^{-jkR}) . \quad (C2)$$

If  $\underline{p}_{ij}$  is written in terms of  $x$  and  $y$  components, then (C2) can be written:

$$\underline{H}_{ij} = \frac{jke^{-jkR}}{4\pi R^2} \{ \hat{x} z p_{ijy} - \hat{y} z p_{ijx} + \hat{z} [(y - y'_j)p_{ijx} - (x - x'_i) p_{ijy}] \} , \quad (C3)$$

where

$$\underline{p}_{ij} = \hat{x} p_{ijx} + \hat{y} p_{ijy} .$$

Only the leading terms in  $k$  have been retained in (C3).

The electric field  $\underline{E}_{ij}$  is determined from the curl of  $\underline{H}_{ij}$ :

$$\begin{aligned} \underline{E}_{ij} = \frac{1}{j\omega\epsilon} \nabla \times \underline{H}_{ij} \sim \eta \frac{jke^{-jkR}}{4\pi R^3} \{ & \hat{x} [-p_{ijx} [z^2 + (y - y'_j)^2] + p_{ijy} (x - x'_i) (y - y'_j)] \\ & + \hat{y} \{ p_{ix}^i (x - x'_i) (y - y'_j) - p_{ijy} [(x - x'_i)^2 + z^2] \} \} \end{aligned}$$

$$+ \hat{z} [p_{ijx} (x - x') + p_{ijy} z(y - y'_j)] \quad (C4)$$

Again, only the leading terms in  $k$  have been retained

## Appendix D

### Fields of a Huygens' source

The fields of a Huygens' source are the sum of the electric dipole fields and the magnetic dipole fields. The electric dipole fields can be obtained by making the following substitutions in (C3) and (C4):

$$p_{ijx} = - E_{ox} \Delta x' \Delta y' / \eta$$

(D1)

and

$$p_{ijy} = 0 .$$

This yields the following fields of the electric dipole source:

$$\underline{E}_{ije} = \frac{jk E_{ox} \Delta x' \Delta y'}{4\pi R^3} \{ \hat{x} [z^2 + (y - y'_{ij})^2] + \hat{y} (x'_{ij} - x) (y - y'_{ij}) - \hat{z} z (x - x'_{ij}) \} ,$$

(D2)

$$\underline{H}_{ije} = \frac{jk E_{ox} \Delta x' \Delta y' e^{-jkR}}{4\pi\eta R^2} [\hat{y} z - \hat{z} (y - y'_{ij})] .$$

The electric and magnetic fields of the magnetic dipole moment can be obtained from (C3) and (C4) by duality [10] and the following substitution:

$$p_{ijy} = - E_{ox} \Delta x' \Delta y' / \eta$$

(D3)

and

$$p_{ijx} = 0 .$$

By using duality on (D3), (C3), and (C4), we obtain the fields of the appropriate magnetic dipole moment as defined in (55):

$$\underline{E}_{ijm} = \frac{jk E_{ox} \Delta x' \Delta y' e^{-jkR}}{4\pi R^2} [\hat{x} z - \hat{z} (x - x'_{ij})] ,$$

$$\underline{H}_{ijm} = \frac{jk E_{ox} \Delta x' \Delta y'}{4\pi\eta R^3} \{ \hat{x} (x'_{ij} - x) (y - y'_{ij}) + \hat{y} [z^2 + (x - x'_{ij})^2] - \hat{z} z (y - y'_{ij}) \} . \quad (D4)$$

The total fields are the sum of the electric and magnetic dipole fields:

$$\underline{E}_{ij} = \underline{E}_{ije} + \underline{E}_{ijm} \quad \text{and} \quad \underline{H}_{ij} = \underline{H}_{ije} + \underline{H}_{ijm} . \quad (D5)$$

Substituting (D2) and (D4) into (D5), we obtain the final forms:

$$\underline{E}_{ij} = \frac{jk E_{ox} \Delta x' \Delta y' e^{-jkR}}{4\pi R^3} \{ \hat{x} [z^2 + (y - y'_{ij})^2 + z R] + \hat{y} (x'_{ij} - x) (y - y'_{ij}) + \hat{z} (x'_{ij} - x) (z + R) \} \quad (D6)$$

and

$$\underline{H}_{ij} = \frac{jk E_{ox} \Delta x' \Delta y' e^{-jkR}}{4\pi\eta R^3} \{ \hat{x} (x'_{ij} - x) (y - y'_{ij}) + \hat{y} [z^2 + (x - x'_{ij})^2 + z R] + \hat{z} (y_{ij} - y) (z + R) \} .$$

Note that  $\underline{E}_{ij}$  and  $\underline{H}_{ij}$  are zero in the back direction ( $x = x_{ij}$ ,  $y = y_{ij}$ , and  $z < 0$ ). As in Appendix C, only the leading terms in  $k$  are included.

## Appendix E

### A uniqueness example

To illustrate the utility of the function  $\underline{F}$  defined by (59), we consider a circular cylindrical example. Let the surface  $S$  in figure 29 be a circular cylinder of radius  $a$ , and assume that external sources produce only an  $E_z$  electric field which is independent of  $z$ . Thus, the problem is two-dimensional, and the magnetic field components,  $H_\rho$  and  $H_\phi$ , are obtained from Maxwell's curl equation:

$$\begin{aligned} H_\phi &= \frac{1}{j\omega\mu} \frac{\partial E_z}{\partial \rho} \\ H_\rho &= \frac{-1}{j\omega\mu\rho} \frac{\partial E_z}{\partial \phi} . \end{aligned} \tag{E1}$$

Standard cylindrical coordinates  $(\rho, \phi, z)$  are used.

Inside the source-free cylindrical region,  $E_z$  satisfies the scalar Helmholtz equation and can be written:

$$E_z = \sum_{n=-\infty}^{\infty} a_n J_n(k\rho) e^{jn\phi} , \tag{E2}$$

where  $J_n$  is the  $n^{\text{th}}$  order Bessel function [23] and  $a_n$  are the unknown coefficients. The vector  $\underline{F}$  as defined by (59) is

$$\underline{F} = \hat{z} F_z , \tag{E3}$$

where

$$F_z = (E_z + \eta_a H_\phi) \Big|_{\rho = a} .$$

For now, we take  $\eta_a$  to be some arbitrary real scalar, rather than the intrinsic impedance of the medium  $\eta$ . Substituting (E1) and (E2) into (E3), we obtain

$$(E_z + \eta_a H_\phi) \Big|_{\rho = a} = \sum_n a_n \left[ J_n(ka) + \frac{J'_n(ka) \eta_a}{j \eta} \right] e^{jn\phi}, \quad (E4)$$

where  $J'_n$  is the derivative of  $J_n$  with respect to the argument. To determine  $a_n$ , we multiply (E4) by  $e^{-jn\phi}$  and integrate from 0 to  $2\pi$ :

$$\int_0^{2\pi} (E_z + \eta_a H_\phi) \Big|_{\rho = a} e^{-jn\phi} d\phi = 2\pi \left[ J_n(ka) - j \frac{\eta_a}{\eta} J'_n(ka) \right] a_n. \quad (E5)$$

Both  $J_n$  and  $J'_n$  have an infinite number of zeros on the real axis, but never at the same argument [23]. Thus, the coefficient of  $a_n$  in (E5), which is complex, never vanishes and  $a_n$  can be written:

$$a_n = \frac{\int_0^{2\pi} (E_z + \eta_a H_\phi) \Big|_{\rho = a} e^{-jn\phi} d\phi}{2\pi \left[ J_n(ka) - j \frac{\eta_a}{\eta} J'_n(ka) \right]}. \quad (E6)$$

Thus  $a_n$  and the interior fields ( $E_z$ ,  $H_\rho$ ,  $H_\phi$ ) are uniquely determined by  $F$  on the boundary,  $\rho = a$ . If  $\eta_a$  is very small, then  $a_n$  is primarily determined by the electric field  $E_z$ . In the limit,  $\eta_a = 0$ ,  $a_n$  is given by:

$$a_n = \frac{\int_0^{2\pi} E_z \Big|_{\rho = a} e^{-jn\phi} d\phi}{2\pi J_n(ka)}, \quad (E7)$$

and  $a_n$  is determined by  $E_z$ . Unfortunately, this representation fails when  $J_n(ka) = 0$ . In such cases,  $a_n$  cannot be determined from  $E_z$ , and the fields are not uniquely determined.

If  $\eta_a$  is very large, then  $a_n$  is primarily determined by the magnetic field  $H_\phi$ . In the limit,  $\eta_a = \infty$ ,  $a_n$  is given by:

$$a_n = \frac{j \eta \int_0^{2\pi} H_\phi \Big|_{\rho = a} e^{-jn\phi} d\phi}{2\pi J'_n(ka)}. \quad (E8)$$

This representation fails when  $J'_n(ka) = 0$ . In such cases,  $a_n$  cannot be determined from  $H_\phi$ , and the fields are not uniquely determined.

For the case where  $\eta_a = \eta$ ,  $a_n$  is given by

$$a_n = \frac{\int_0^{2\pi} (E_z + \eta H_\phi) \Big|_{\rho = a} e^{-jn\phi} d\phi}{2\pi [J_n(ka) - j J_n'(ka)]} \quad (E9)$$

In this case,  $a_n$  is determined approximately equally by the electric and magnetic fields. Another advantage of the choice  $\eta_a = \eta$  is that the denominator is numerically well conditioned. Whenever  $J_n = 0$ ,  $J_n'$  is a maximum and vice versa. So the choice of  $\eta_a = \eta$  appears to be a good one.

## Appendix F

### Line source fields

A y-directed line source located in the  $z = 0$  plane at  $x = x'$ , produces the following y component of electric field [10]:

$$E_y = \frac{-k \eta I}{4} H_0^{(2)}(k\rho),$$

where

$$\rho = \sqrt{(x - x')^2 + z^2} \quad (F1)$$

and  $I$  is the line current. The  $E_{yj}$  term required in (86) is the sum of two terms with  $I$  set equal to unity:

$$E_{yj} = \frac{-k \eta}{4} [H_0^{(2)}(k\rho_j^+) + H_0^{(2)}(k\rho_j^-)],$$

where

$$\rho_j^+ = \sqrt{(x - x'_j)^2 + z^2} \quad (F2)$$

and

$$\rho_j^- = \sqrt{(x + x'_j)^2 + z^2}.$$

The magnetic field  $\underline{H}_j$  is obtained from the curl of the electric field:

$$\underline{H}_j = \frac{-1}{j\omega\mu} \nabla \times (\hat{y} E_{yj}) = \hat{x} H_{xj} + \hat{z} H_{zj},$$

where

$$H_{xj} = \frac{1}{j\omega\mu} \frac{\partial E_{yj}}{\partial z} \quad (F3)$$

and

$$H_{zj} = \frac{-1}{j\omega\mu} \frac{\partial E_{yj}}{\partial x}.$$

Substituting (F2) into (F3), we obtain:

$$H_{xj} = \frac{1}{4j} \left[ \frac{z}{\rho_j^+} H_1^{(2)}(k\rho_j^+) + \frac{z}{\rho_j^-} H_1^{(2)}(k\rho_j^-) \right],$$

(F4)

$$H_{zj} = \frac{1}{4j} \left[ \frac{x - x'_j}{\rho_j^+} H_1^{(2)}(k\rho_j^+) + \frac{x + x'_j}{\rho_j^-} H_1^{(2)}(k\rho_j^-) \right],$$

where  $H_1^{(2)}$  is the first-order Hankel function of the second kind. As with the zero-order Hankel function in (A1), when the argument is large, the asymptotic expansion can be used [10]:

$$H_1^{(2)}(x) \sim j \sqrt{\frac{2j}{\pi x}} e^{-jx}. \quad (F5)$$

The expression for  $T_{ij}$  is obtained by substituting (F3) into (84):

$$T_{ij} = [E_{yj} - \eta \hat{y} \cdot \hat{n} \times (\hat{x} H_{xj} + \hat{z} H_{zj})] \Big|_{\substack{x = x_i \\ z = z_i}}. \quad (F6)$$

Using vector identities, (F6) can be written:

$$T_{ij} = [E_{yj} - \eta(\hat{n} \cdot \hat{z} H_{xj} - \hat{n} \cdot \hat{x} H_{zj})] \Big|_{\substack{x = x_i \\ z = z_i}}. \quad (F7)$$

The values of the dot products in (F7) depend on which side of the test volume the point is located:

$$\begin{aligned} \text{side 1} & : \hat{n} \cdot \hat{z} = 1, & \hat{n} \cdot \hat{x} = 0, \\ \text{side 2} & : \hat{n} \cdot \hat{z} = 0, & \hat{n} \cdot \hat{x} = -1, \\ \text{side 3} & : \hat{n} \cdot \hat{z} = -1, & \hat{n} \cdot \hat{x} = 0, \\ \text{side 4} & : \hat{n} \cdot \hat{z} = 0, & \hat{n} \cdot \hat{x} = 1. \end{aligned} \quad (F8)$$

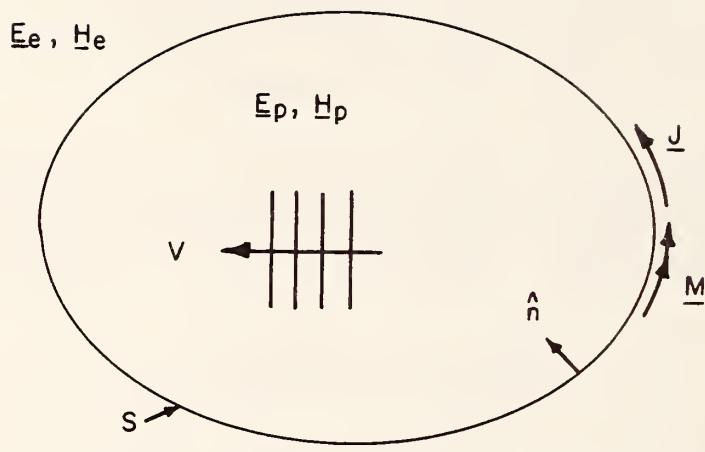


Figure 1. Electric and magnetic surface currents,  $\underline{J}$  and  $\underline{M}$ , on a surface  $S$ .

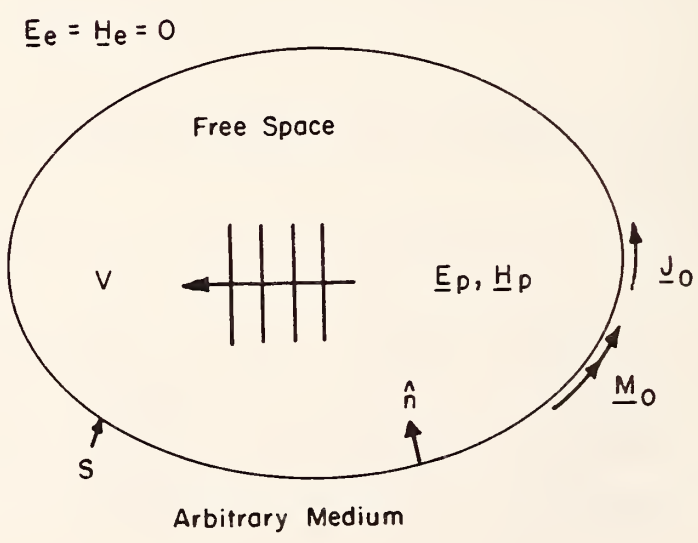


Figure 2. Electric and magnetic surface currents,  $\underline{J}_0$  and  $\underline{M}_0$ , which generate a plane wave inside  $S$  and a zero field outside  $S$ .

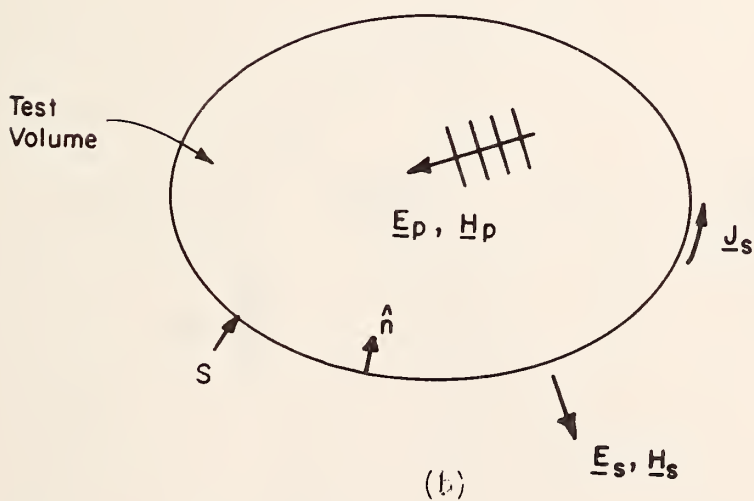
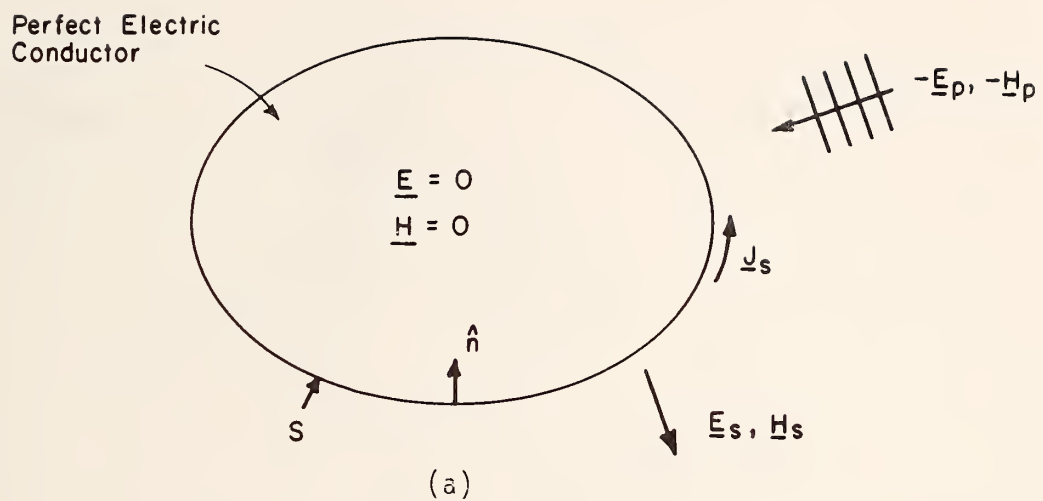


Figure 3. Electric surface current  $\underline{J}_s$  flowing on  $S$ . (a) Scattering problem for plane wave incidence. (b) Source problem for plane wave synthesis.

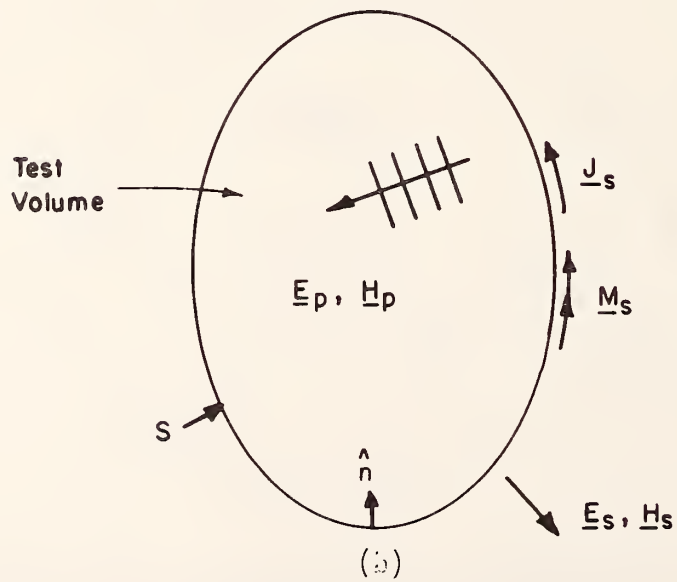
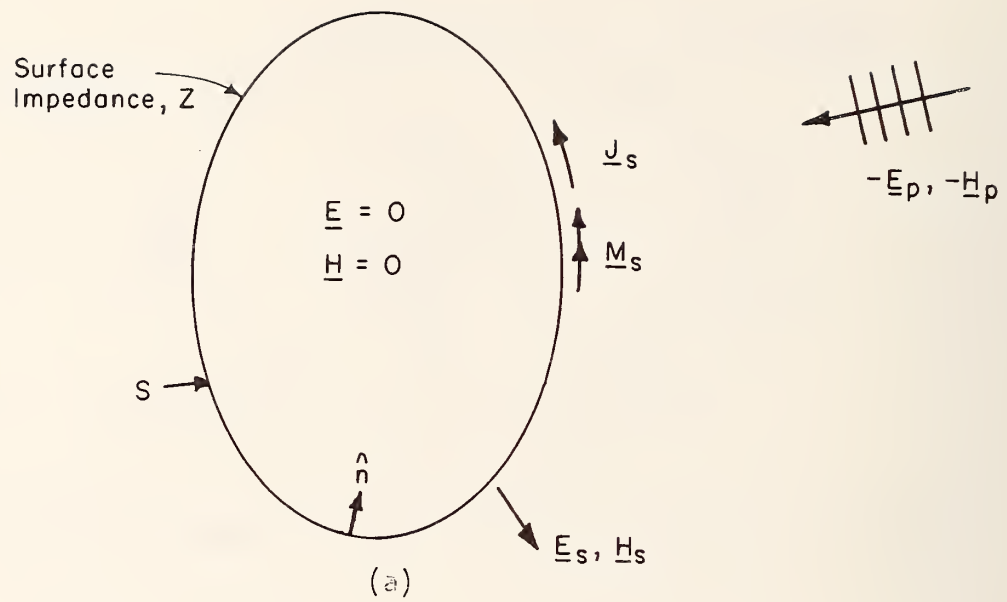


Figure 4. (a) Equivalent currents,  $\underline{J}_s$  and  $\underline{M}_s$ , excited on an impedance surface. (b) Source currents,  $\underline{J}_s$  and  $\underline{M}_s$ , for plane wave synthesis.

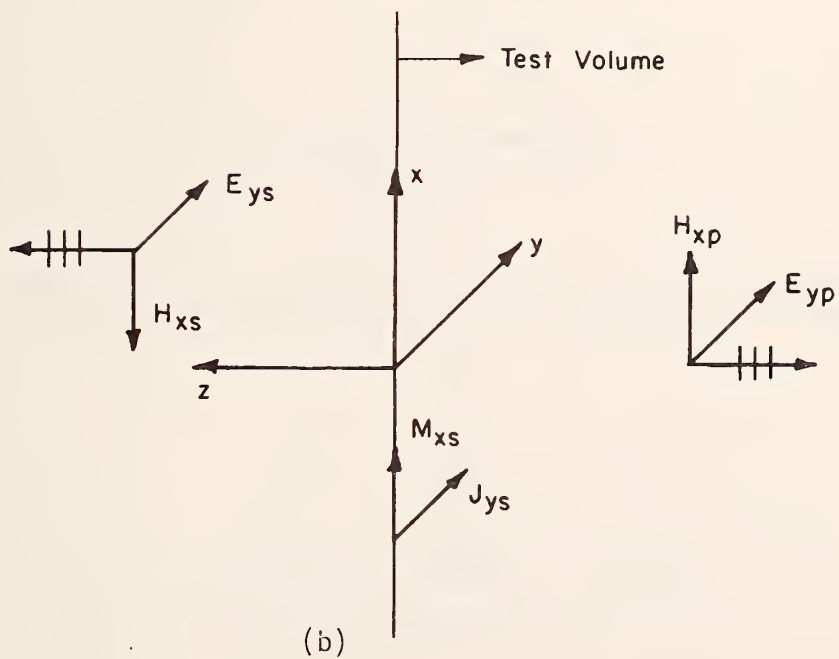
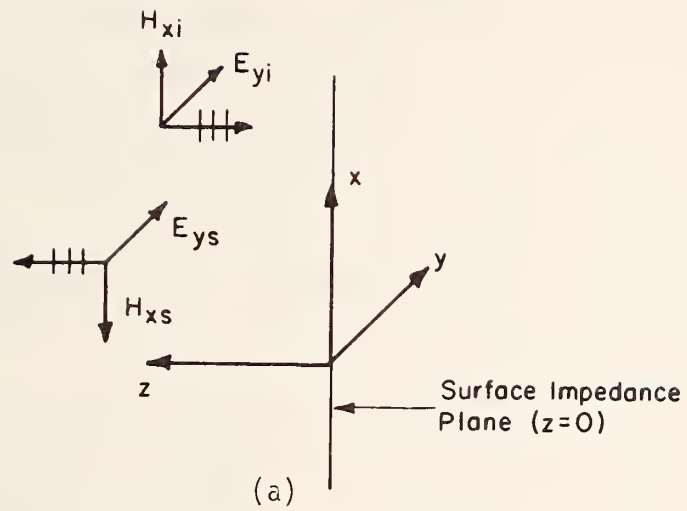


Figure 5. (a) Plane wave incident on a surface impedance plane. (b) Radiation by equivalent electric and magnetic sheet currents,  $J_{ys}$  and  $M_{xs}$ .

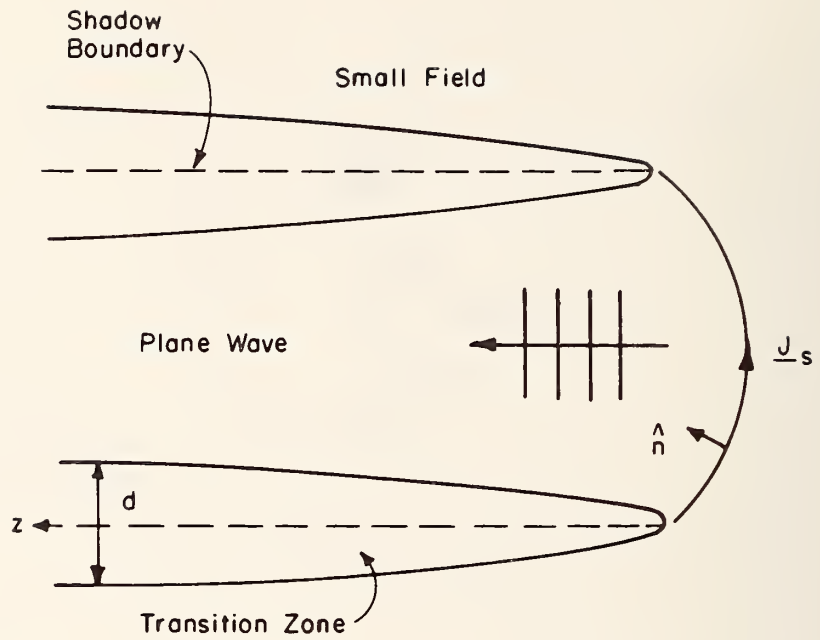


Figure 6. Near fields of the physical optics current,  $\underline{J}_s = 2 \hat{n} \times \underline{H}_p$ .

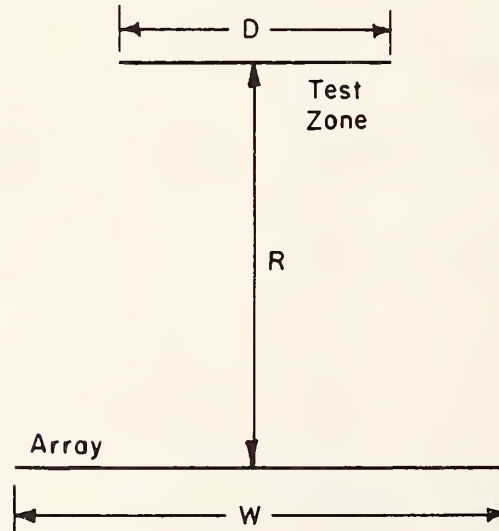


Figure 7. Planar array of width  $W$  with interelement spacing  $s$ . The test zone is of width  $D$  and is located at a distance  $R$ .

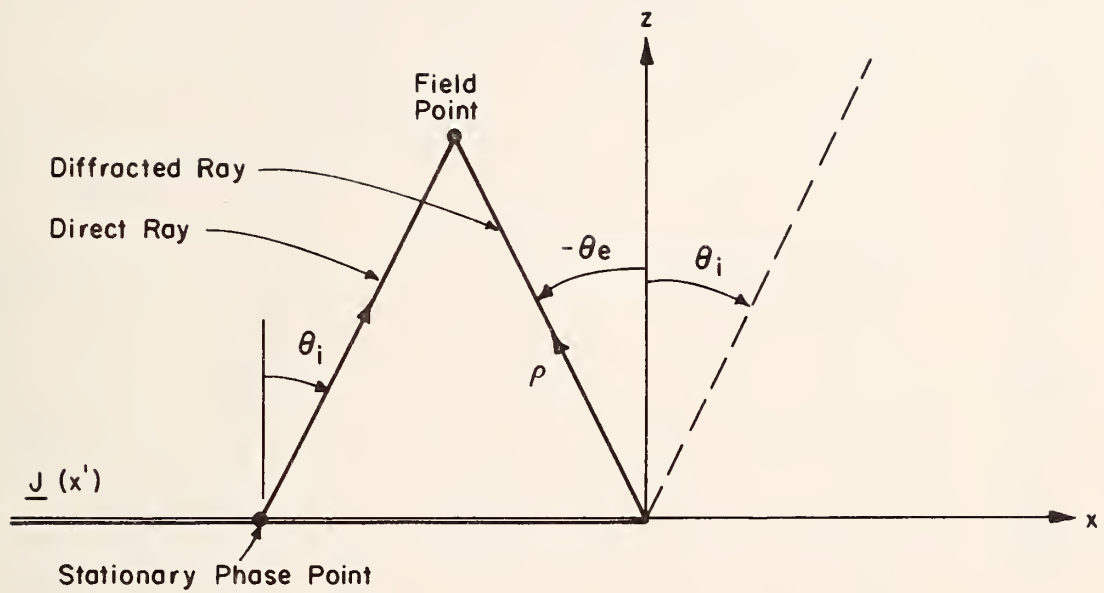


Figure 8. Physical optics current  $\underline{J}(x')$  on a semi-infinite plane. The total field can be described by a direct ray plus a diffracted ray.

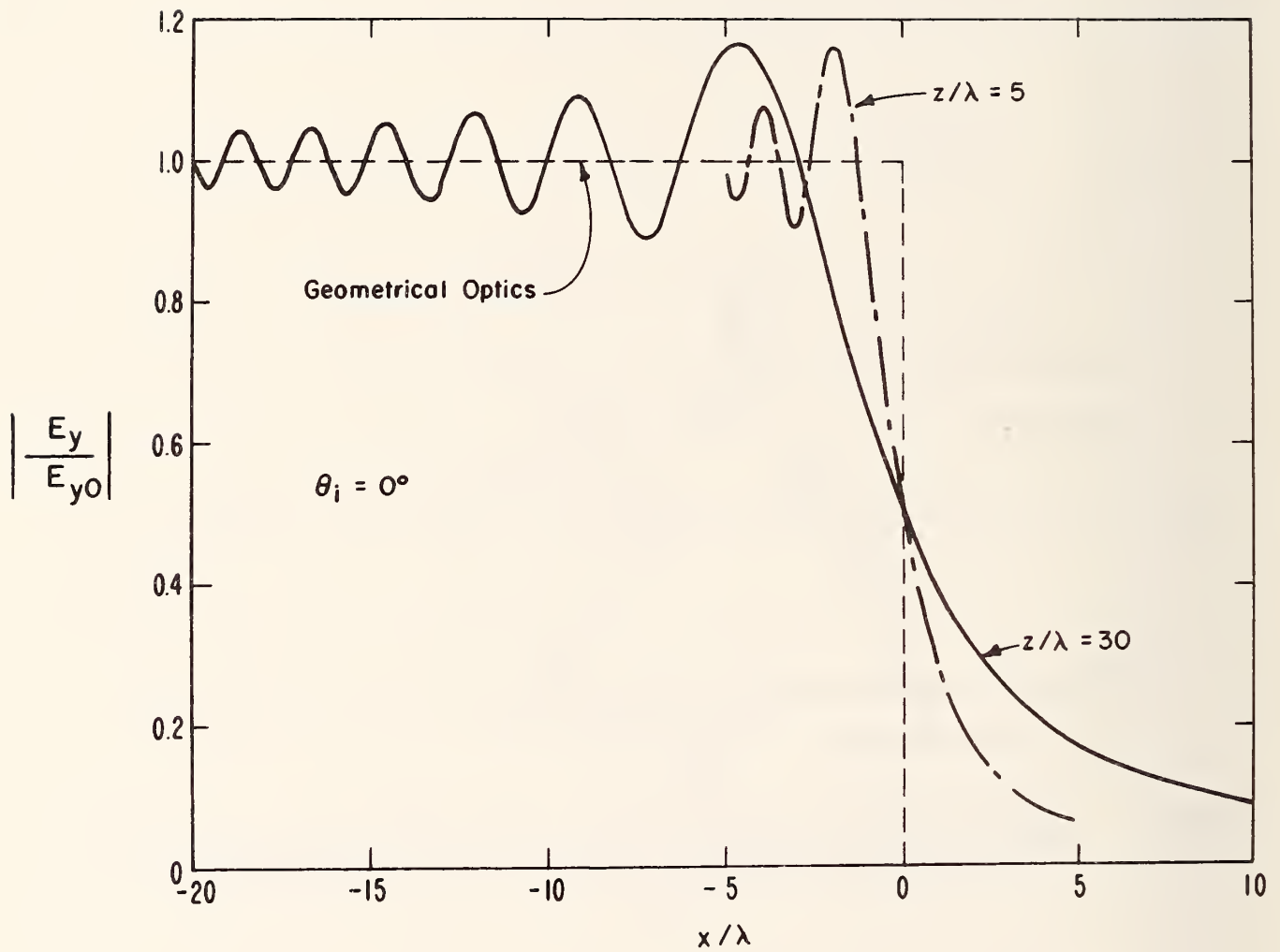


Figure 9. Magnitude of the normalized electric field of a semi-infinite current sheet ( $E_y$  polarization).

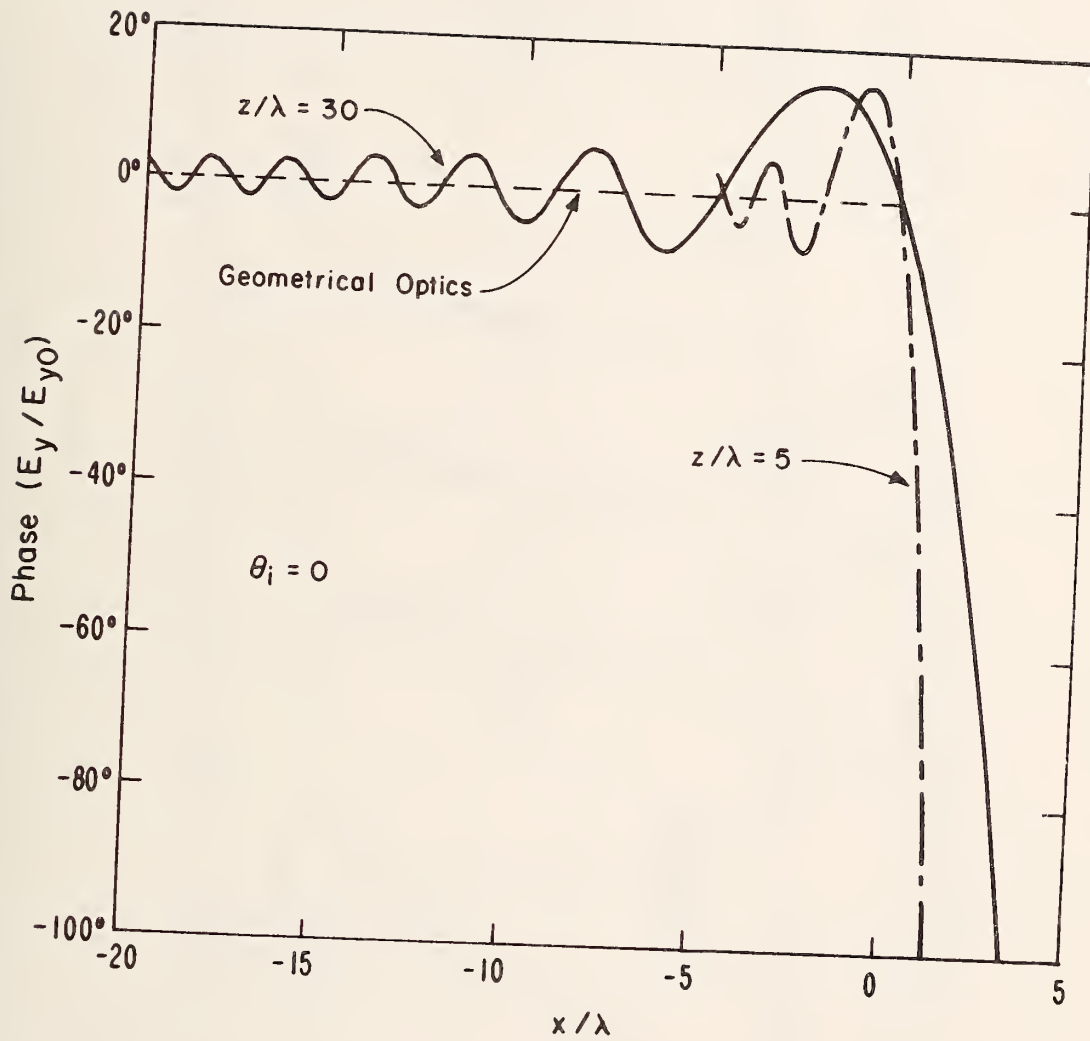


Figure 10. Phase of the normalized electric field of a semi-infinite current sheet ( $E_y$  polarization).

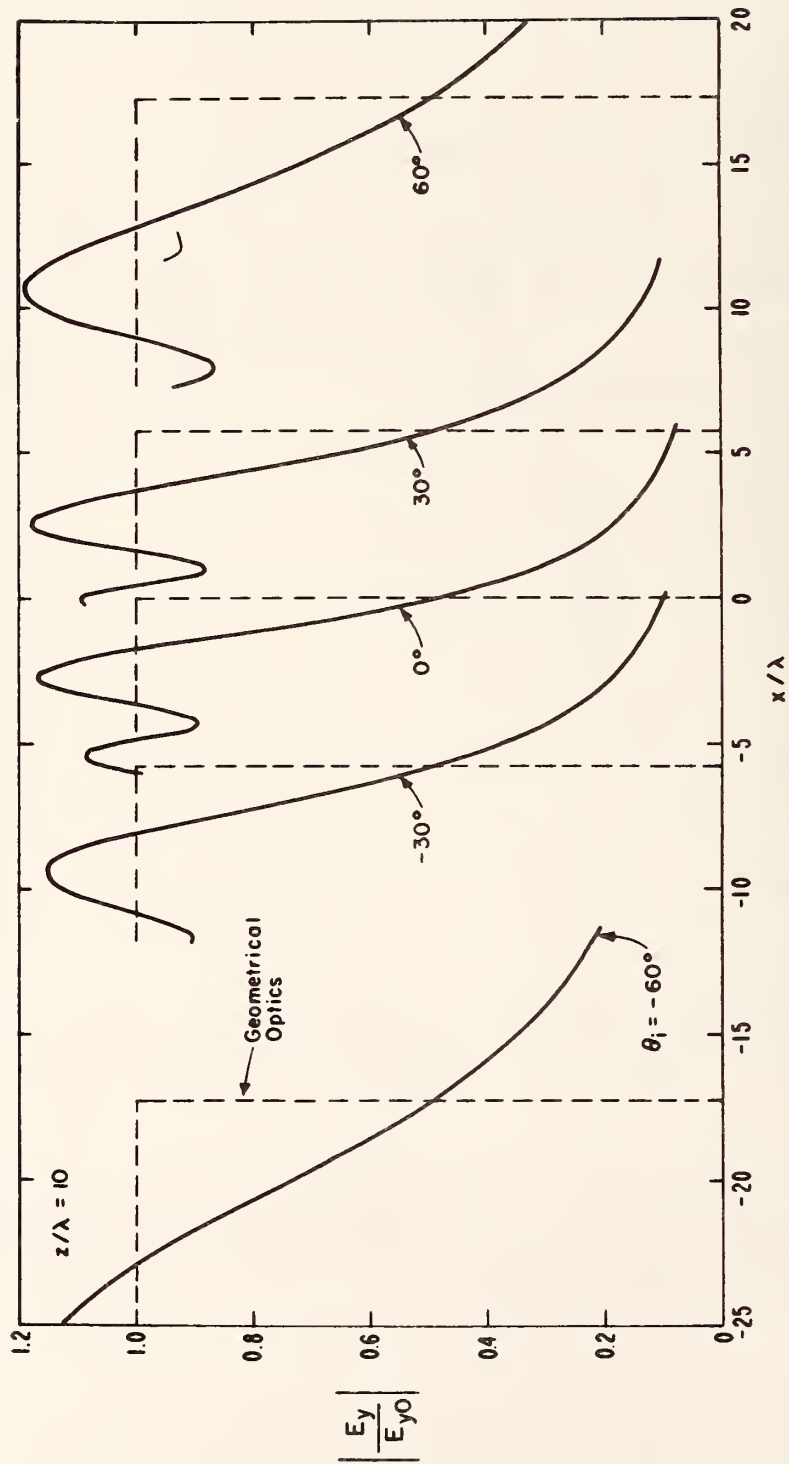


Figure 11. Magnitude of the normalized electric field of a semi-infinite current sheet for various incidence angles  $\theta_i$  ( $E_y$  polarization).

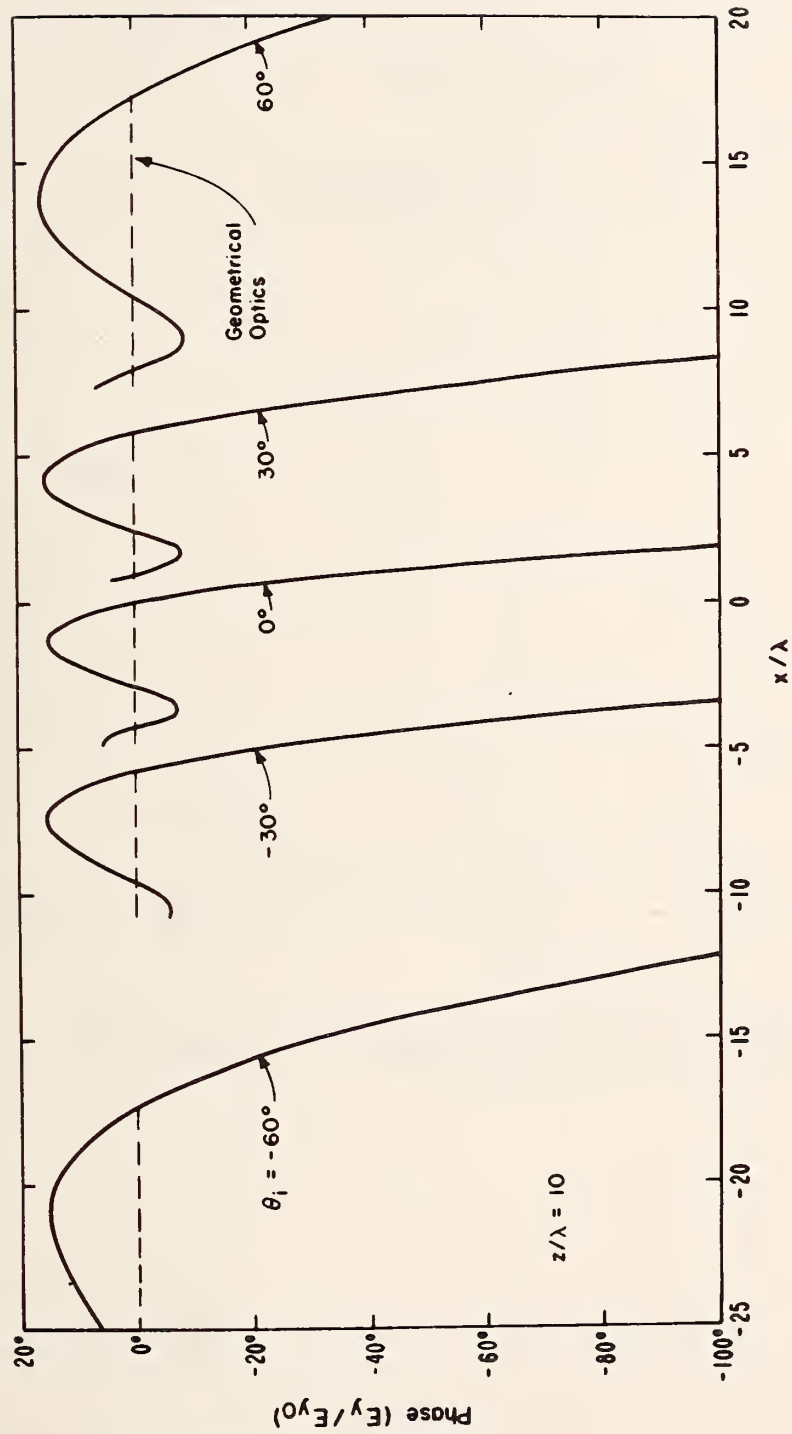


Figure 12. Phase of the normalized electric field of a semi-infinite current sheet for various incidence angles  $\theta_i$  ( $E_y$  polarization).

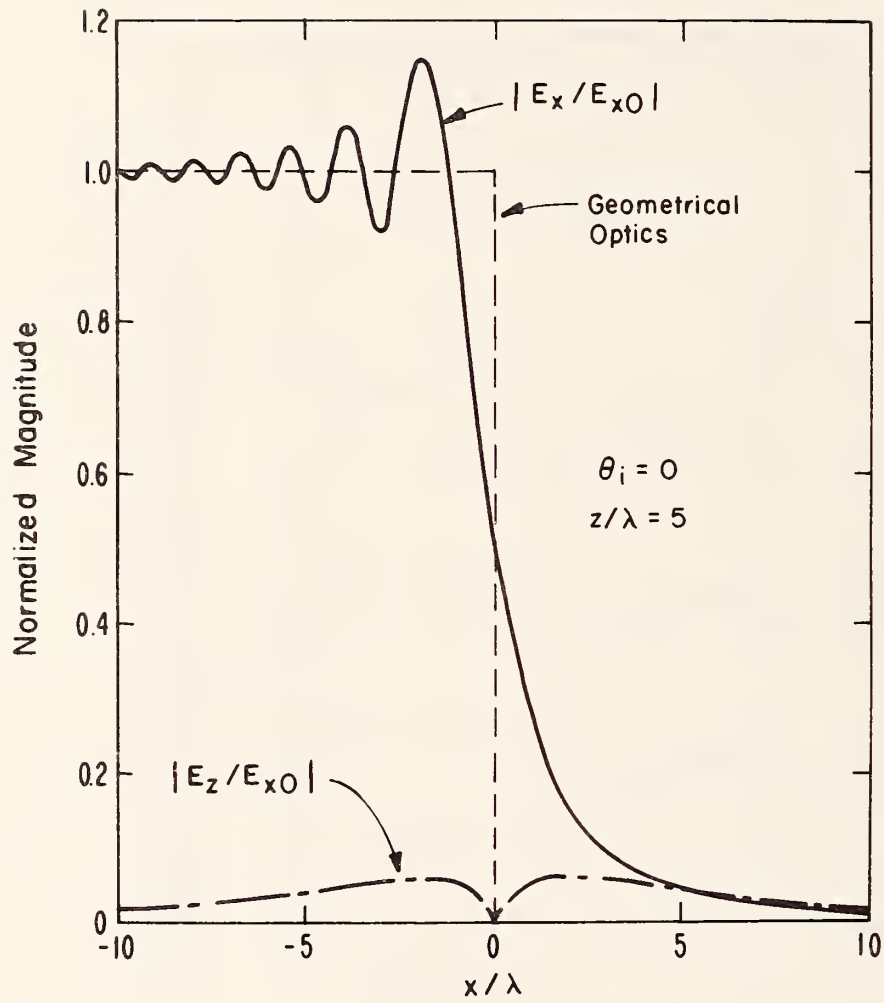


Figure 13. Magnitude of the normalized electric field of a semi-infinite current sheet ( $H_y$  polarization).

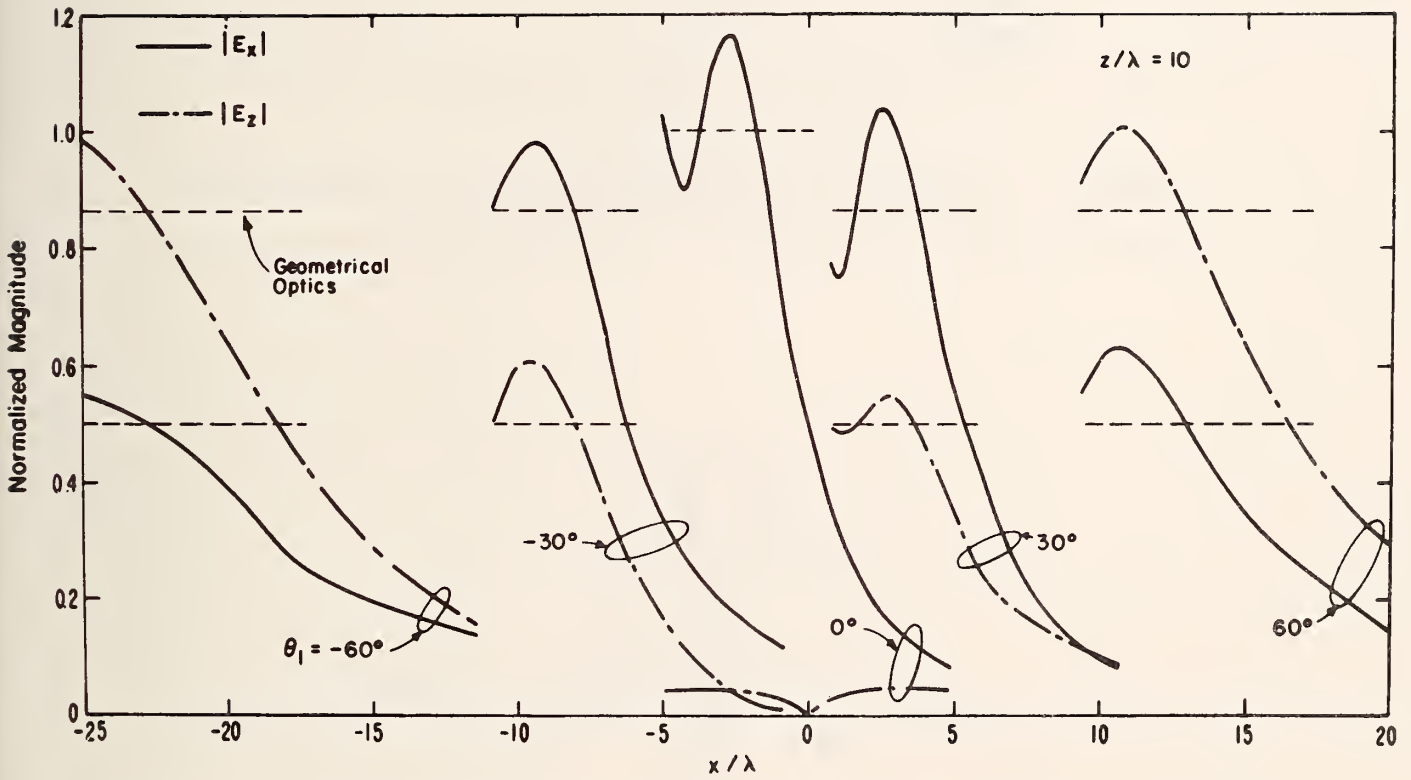


Figure 14. Magnitude of the normalized electric field of a semi-infinite current sheet for various incidence angles  $\theta_i$  ( $H_y$  polarization).

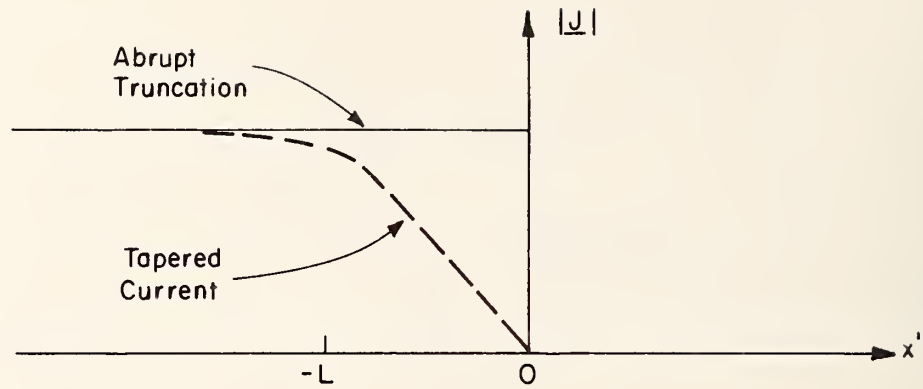


Figure 15. Comparison of truncated current and tapered current.

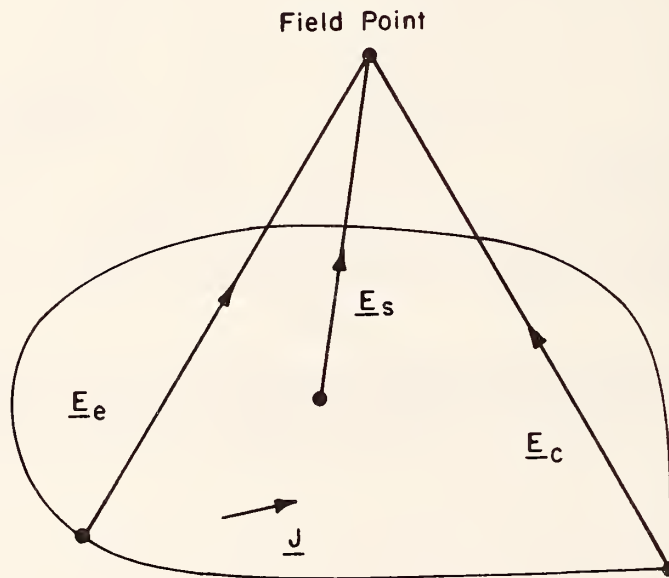


Figure 16. Stationary phase ( $\underline{E}_s$ ), edge diffracted ( $\underline{E}_e$ ), and corner diffracted ( $\underline{E}_c$ ) field contributions from surface currents  $\underline{J}$ .

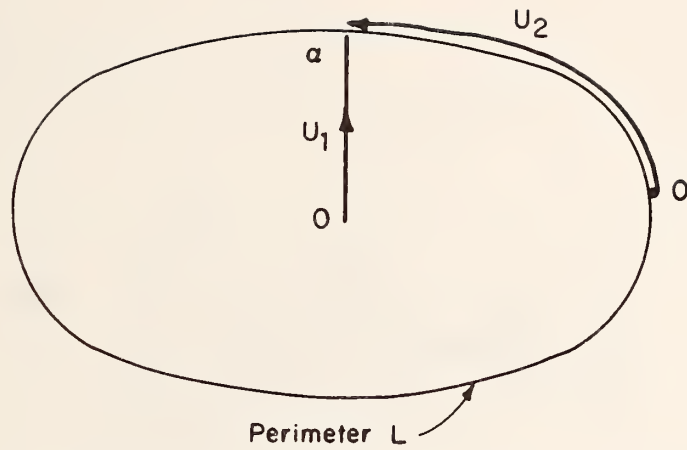


Figure 17. Coordinate system for calculation of edge diffraction.

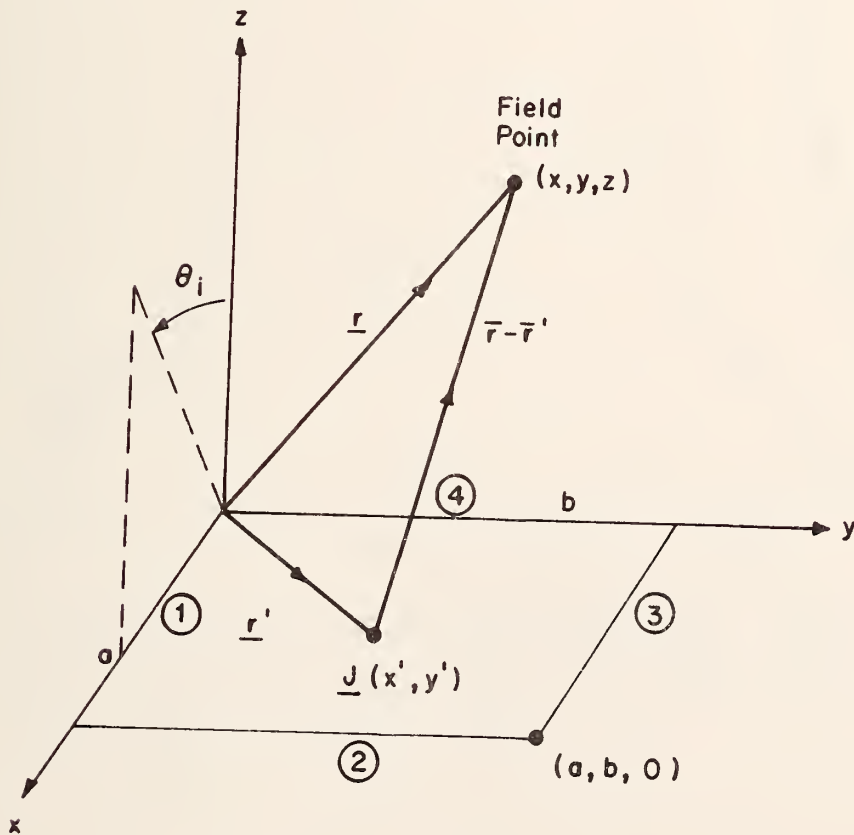


Figure 18. Rectangular current sheet of dimensions  $a$  by  $b$ . Each of the four edges (1-4) contributes to the edge diffracted field.

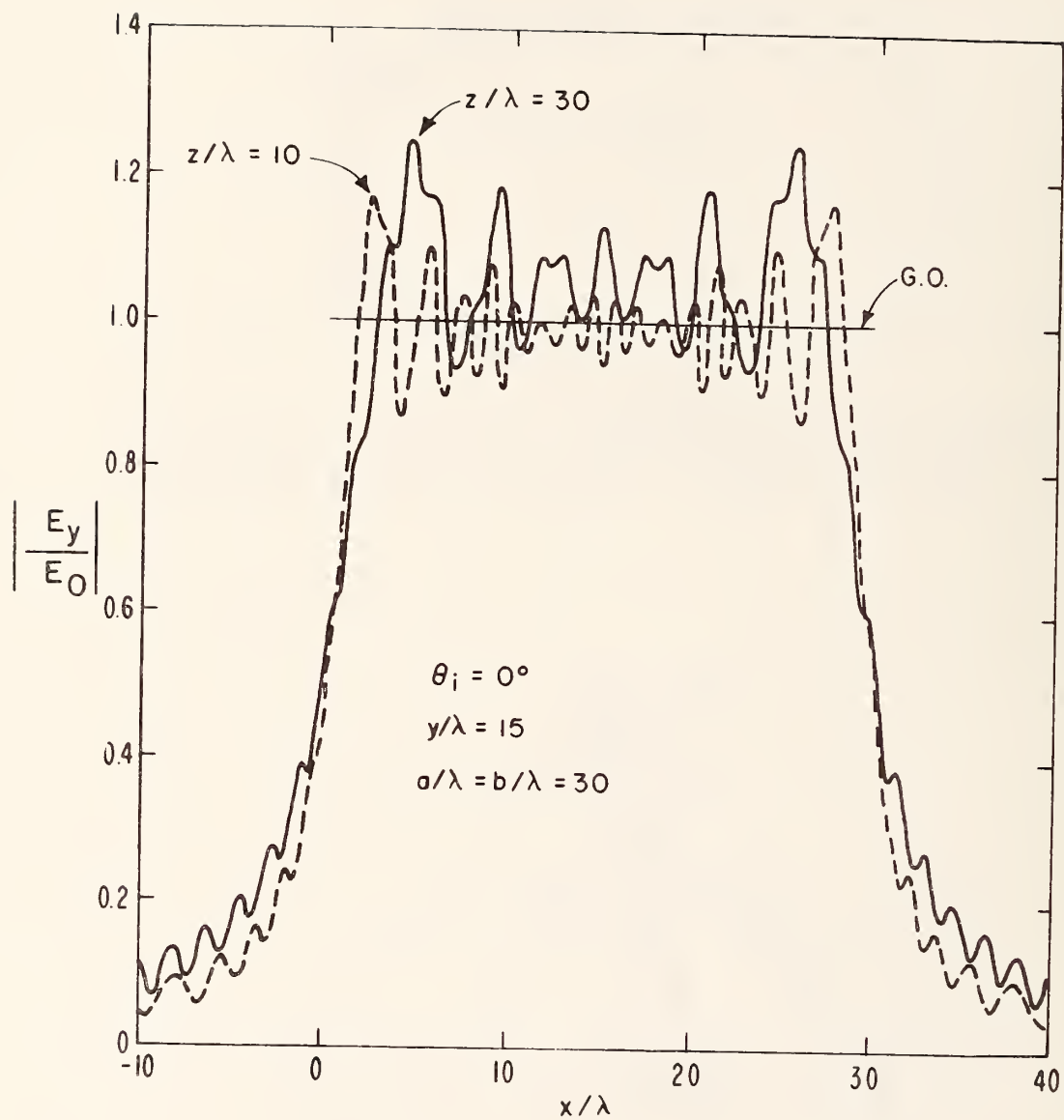


Figure 19. Magnitude of the normalized electric field radiated by a square current sheet. The geometrical optics approximation (g.o.) is shown for comparison.

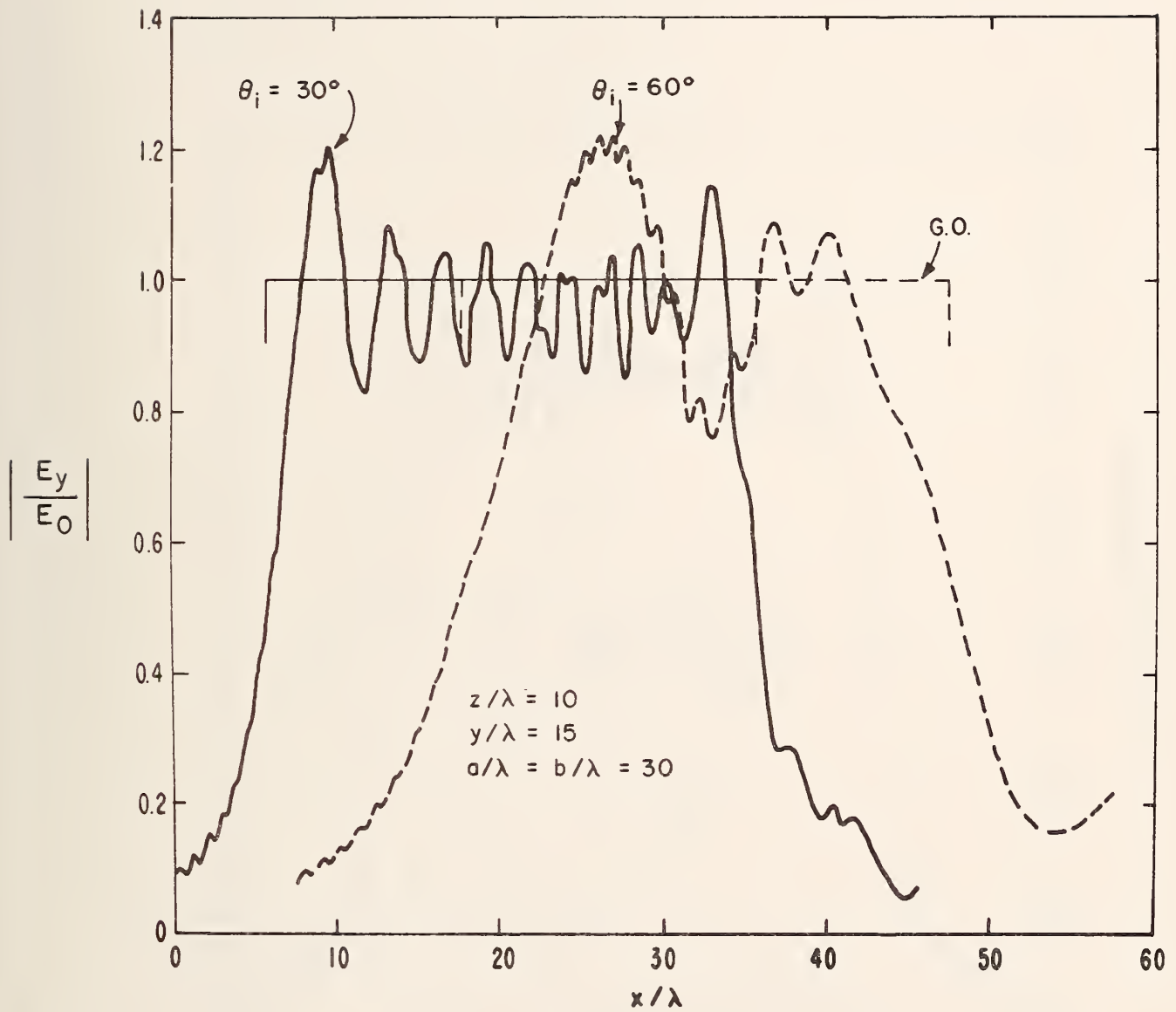


Figure 20. Magnitude of the normalized electric field radiated by a square current sheet for two scan angles,  $\theta_i = 30^\circ$  and  $60^\circ$ .

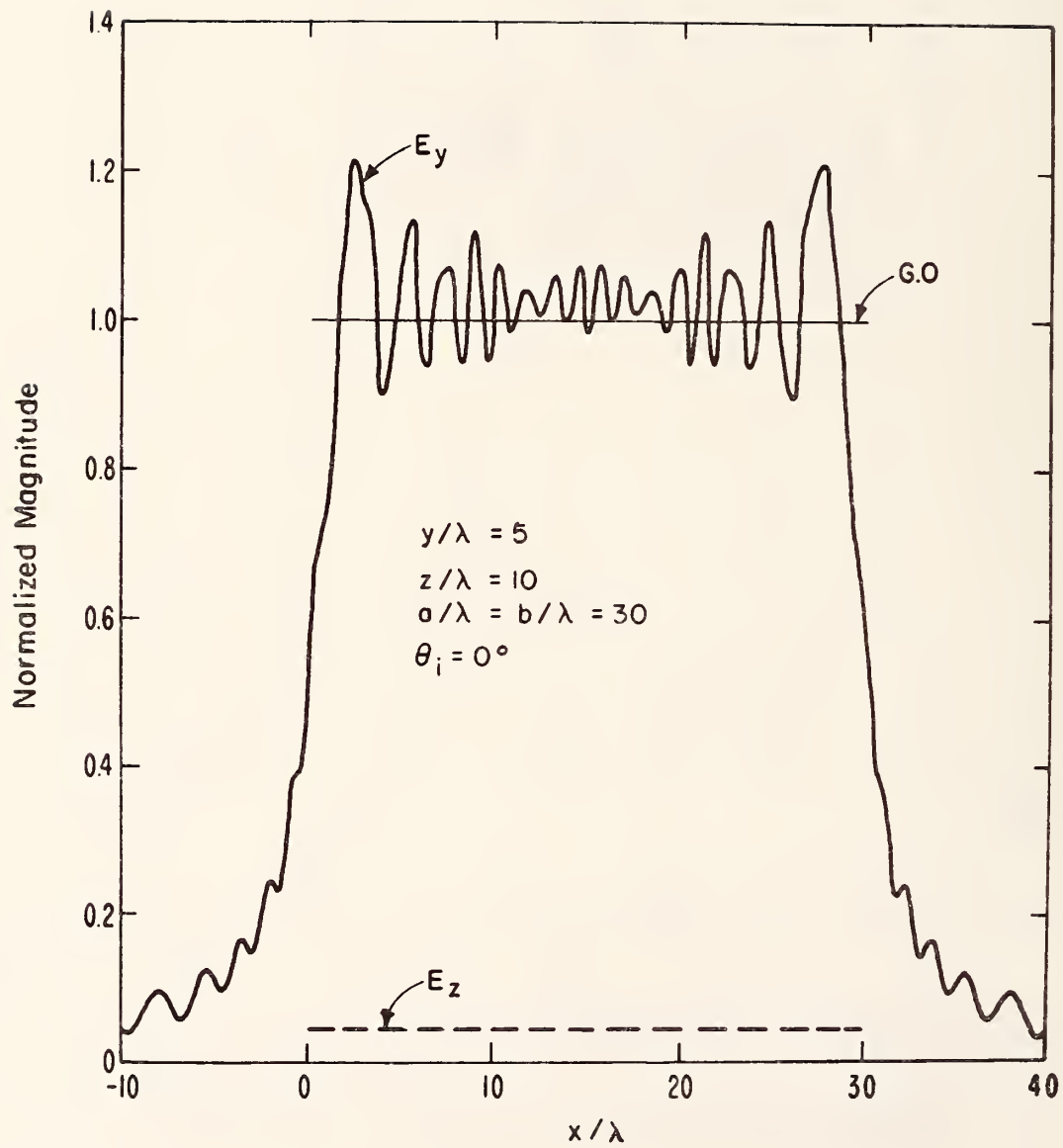


Figure 21. Magnitude of the normalized electric field radiated by a square current sheet for a cut off the center line,  $y/\lambda = 5$ .

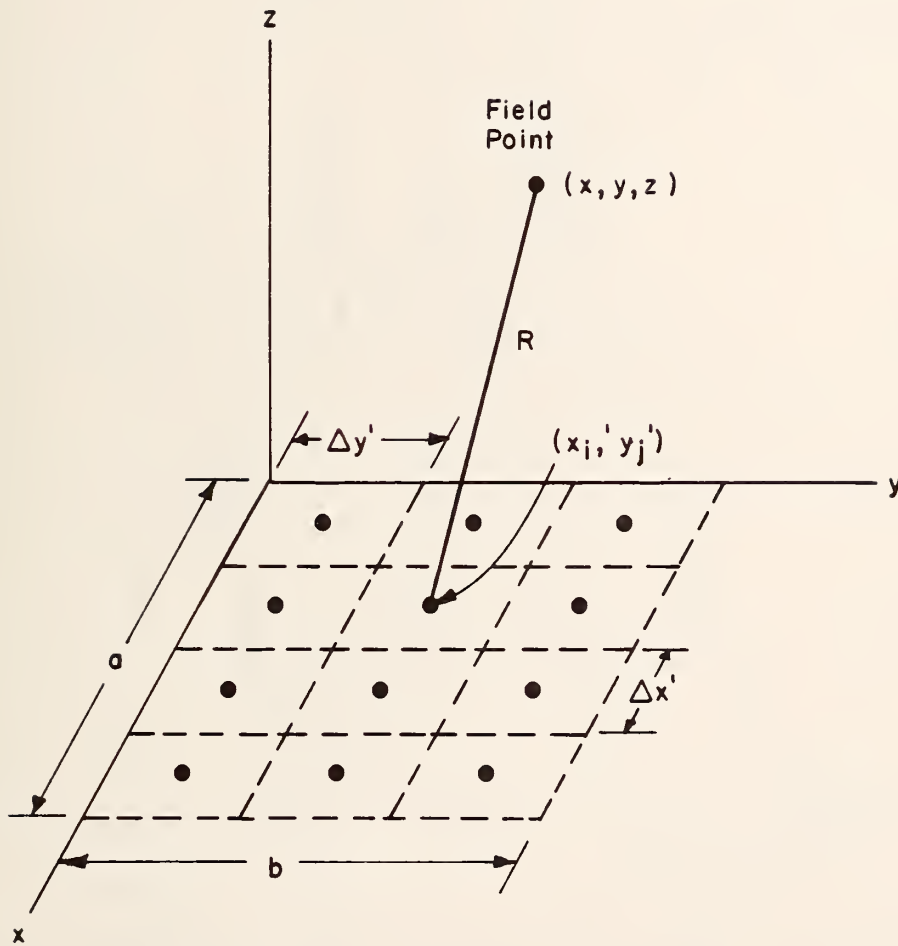


Figure 22. Geometry for a rectangular array of equally-spaced electric dipole elements or Huygens' sources.

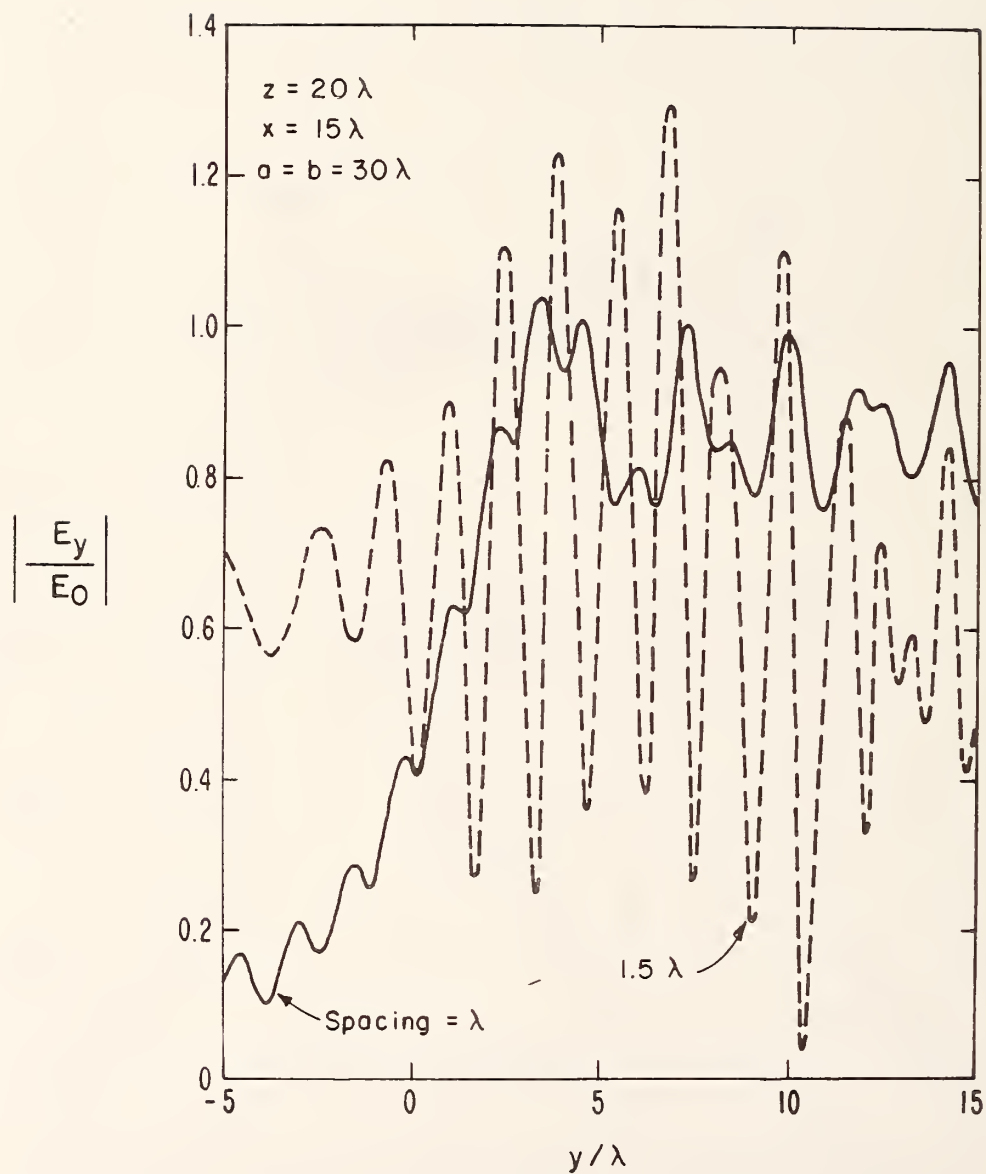


Figure 23. Normalized electric field strength of a uniform square array of electric dipoles. An interelement spacing of  $1.5 \lambda$  violates the sampling criteria of section 3.3.

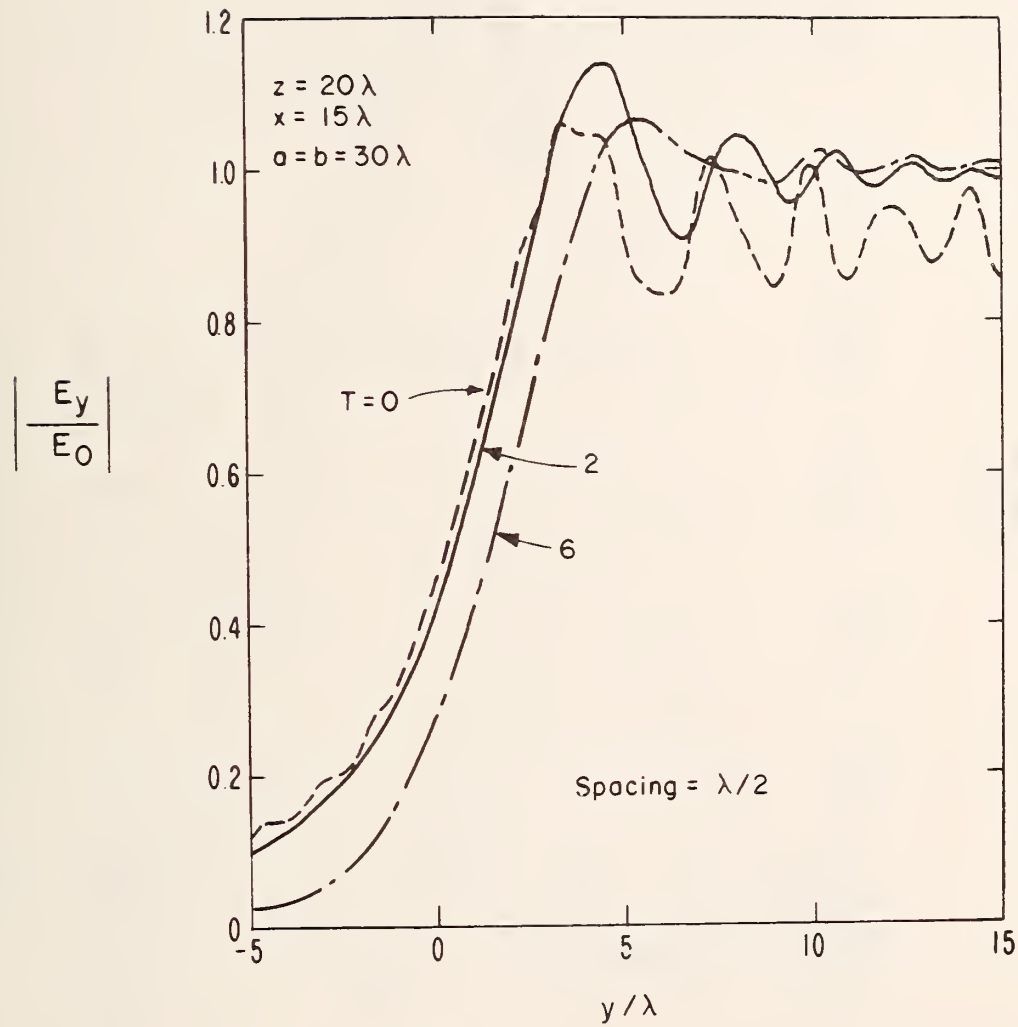


Figure 24. Normalized electric field strength of a tapered square array of electric dipoles. The curve for  $T = 0$  represents the uniform array.

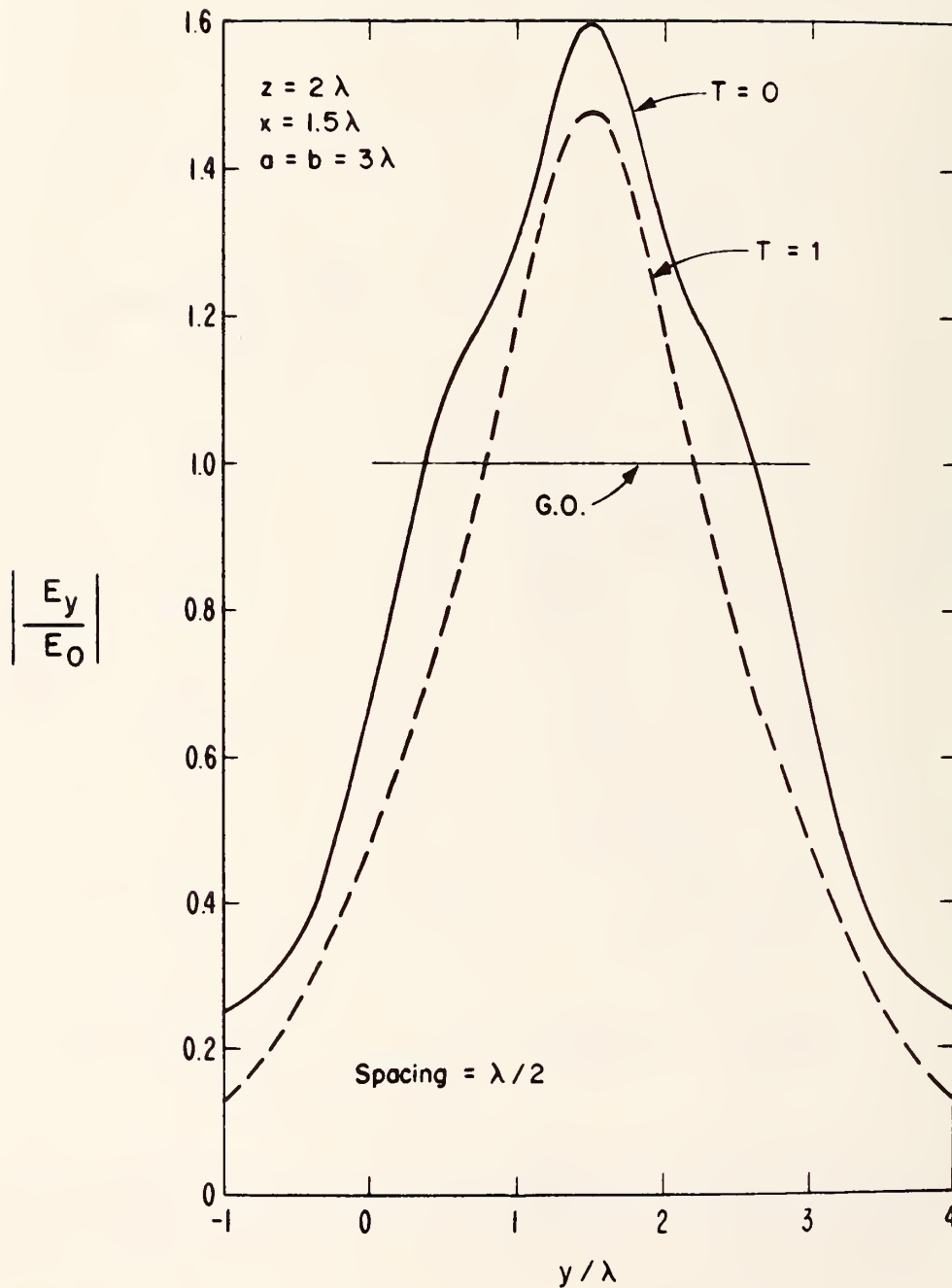


Figure 25. Normalized electric field strength of a small tapered array of electric dipoles. The geometrical optics field (g.o.) is shown for comparison.

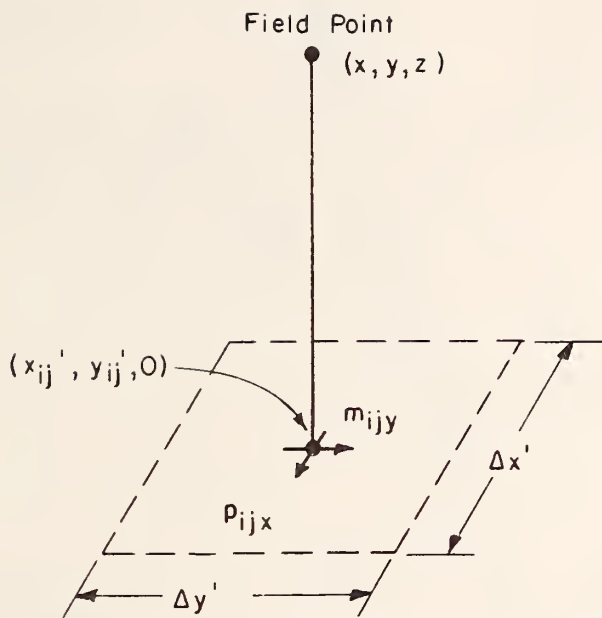


Figure 26. Electric and magnetic dipole moments,  $p_{ijx}$  and  $m_{ijy}$ , of a Huygens' source.

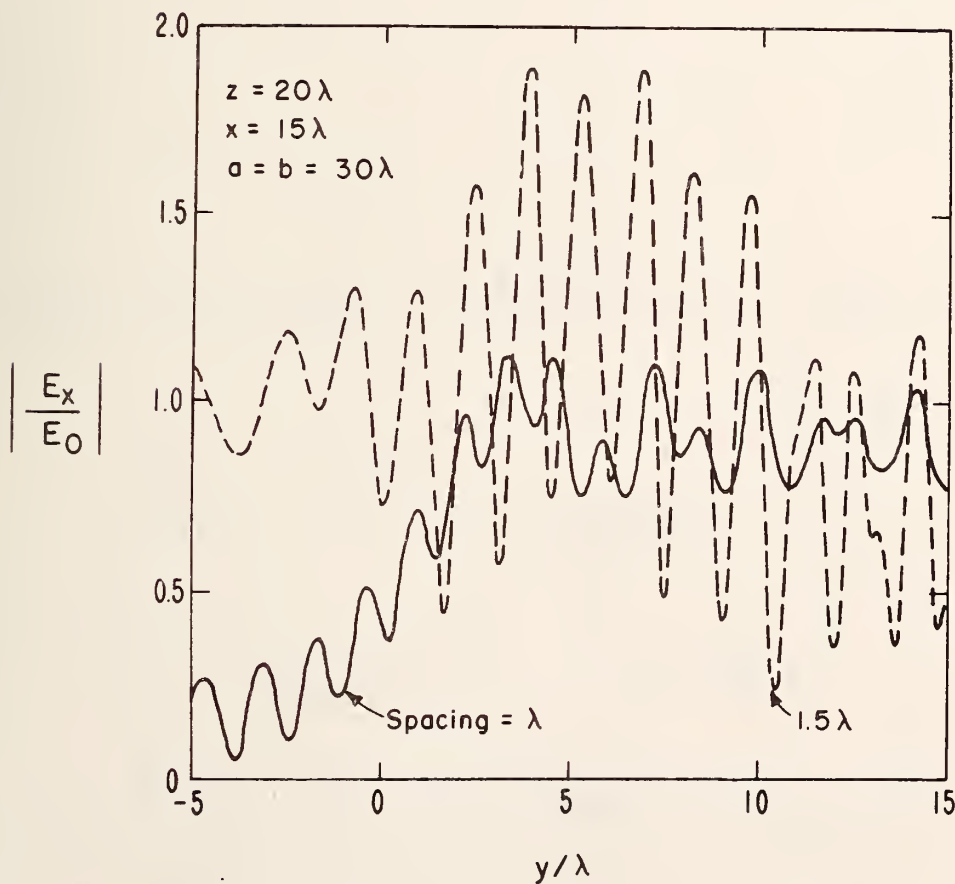


Figure 27. Normalized electric field strength of a uniform square array of Huygens' sources. An interelement spacing of  $1.5\lambda$  violates the sampling criteria of section 3.3.

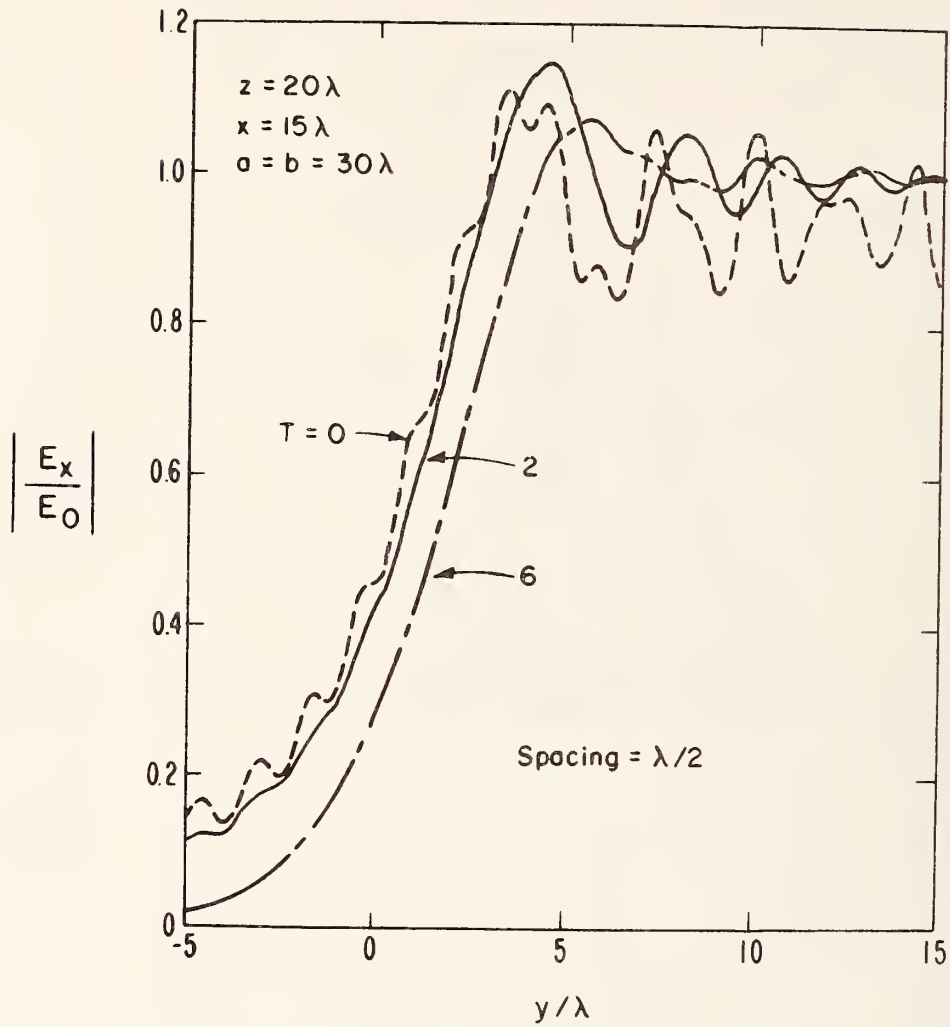


Figure 28. Normalized electric field strength of a tapered square array of Huygens' sources. The curve for  $T = 0$  represents the uniform array.

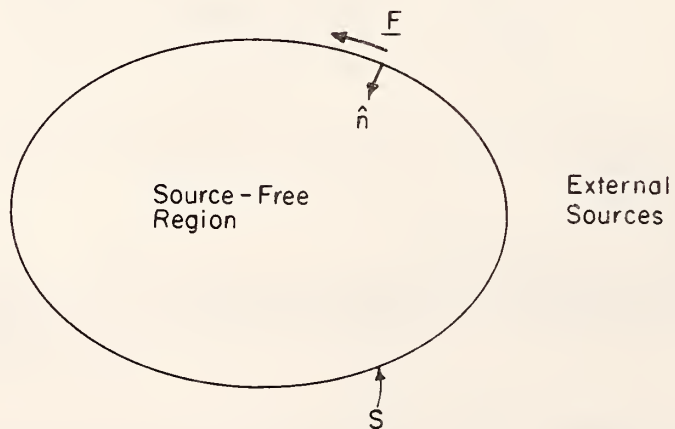


Figure 29 Source-free region enclosed by  $S$ .  $\vec{F}$  is a tangential vector which uniquely determines the interior fields

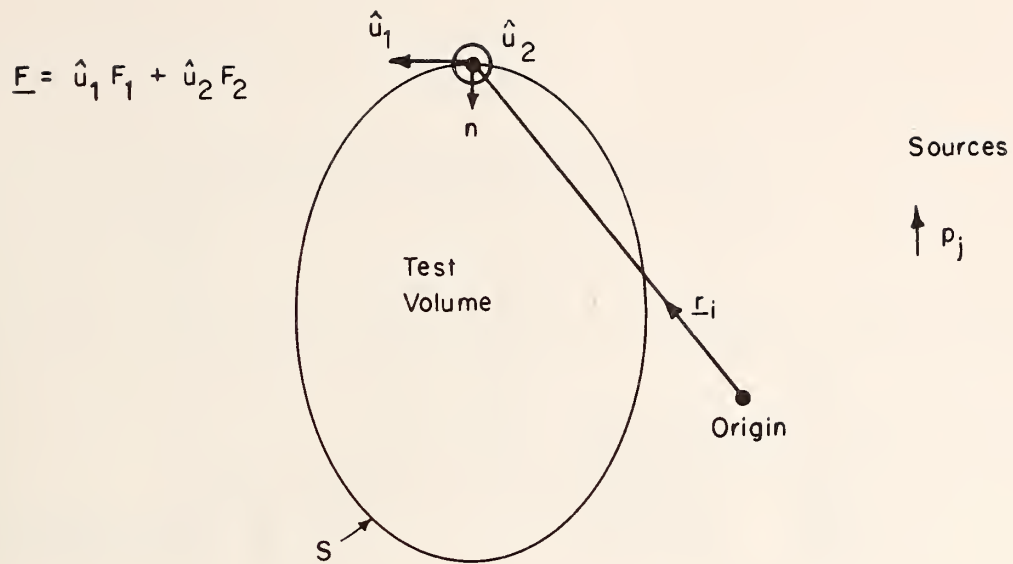


Figure 30. Geometry for near-field synthesis. The vector  $\underline{F}$  is tangential to the surface  $S$ .

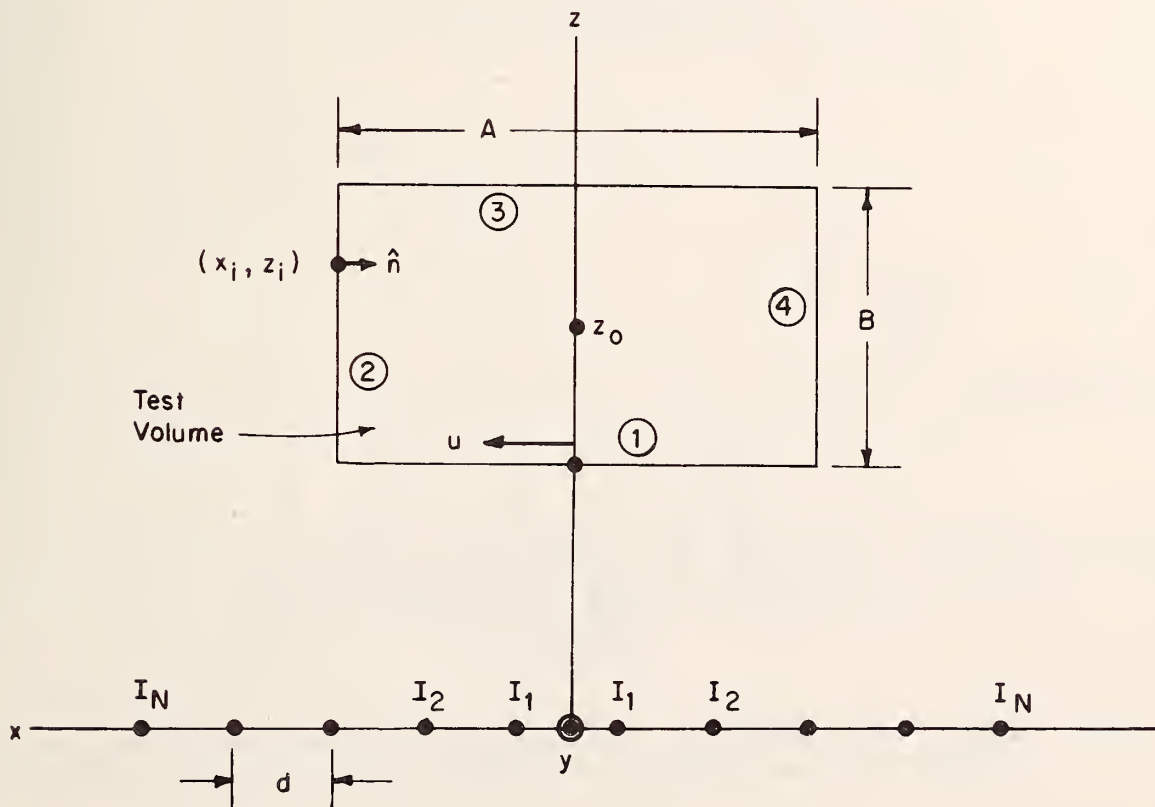


Figure 31. An array of  $y$ -directed electric line current sources illuminating a rectangular test volume.

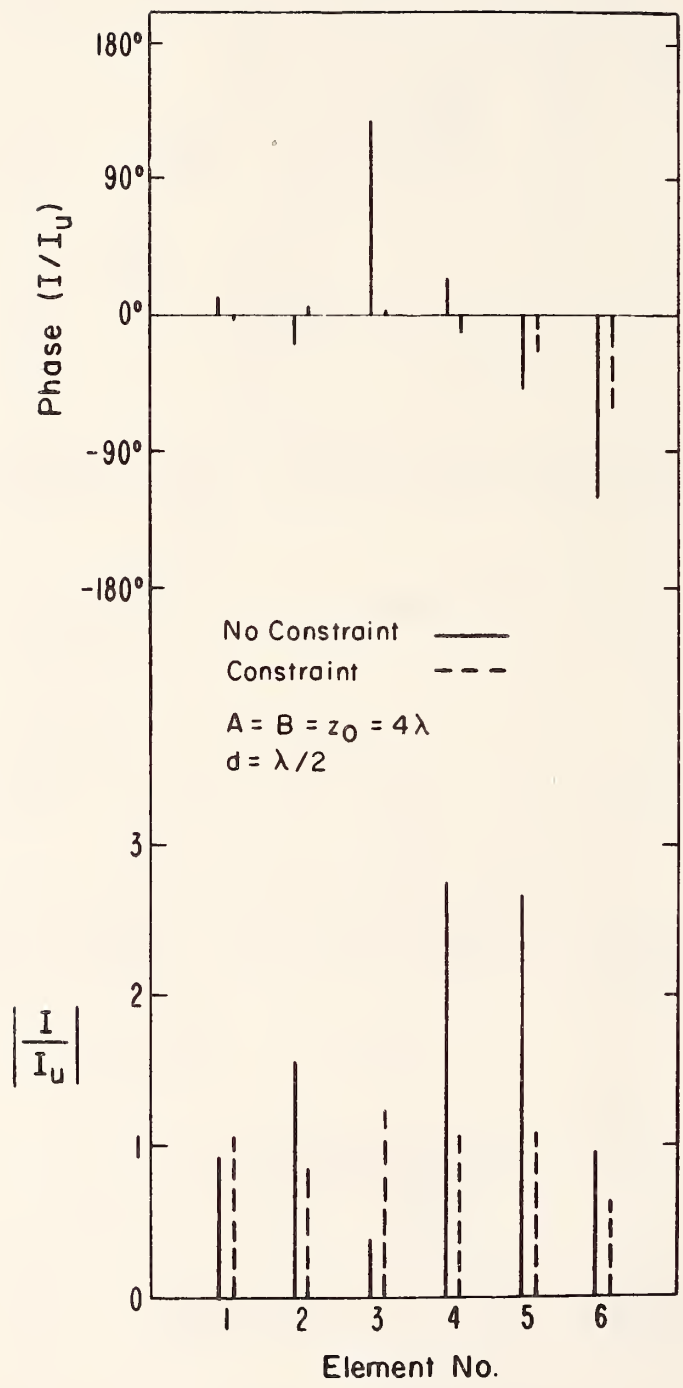


Figure 32. Magnitude and phase of the synthesized currents for an array of 12 elements with and without a constraint.

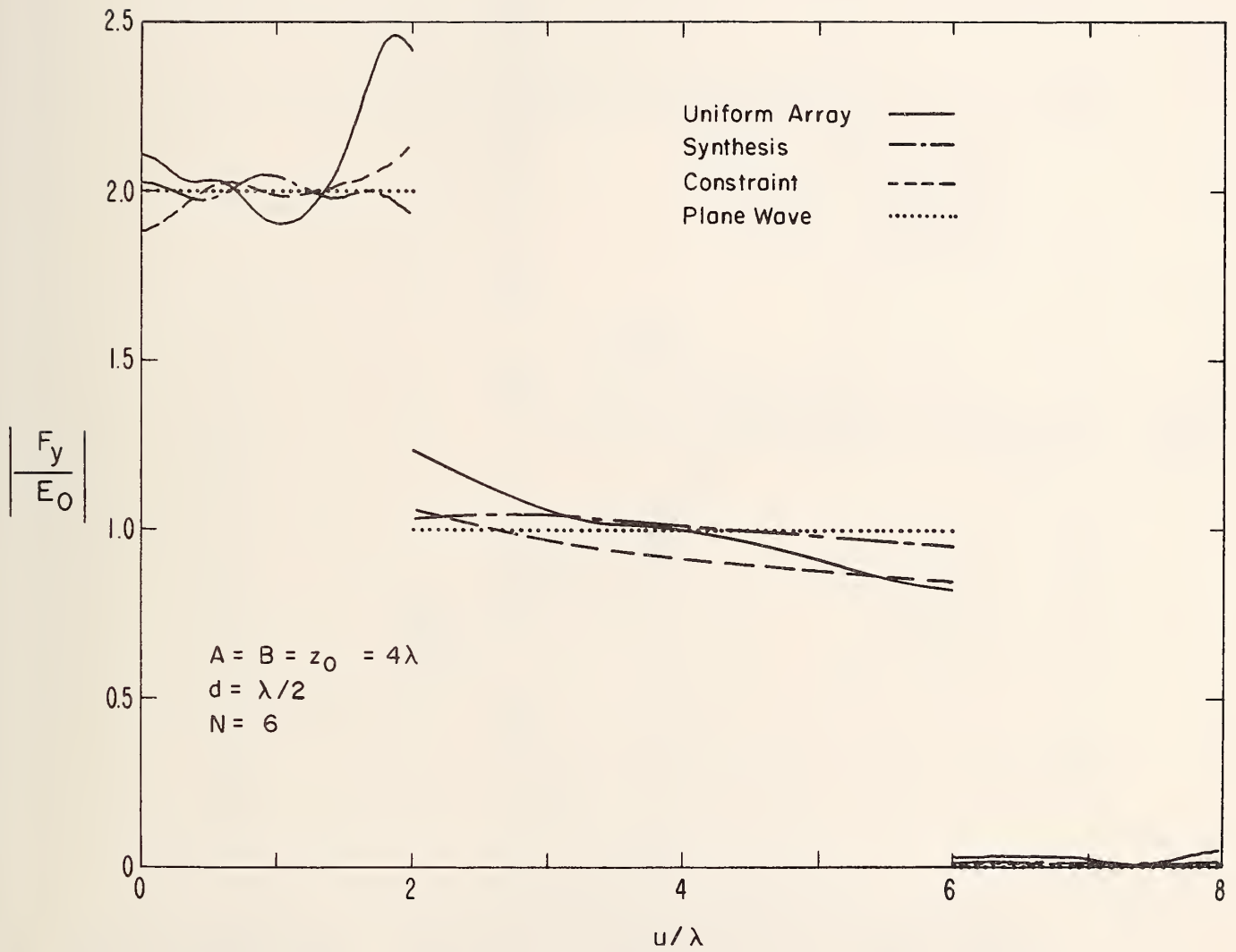


Figure 33. Normalized magnitude of the uniqueness function for a uniform array, a synthesized array, and a constrained array. The perfect plane wave result is shown for comparison.

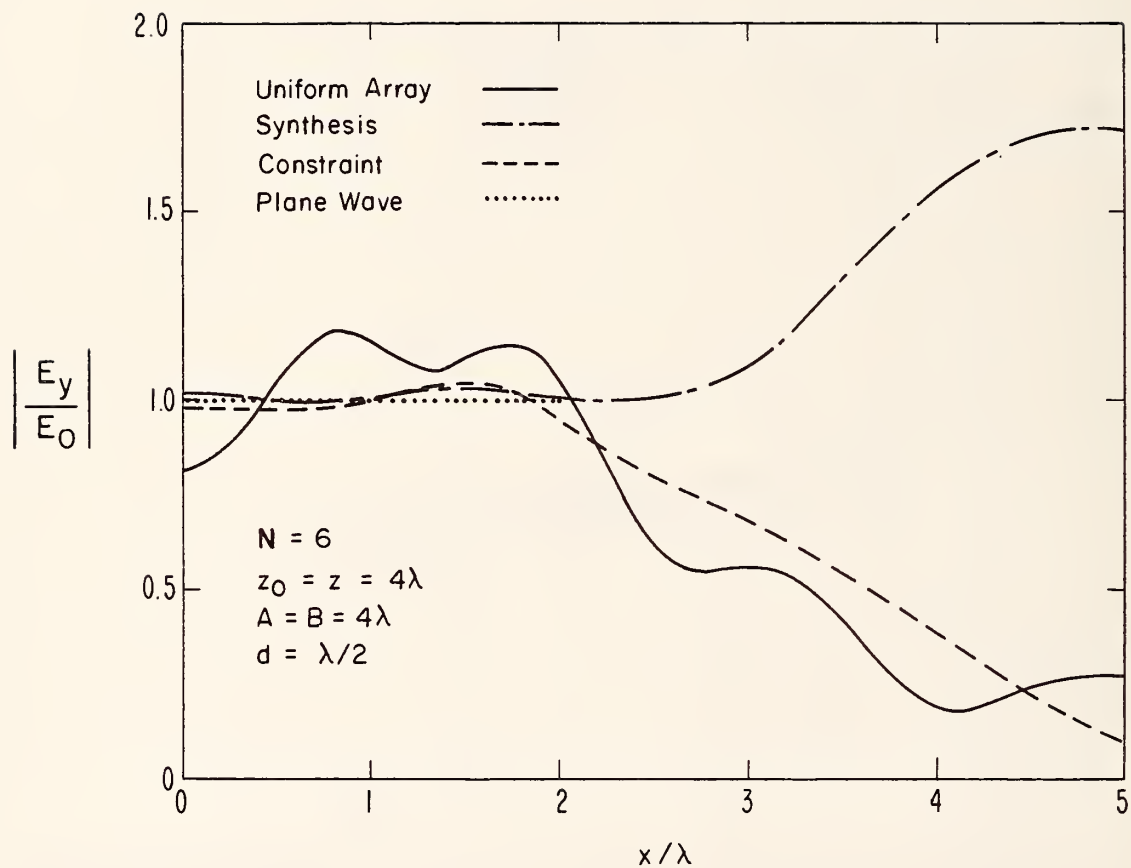


Figure 34. Normalized magnitude of the electric field for a uniform array, a synthesized array, and a constrained array. The perfect plane wave is shown for comparison.

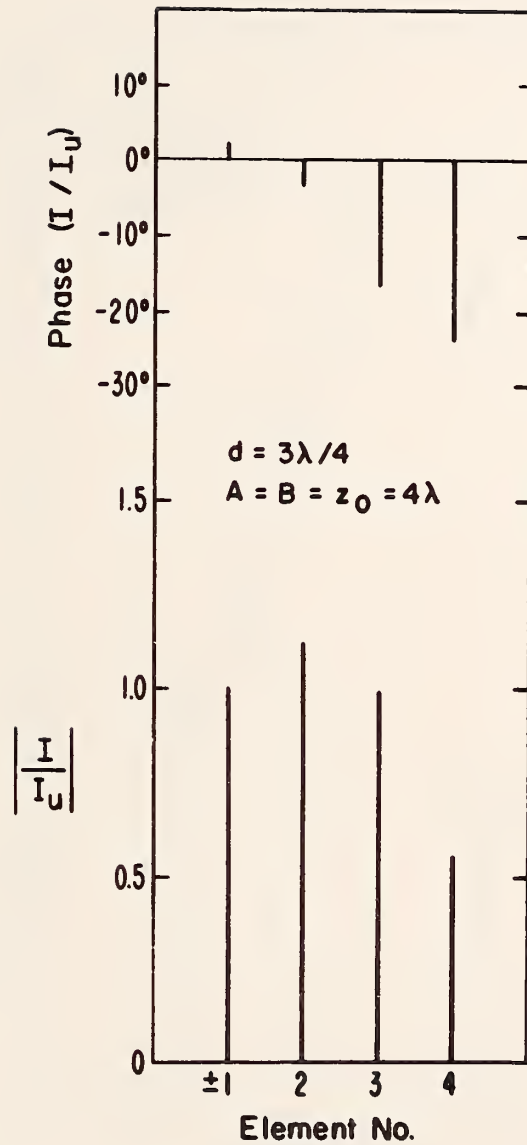


Figure 35. Magnitude and phase of the synthesized currents for an array of 8 elements. In this case, the constraint has no effect.

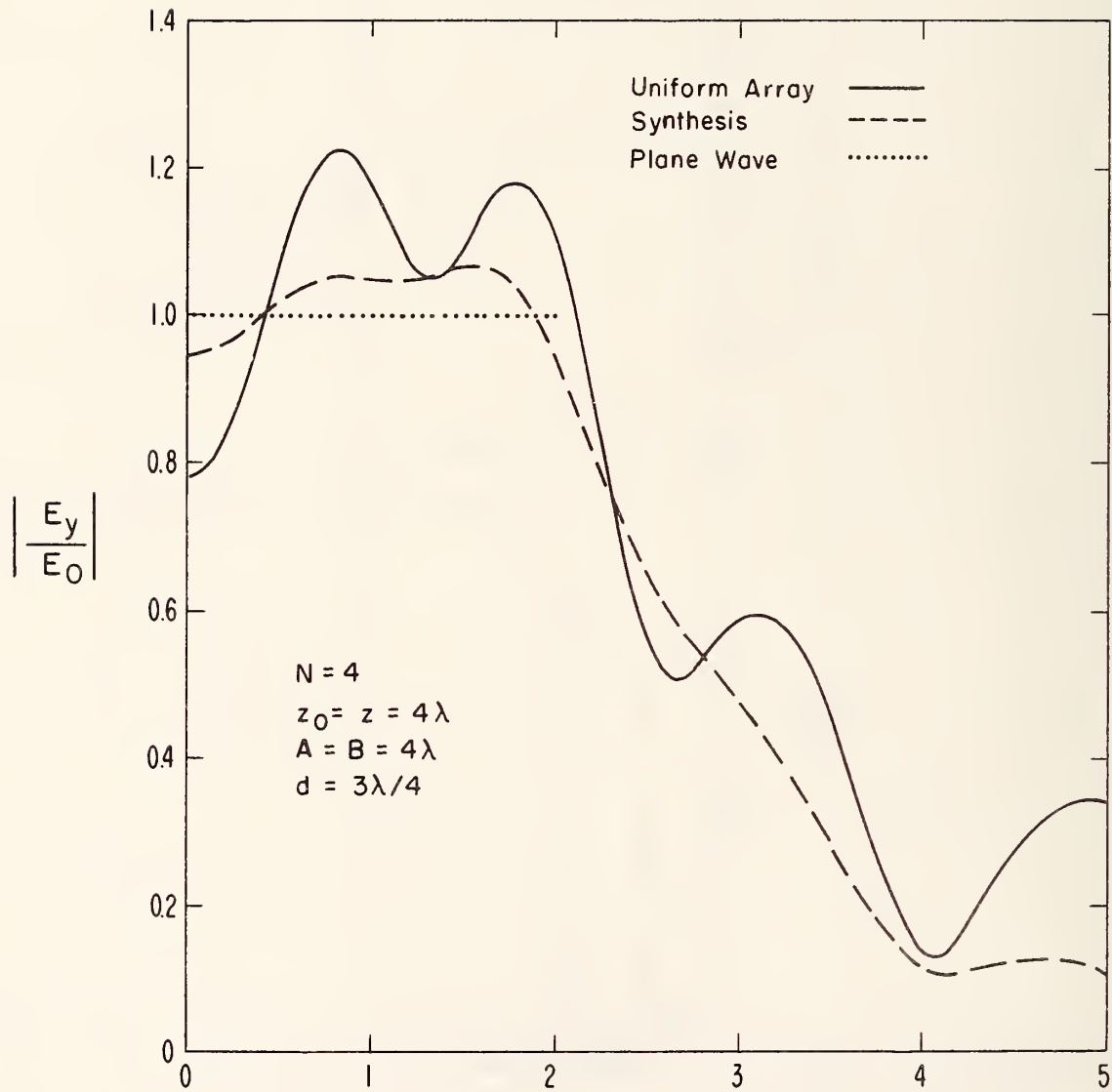


Figure 36. Normalized magnitude of the electric field for a uniform array and a synthesized array. The perfect plane wave is shown for comparison.

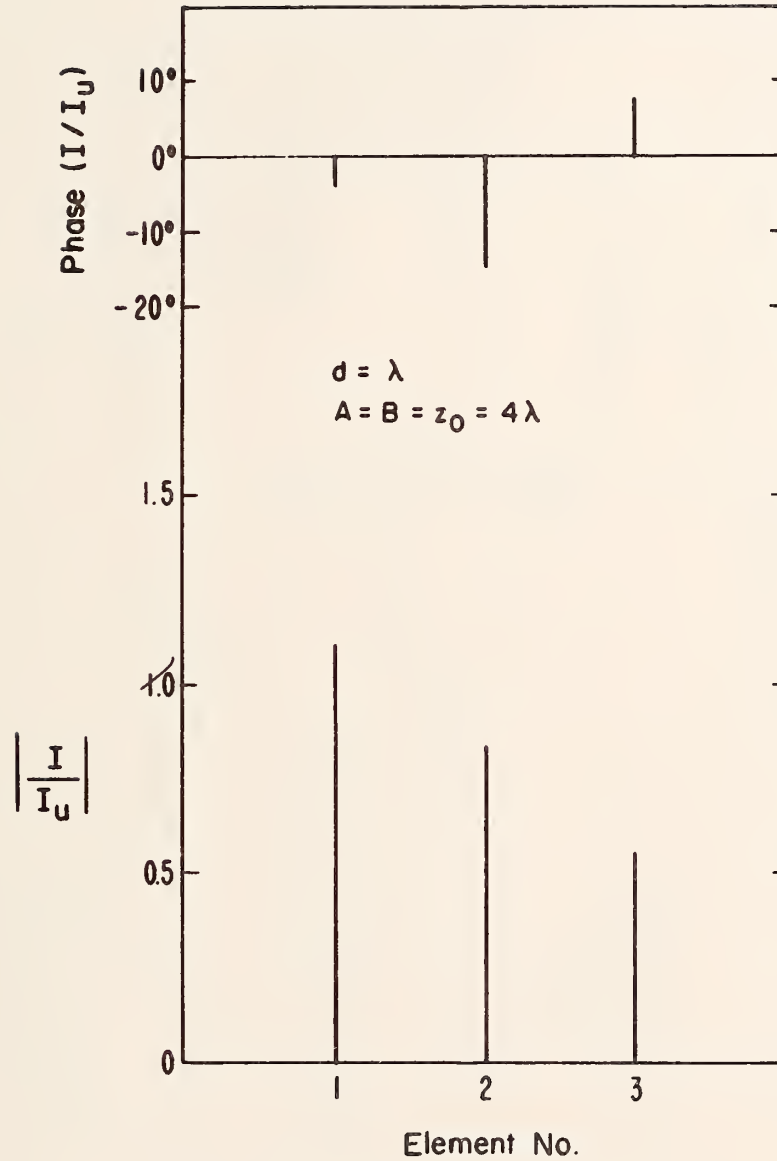


Figure 37. Magnitude and phase of the synthesized currents for an array of 6 elements. The constraint has no effect.

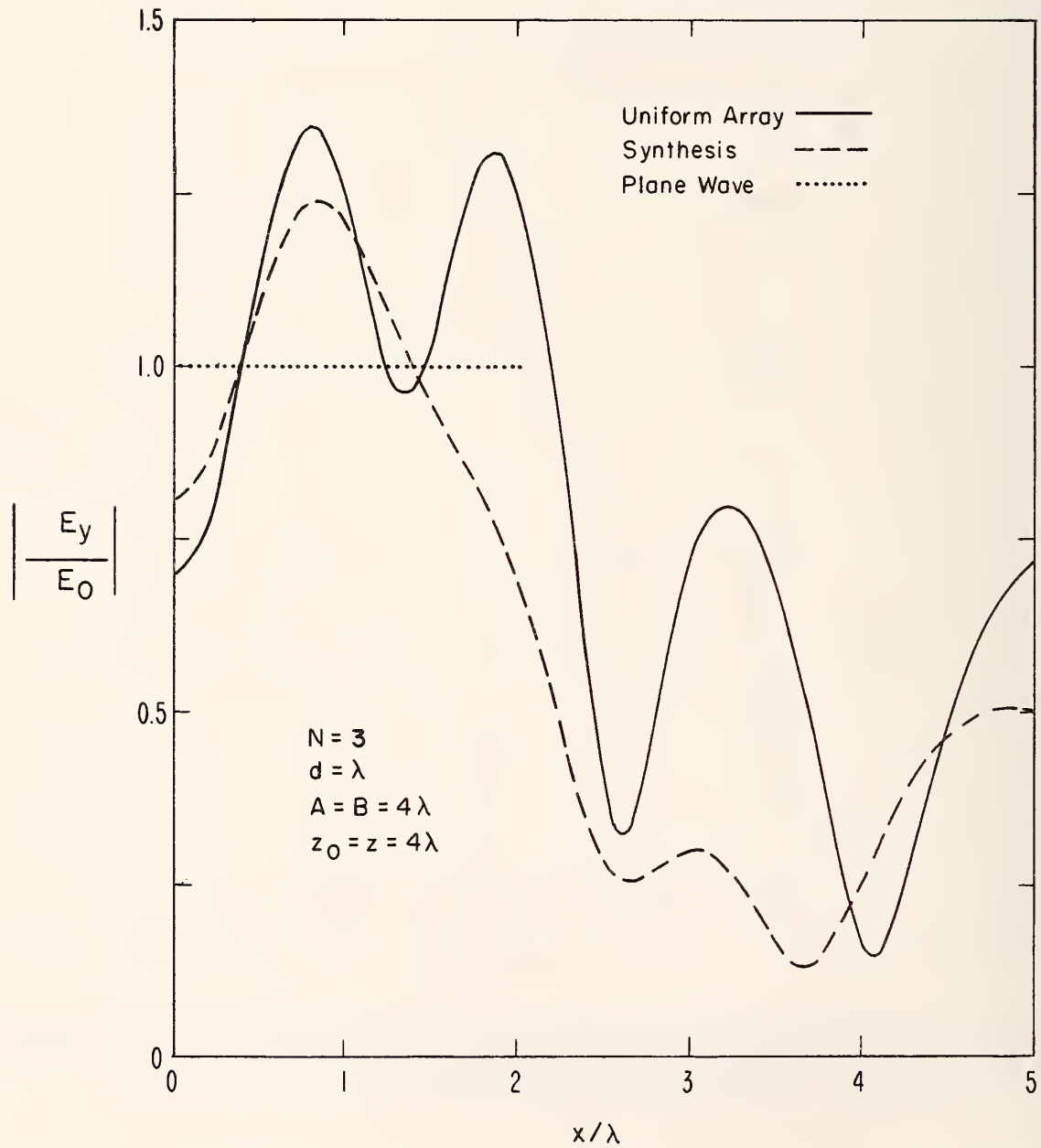


Figure 38. Normalized magnitude of the electric field for a uniform array and a synthesized array. The perfect plane wave is shown for comparison.

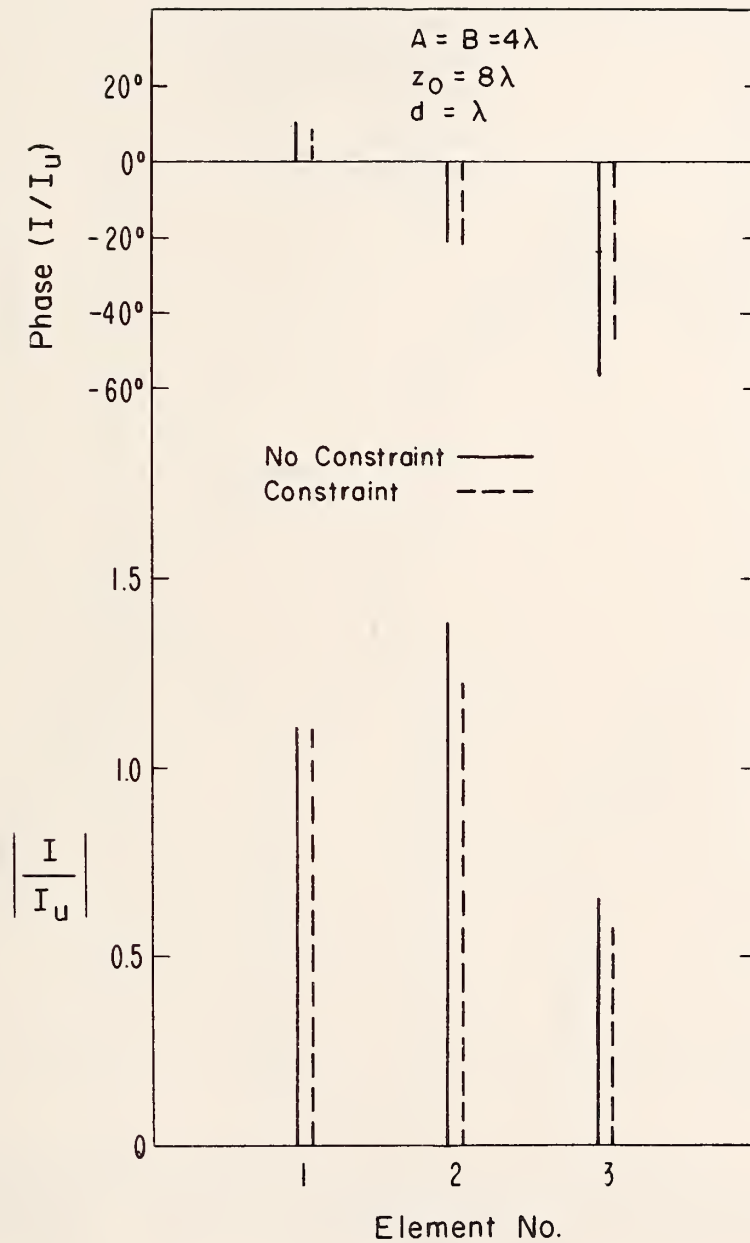


Figure 39. Magnitude and phase of the synthesized currents for an array of 6 elements with and without a constraint.

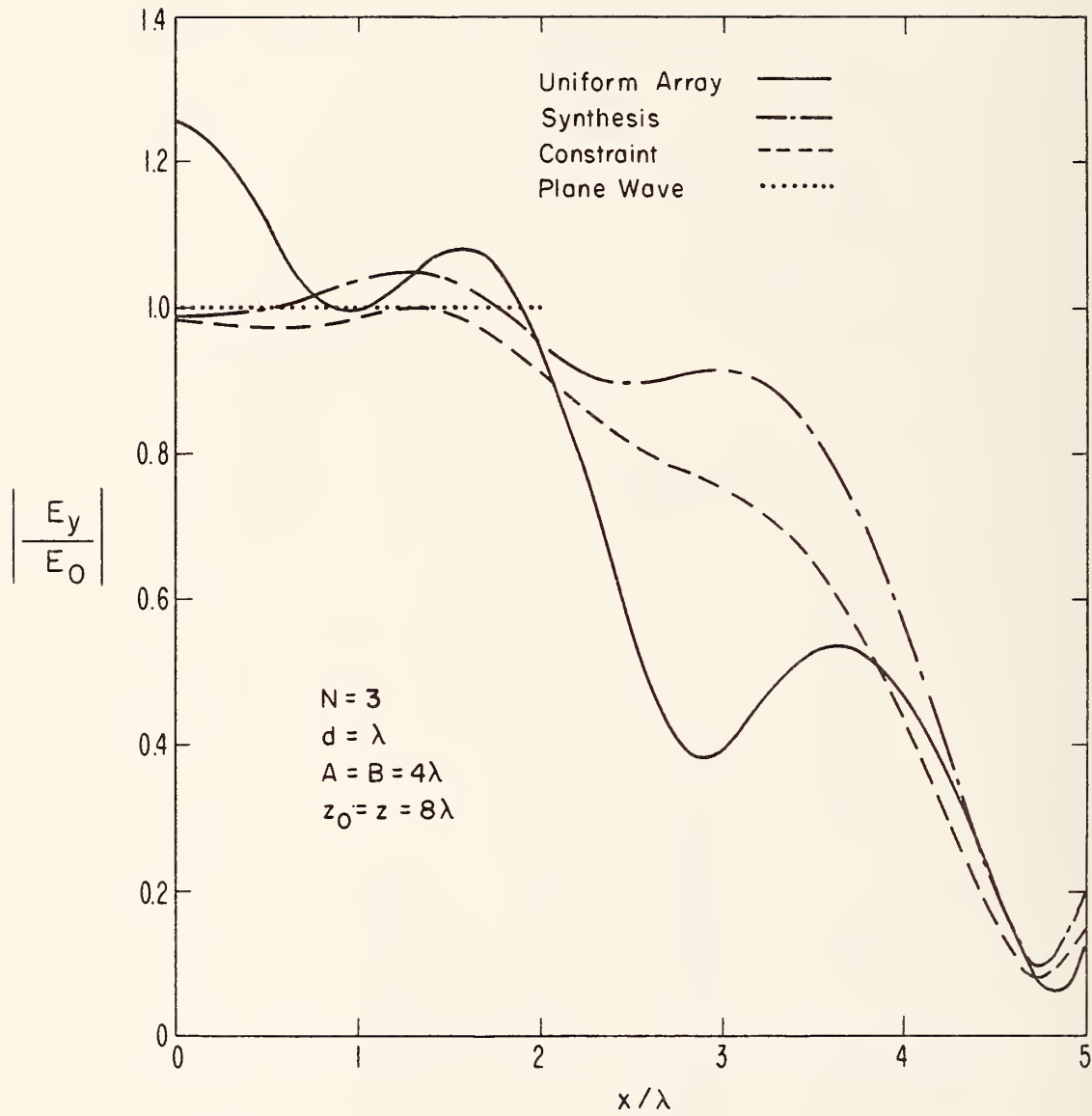


Figure 40. Normalized magnitude of the electric field for a uniform array, a synthesized array, and a constrained array. The perfect plane wave is shown for comparison.

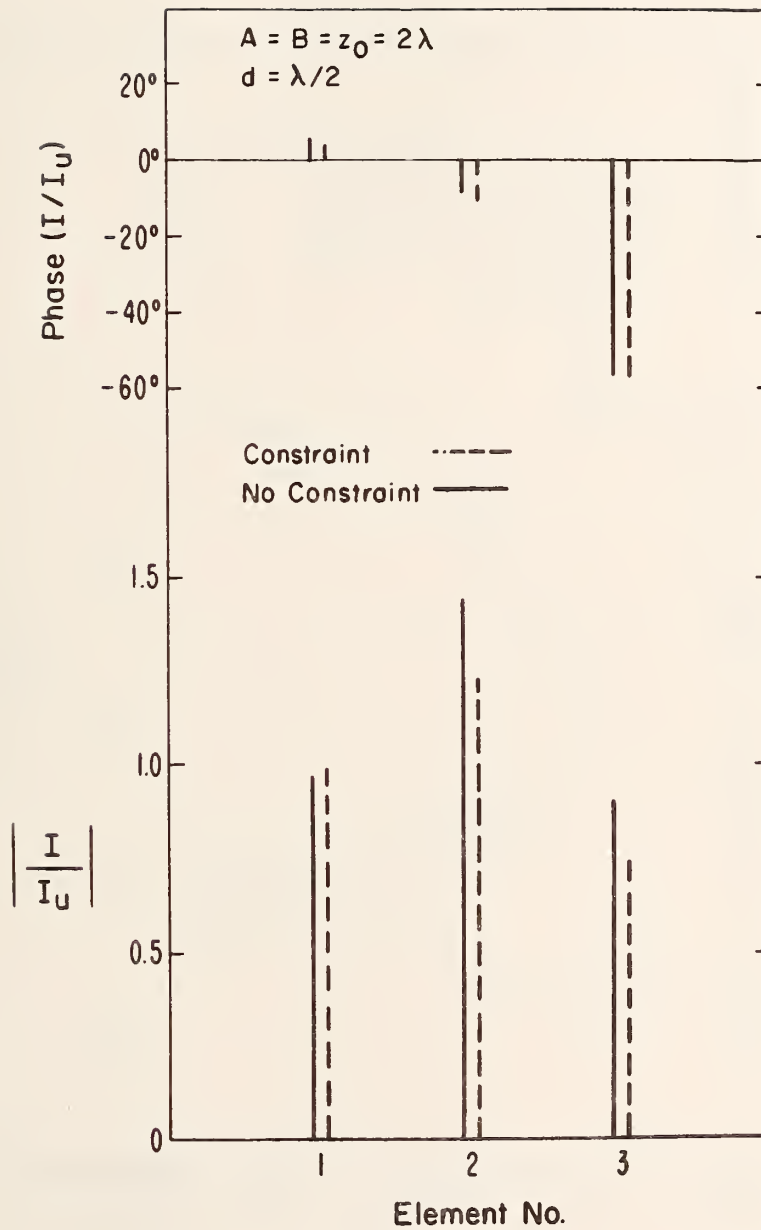


Figure 41. Magnitude and phase of the synthesized currents for an array of 6 elements with and without a constraint.

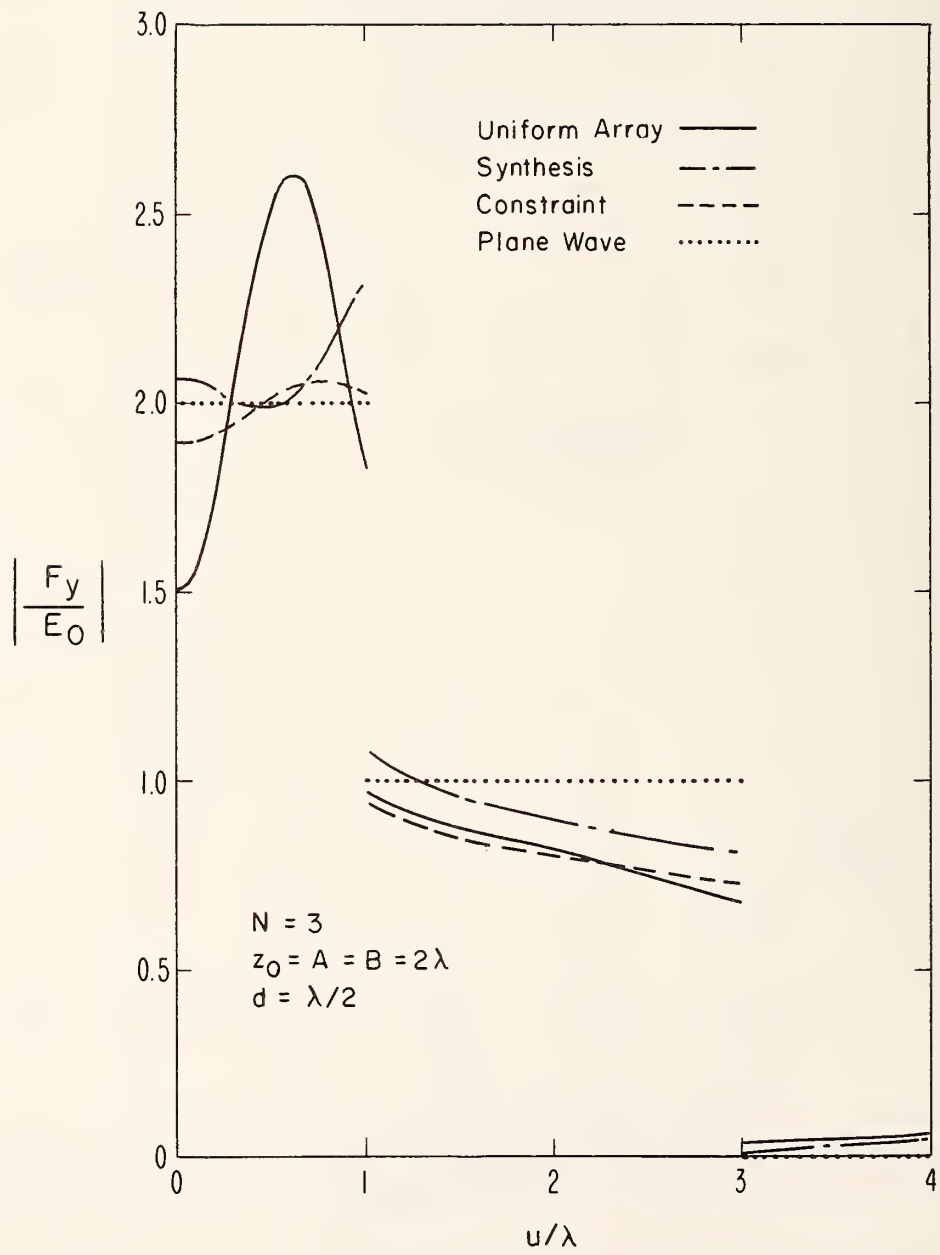


Figure 42. Normalized magnitude of the uniqueness function for a uniform array, a synthesized array, and a constrained array. The perfect plane wave is shown for comparison.

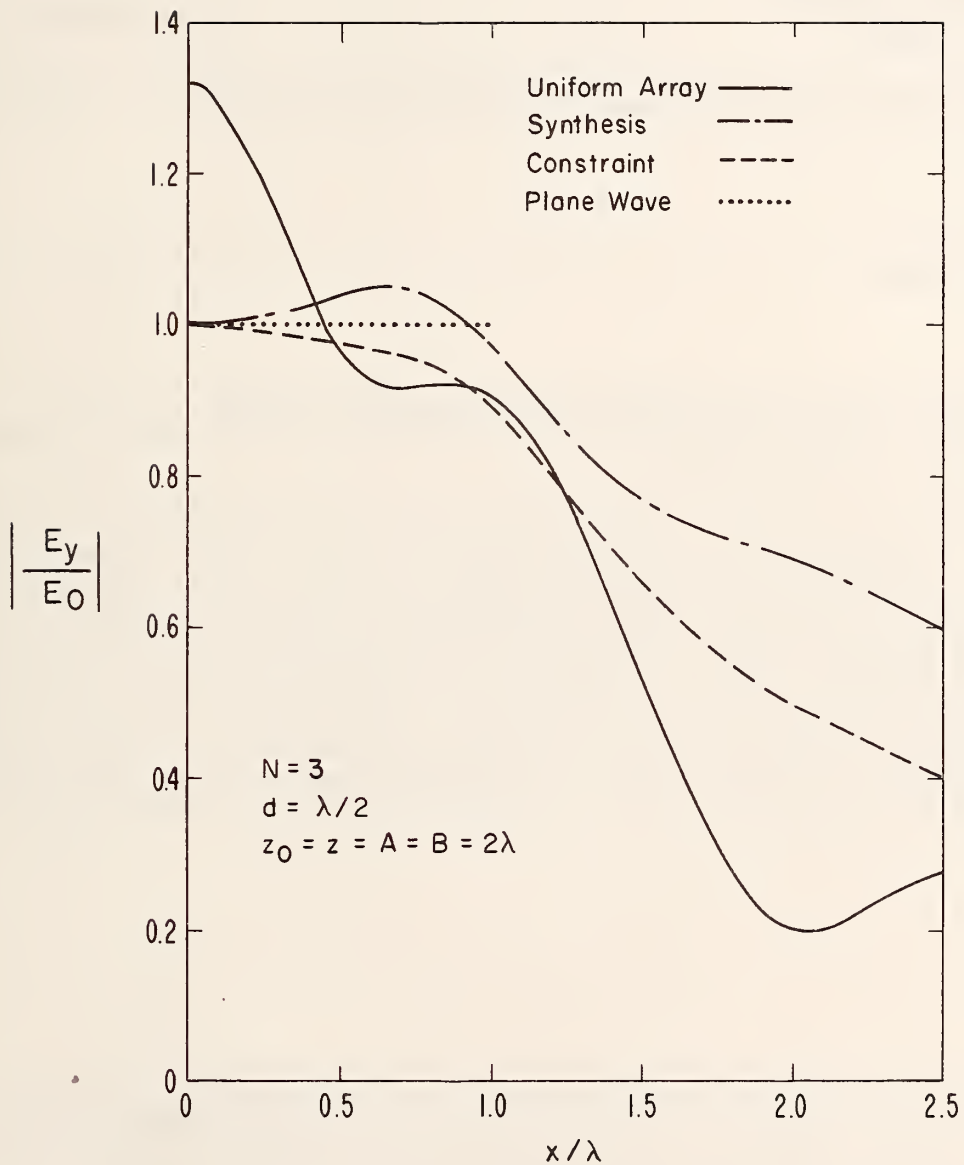


Figure 43. Normalized magnitude of the electric field for a uniform array, a synthesized array, and a constrained array. The perfect plane wave is shown for comparison.

U.S. DEPT. OF COMM. <b>BIBLIOGRAPHIC DATA SHEET</b> <i>(See instructions)</i>	<b>1. PUBLICATION OR REPORT NO.</b> NBS TN-1072	<b>2. Performing Organ. Report No.</b>	<b>3. Publication Date</b> February 1984
<b>4. TITLE AND SUBTITLE</b> <p style="text-align: center;">Theory of Near-Field Phased Arrays for Electromagnetic Susceptibility Testing</p>			
<b>5. AUTHOR(S)</b> David A. Hill			
<b>6. PERFORMING ORGANIZATION</b> <i>(If joint or other than NBS, see instructions)</i> NATIONAL BUREAU OF STANDARDS DEPARTMENT OF COMMERCE WASHINGTON, D.C. 20234		<b>7. Contract/Grant No.</b>	<b>8. Type of Report &amp; Period Covered</b>
<b>9. SPONSORING ORGANIZATION NAME AND COMPLETE ADDRESS</b> <i>(Street, City, State, ZIP)</i>			
<b>10. SUPPLEMENTARY NOTES</b>  <input type="checkbox"/> Document describes a computer program; SF-185, FIPS Software Summary, is attached.			
<b>11. ABSTRACT</b> <i>(A 200-word or less factual summary of most significant information. If document includes a significant bibliography or literature survey, mention it here)</i>  <p>The feasibility of using a near-field array for electromagnetic susceptibility testing is studied. The basic objective is to control the element weightings such that a plane wave is generated within the test volume. The basic theory is developed for arbitrary array geometries, and numerical results are obtained for finite planar arrays. A general near-field array synthesis technique is developed, and the technique minimizes the mean square error in the test volume while constraining the array excitations. The constraint prevents large currents and is useful in minimizing the fields outside the test volume. The basic idea looks promising, but some practical considerations, such as bandwidth and angular scanning limitations, require further theoretical and experimental investigation.</p>			
<b>12. KEY WORDS</b> <i>(Six to twelve entries; alphabetical order; capitalize only proper names; and separate key words by semicolons)</i> <p style="text-align: center;">array synthesis; dipole; electromagnetic susceptibility; Huygens' source; line source; near field; phased array.</p>			
<b>13. AVAILABILITY</b> <input checked="" type="checkbox"/> Unlimited <input type="checkbox"/> For Official Distribution. Do Not Release to NTIS <input checked="" type="checkbox"/> Order From Superintendent of Documents, U.S. Government Printing Office, Washington, D.C. 20402.  <input type="checkbox"/> Order From National Technical Information Service (NTIS), Springfield, VA. 22161		<b>14. NO. OF PRINTED PAGES</b> <p style="text-align: center;">109</p>	<b>15. Price</b>





# NBS TECHNICAL PUBLICATIONS

## PERIODICALS

**JOURNAL OF RESEARCH**—The Journal of Research of the National Bureau of Standards reports NBS research and development in those disciplines of the physical and engineering sciences in which the Bureau is active. These include physics, chemistry, engineering, mathematics, and computer sciences. Papers cover a broad range of subjects, with major emphasis on measurement methodology and the basic technology underlying standardization. Also included from time to time are survey articles on topics closely related to the Bureau's technical and scientific programs. As a special service to subscribers each issue contains complete citations to all recent Bureau publications in both NBS and non-NBS media. Issued six times a year. Annual subscription, domestic \$18; foreign \$22.50. Single copy, \$5.50 domestic; \$6.90 foreign.

## NONPERIODICALS

**Monographs**—Major contributions to the technical literature on various subjects related to the Bureau's scientific and technical activities.

**Handbooks**—Recommended codes of engineering and industrial practice (including safety codes) developed in cooperation with interested industries, professional organizations, and regulatory bodies.

**Special Publications**—Include proceedings of conferences sponsored by NBS, NBS annual reports, and other special publications appropriate to this grouping such as wall charts, pocket cards, and bibliographies.

**Applied Mathematics Series**—Mathematical tables, manuals, and studies of special interest to physicists, engineers, chemists, biologists, mathematicians, computer programmers, and others engaged in scientific and technical work.

**National Standard Reference Data Series**—Provides quantitative data on the physical and chemical properties of materials, compiled from the world's literature and critically evaluated. Developed under a worldwide program coordinated by NBS under the authority of the National Standard Data Act (Public Law 90-396).

NOTE: The principal publication outlet for the foregoing data is the Journal of Physical and Chemical Reference Data (JPCRD) published quarterly for NBS by the American Chemical Society (ACS) and the American Institute of Physics (AIP). Subscriptions, reprints, and supplements available from ACS, 1155 Sixteenth St., NW, Washington, DC 20056.

**Building Science Series**—Disseminates technical information developed at the Bureau on building materials, components, systems, and whole structures. The series presents research results, test methods, and performance criteria related to the structural and environmental functions and the durability and safety characteristics of building elements and systems.

**Technical Notes**—Studies or reports which are complete in themselves but restrictive in their treatment of a subject. Analogous to monographs but not so comprehensive in scope or definitive in treatment of the subject area. Often serve as a vehicle for final reports of work performed at NBS under the sponsorship of other government agencies.

**Voluntary Product Standards**—Developed under procedures published by the Department of Commerce in Part 10, Title 15, of the Code of Federal Regulations. The standards establish nationally recognized requirements for products, and provide all concerned interests with a basis for common understanding of the characteristics of the products. NBS administers this program as a supplement to the activities of the private sector standardizing organizations.

**Consumer Information Series**—Practical information, based on NBS research and experience, covering areas of interest to the consumer. Easily understandable language and illustrations provide useful background knowledge for shopping in today's technological marketplace.

*Order the above NBS publications from: Superintendent of Documents, Government Printing Office, Washington, DC 20402.*

*Order the following NBS publications—FIPS and NBSIR's—from the National Technical Information Service, Springfield, VA 22161.*

**Federal Information Processing Standards Publications (FIPS PUB)**—Publications in this series collectively constitute the Federal Information Processing Standards Register. The Register serves as the official source of information in the Federal Government regarding standards issued by NBS pursuant to the Federal Property and Administrative Services Act of 1949 as amended, Public Law 89-306 (79 Stat. 1127), and as implemented by Executive Order 11717 (38 FR 12315, dated May 11, 1973) and Part 6 of Title 15 CFR (Code of Federal Regulations).

**NBS Interagency Reports (NBSIR)**—A special series of interim or final reports on work performed by NBS for outside sponsors (both government and non-government). In general, initial distribution is handled by the sponsor; public distribution is by the National Technical Information Service, Springfield, VA 22161, in paper copy or microfiche form.

**U.S. Department of Commerce**  
National Bureau of Standards

Washington, D.C. 20234  
Official Business  
Penalty for Private Use \$300



POSTAGE AND FEES PAID  
U.S. DEPARTMENT OF COMMERCE  
COM-215

SPECIAL FOURTH-CLASS RATE  
BOOK